A Stand-Alone Hybrid Power System with Energy Storage

Abu Mohammad Osman Haruni

B.Sc. (BUET), M.ScEng. (University of Tasmania)

A thesis submitted for the fulfilment of the degree of Doctor of Philosophy

Centre of Renewable Energy and Power Systems (CREPS)

School of Engineering

University of Tasmania

January 2013

Abstract

Small-scale hybrid stand-alone power systems are becoming popular alternatives in remote and island areas where grid connection is not economically or technically viable. Harnessing the abundant supply of wind and solar energy can play an important role in ensuring an environmentally friendly and clean energy generation for remote and isolated communities. However, renewable energy sources are intermittent in nature, and as a result, power generation from renewable energy sources often may not necessarily match the load demand. Therefore, energy storage is required to ensure reliable power supply.

Hybrid power systems with renewable sources can provide efficiency, reliability and security, while reducing operational costs. However, the main challenge of hybrid power system applications is satisfying the load demand under constraints. Therefore, proper control and coordination of each energy generation unit is vital. It is also important to ensure robustness of the energy management system to avoid system black-outs when power from the renewable energy sources is not adequate to support all loads.

This thesis proposes a novel operation and control strategy for a hybrid power system for a stand-alone operation. The proposed hybrid system consists of a wind turbine, a fuel cell, an electrolyzer, a battery storage unit and a set of loads. The overall control strategy is based on a two-level structure. The top level is the energy management and power regulation system. The main objective of this system is to ensure a proper control and coordination of the system. It also controls load scheduling during wind variability under inadequate energy storage to avoid system black-outs. Depending on wind and load conditions, this system generates reference dynamic operating points to low level individual sub-systems. Based on these operating points, the local controllers manage the wind turbine, fuel cell, electrolyzer and battery storage units. The local controller of wind turbine extracts the reference power from the varying wind by regulating the rotor speed. The fuel cell is controlled by using a hydrogen regulator and boost converter, and the electrolyzer via a buck-converter. A bi-directional dc-dc converter is employed to control charging and discharging of the

battery storage system. The proposed control system is implemented with MATLAB Simpower software and tested for various wind and load conditions. Results are presented and discussed.

Authorship

The work continued in this thesis has not been published or previously submitted for a degree at this or any other educational institution. To the best of my knowledge, this thesis contains no material previously published or written by another person except where due reference is made.

Signed…….

Acknowledgements

Firstly, I would like to express my deepest and sincerest gratitude to the Almighty, the most compassionate and merciful who guides me in the most appropriate way towards the completion of my research.

I would like to express my sincere gratitude to my primary supervisor Prof. Michael Negnevitsky, University of Tasmania for his valuable advice and help. I would also like to thank all the academic stuff and postgraduate students of the School of Engineering, University of Tasmania, for providing a healthy and helpful academic environment.

I would like to express my deepest gratitude to all of my family members and relatives. Finally, I would like to thank the Graduate Research Unit of the University of Tasmania for providing support.

List of publications

Refereed journal publications

- Haruni, AMO and Negnevitsky, M, 'An Artificial Intelligence Approach to Develop a Time-Series Prediction Model of The Arc Furnace Resistance', *Journal of Advanced Computational Intelligence*, 14 (6) pp. 722-728.
- Gargoom, AMM and Haruni, AMO and Haque, ME and Negnevitsky, M, 'Smooth synchronisation and power sharing schemes for high penetration wind diesel hybrid remote area power systems', *Australian Journal of Electrical & Electronics Engineering*, 8 (1) pp. 75-84.
- Haruni, AMO and Negnevitsky, M and Haque, ME and Gargoom, AMM, 'A Novel Operation and Control Strategy for a Stand-Alone Hybrid Renewable Power System' *IEEE transaction of sustainable energy* (in press).

Refereed conferences publication

- Haruni, AMO and Negnevitsky, M and Haque, ME and Gargoom, AMM, 'Control Strategy of a Stand-Alone Variable Speed Wind Turbine with Integrated Energy Storage System Using NPC Converter', Proc of 2012 *IEEE PCS General Meeting*, 21-25 July, San Diego, USA, pp. 1-7.
- Haruni, AMO and Negnevitsky, M and Haque, ME and Gargoom, AMM, 'A Novel Power Management Control Strategy for a Renewable Stand-Alone Power System ', *Proc of 2011 IEEE PCS General Meeting*, 24-28 July, Detroit, USA, pp. 1-8.
- Gargoom, AMM and Haruni, AMO and Haque, ME and Negnevitsky, M, 'Hybrid stand-alone power systems with hydrogen energy storage for isolated communities', *2010 IEEE PES Transmission and Distribution Conference and Exposition*, April 19-22 2010, New Orleans, Louisiana, USA.
- Gargoom, AMM and Haruni, AMO and Haque, ME and Negnevitsky, M, 'Voltage and frequency stabalizer based on Fuzzy Logic control for three-level NPC converters in stand-alone wind energy systems', *Power and Energy Society General Meeting, 2010 IEEE*, July 25-29 2010, Minneapolis, Minnesota, USA.
- Gargoom, AMM and Haruni, AMO and Haque, ME and Negnevitsky, M, 'Voltage and frequency stabilization using PI-like fuzzy controller for the load side converters of the stand alone wind energy systems', *IEEE Power Electronic Society*, February 21-25 2010, Palm Springs, California USA, pp. 2132-2137.
- Haruni, AMO and Gargoom, AMM and Haque, ME and Negnevitsky, M, 'Dynamic Operation and Control of a Hybrid Wind-Diesel Stand Alone Power

Systems', *2010 Twenty-Fifth Annual IEEE Applied Power Electronics Conference and Exposition (APEC'10)*, February 21-25 2010, Palm Springs, USA, pp. 162-169.

- Haruni, AMO and Haque, ME and Gargoom, AMM and Negnevitsky, M, 'Efficient Control of a Direct Drive IPM Synchronous Generator Based Variable Spwwed Wind Turbine with Energy Storage', *36th Annual Conference on IEEE Industrial Electronics Society (IECON 2010)* , 7-10 Nov 2010, Phoenix AZ, pp. 457-463.
- Haruni, AMO and Gargoom, AMM and Haque, ME and Negnevitsky, M, 'Voltage and Frequency Stabilisation of Wind-Diesel Hybrid Remote Area Power Systems ', *Proceedings of Australasian Universities Power Engineering Conference (AUPEC 2009)*, 27-30 September 2009, Adelaide.

Table of Content

Figures

Tables

Abbreviation

AFC	Alkaline Fuel Cell
ANFIS	Adaptive Neuro-Fuzzy Inference System
DFIG	Doubly-fed Induction Generator
DMFC	Direct Methanol Fuel Cell
EIA	Energy Information Administration
EMPRS	Energy Management and Power Regulation System
EV	Electric Vehicle
FSC	Full Scale Power Converter
HFAC	High Frequency Ac- coupled
IG	Cage Induction
IPM	Interior Permanent Magnet
IPMSG	Interior Permanent Magnet Synchronous Generator
KOH	Potassium Hydroxide
MAS	Multi-Agent System
MCFC	Molten Carbonate Fuel Cell
MMF	Magneto-motive force
NiCad	Nickel/ Cadmium
NiMH	Nickel/ Metal Hydride
Pcomp	Compressor Power
PEM	Proton Exchange Membrane
PEMFC	Proton Exchange Membrane Fuel Cell
PFAC	Power Frequency Ac-coupled
PHEV	Plug-in Hybrid Electric Vehicle
PID	Proportional, integral and derivative
PMG	Permanent- Magnet Generator
PMSG	Permanent- magnet Synchronous Generator
PWM	Pulse-width Modulation
SCIG	Squirrel- Cage IG
SG	Synchronous Generator

SMES	Super- Conducting Magnetic Energy Storage
SPM	Surface Permanent Magnet
SOC	State of Charge
SOFC	Solid Oxide Fuel Cell
SOH	State of Health
VRLA	Valve-Regulated Lead -Acid
WECS	Wind Energy Conversion System

Introduction

A stand-alone power system is an autonomous power generation system that supplies electricity without being connected to the grid. Such systems are often located on islands and in remote parts of the world where grid connection is not technically or economically viable. The electric power can be generated from diesel, natural gas or preferably from renewable energy sources such as wind, hydro or solar system.

Diesel generators are popular in remote area power system applications for their reliability, low installation costs, ease of starting, compact power density and portability [1], [2]. In stand-alone power system applications, they are generally sized to supply at least the peak system load. However, diesel generators have some disadvantages as follows:

- Diesel generators are becoming expensive to run due to increasing fuel cost and transportation costs. According to the Australian Institute of Petroleum (AIP), the retail price of the diesel fuel has increased about three times in the last decade [3].
- Diesel generators require a high level of maintenance cost [4], [5].
- Diesel generators are efficient only when running at rated load [5]. A diesel engine has higher fuel consumption at light loads at constant speed. This is due to incomplete fuel combustion during light loads [5]. It is usually recommended by the manufacturers that diesel generators have to run at a minimum load of about 30% to achieve high operating efficiency [6]. The typical fuel consumption and fuel efficiency curve of a 50 kVA diesel generator is shown in Fig. 1 [5]. From Fig. 1, it is seen that a typical 50 kVA diesel generator operates at highest efficiency (about 33%) at the rated load. At 30% of rated load (15 kVA), the efficiency is as low as 20%. It is also seen that, as the load decreases, the efficiency decreases.

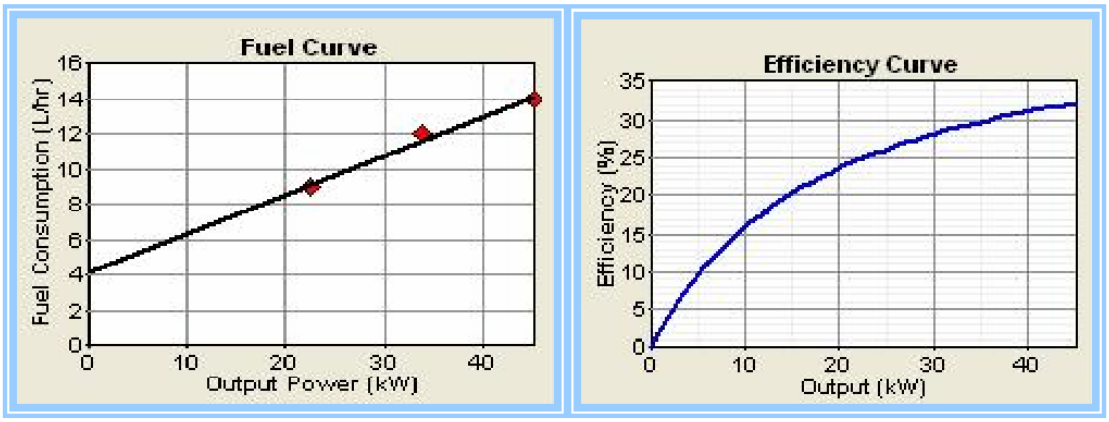

Fig. 1. Typical fuel consumption and fuel efficiency curve of a diesel generator [5].

- Diesel generators rely on a continuous supply of fuel. As a result, it is important to ensure security of fuel supply in remote areas.
- Diesel generators pollute the local environment as they emit greenhouse gases [5], [7] and they also create noise [5].

Renewable energy sources such as hydro, solar, wind, bio-mass, geothermal and tidal can act as an alternative power sources in stand-alone power system applications, as they provide clean power for remote communities. In general, there is huge potential for utilizing renewable energy sources in most remote areas which can provide a clean and environmentally-friendly power supply to the community. However, the main challenge of using renewable energy sources for stand-alone power system applications is that the availability of power has daily and seasonal patterns that may not match the load demand. Combining renewable energy generation with a stand-by generator or energy storage device will render the renewable energy sources more reliable and affordable. This kind of electric power generation system with a main power source from renewable energy and back up generation or energy storage is known as a 'hybrid power system'. The main objective of such systems is to produce as much energy as possible from the renewable sources while maintaining acceptable power quality and reliability. However, a renewable energy-based stand-alone power supply system introduces a number of technical challenges. These challenges are mainly attributed to the intermittent nature of

renewable power, variable loads and low inertial of such systems [8]-[18]. The technical challenges are listed below:

- **Intermittent nature of renewable energy sources –** A major challenge for using renewable energy sources such as wind and solar is that they are variable and intermittent [8]-[15]. Using such sources in a hybrid power generation system typically requires extensive backup generation or energy storage capacity in order to eliminate the effects of their variable and intermittent nature [8]-[15].
- **Load fluctuation –** Electricity consumption varies over time. These temporal variations include moment-to-moment fluctuations and hour-to-hour changes associated with daily, weekly, and seasonal patterns [16]-[18]. As a result, a renewable energy based hybrid power system has to respond to such load changes.
- **Power quality issues –** Perfect power quality means that the voltage is continuous and sinusoidal, having a constant amplitude and frequency. Power quality can be expressed in terms of physical characteristics and properties of electricity. It is most often described in terms of voltage, frequency and interruptions [19]-[22]. The voltage quality must fulfill stipulated national and international standards. Within these standards, voltage disturbances are subdivided into voltage variation, flicker, transients and harmonic distortion. Voltage variations are caused by the intermittent nature of renewable energy sources and load fluctuation. Voltage flicker and harmonics may be caused by the presence of non-linear loads and power electronic converters in the system [23], [24]. Transients may occur due to the dynamic characteristics of the renewable energy sources and loads.
- **Difference in response time for integrated components –** One of the main challenges of control strategy is to ensure transient stability of different components of the hybrid power system when they work together. As a stand-alone power system experiences various disturbances such as fluctuating loads

and outputs of renewable sources, energy storage with a fast response is required to ensure transient stability [25], [26]. Moreover, the hybrid energy storage with different energy storage devices may respond differently to certain disturbances [25]-[28]. Therefore, coordinated control needs to be developed to ensure better transient stability of the stand-alone power system.

- **Energy storage strategy and back-up power generation –** Energy storage plays an important role in hybrid stand-alone power system applications, as they are used for both short-term transient stability and long-term load leveling and peak shaving applications [25]-[31]. As a result, a proper management of energy storage is needed to ensure a continuous, reliable and quality power supply. Back-up power generation is also used in stand-alone power systems. It can be employed to share power demand, especially during peak load conditions when power from renewable energy sources and energy reserves in the storage system are insufficient to satisfy the load demand. Small-scale diesel generators are often used as the back-up generation.
- **Security of supply –** Security is defined as the ability of a power system to withstand sudden disturbances [32], [33]. As a result, sufficient generation resources must be present to meet projected loads and reserves for contingencies [32], [33]. Security also implies that the power system will remain intact, even after outages or equipment failure. As a result, a proper system planning and operation strategy is vital.
- **Demand-side management –** Demand-side management (DSM) has been traditionally seen as a means of reducing peak electricity demands [34], [35]. DSM has various beneficial effects in a stand-alone power system application, such as mitigating electrical system emergencies, reducing the number of blackouts and increasing overall system reliability [34]-[35]. Moreover, DSM also helps to reduce dependency on expensive non-renewable fuel, thus reducing energy costs as well as harmful emissions. Finally, DSM plays a major role in

deferring high-cost investments in generation, transmission and distribution networks in long-term asset planning. As a result, DSM applied to electricity systems provides significant economic, reliability and environmental benefits.

- **Load growth –** Over time, stand-alone power supply systems may experience increasing load demand as a result of population growth and continuous economic growth of the community [36]-[38]. As a result, the structure and overall control strategy has to be flexible enough for the system to increase the generation rating to cope with increased load demand.
- **Economic aspect of hybrid system –** In the case of a stand-alone power system, the cost of power generation has to be minimized through proper equipment sizing and load matching [39]-[45]. In the economic analysis, capital and maintenance costs, and energy cost for different resources have to be accounted for in order to optimize the hybrid renewable energy-based system.

Meeting the technical and financial challenges associated with renewable energy-based hybrid power systems requires research in several areas. These are indentified and categorized as follows:

i) **Proper control of renewable energy sources to achieve optimum power output** – It is important to ensure that each energy generation source operates at its optimum level. Hence, proper control of the renewable energy sources is required.

ii) **Proper co-ordination of each sub-system of the hybrid system** –In the hybrid stand alone power system, proper co-ordination among each subsystem is essential when they operate together. There, the control system has to coordinate different sub-systems in order to achieve efficient operation.

iii) **Proper selection of energy storage devices** – Energy storage devices are an integral part of the hybrid power system. Energy storage can be classified as short-term or long-term. Short-term energy storage refers to a storage device that can release or absorb a large amount of energy relatively quickly. Such

storage is used to improve transient stability of the system in the event of sudden changes in wind or load conditions [25], [26]. Long-term energy storage is used for load leveling or peak-shaving purposes [27]-[30]. Proper selection of energy storage is required to ensure stable, cost-effective and reliable stand-alone power generation in remote and isolated areas.

iv) **Output voltage and frequency regulation** – The main challenge of a hybrid power system is to ensure a power supply with regulated voltage and frequency. Non-linear, unbalanced load conditions contribute to voltage harmonics and distortions. Moreover, due to low inertia, the system frequency can be affected by a sudden load change and the intermittent nature of renewable energy sources. As a result, power quality issues need to be addressed.

v) **Optimum location of energy sources** – It is very important to determine the optimum location of renewable energy sources and storage systems. As the power output from renewable energy sources depends on geographic location, a better location can enhance the utilization of renewable energy sources [46], [47]. In addition, in stand-alone power systems, voltage profile at the distribution level can fall below operating standards owing to distribution losses. Energy storage devices installed in critical areas can improve the voltage profile of the system.

vi) **Optimum sizing of the system** – Optimum sizing of renewable energy sources and storage systems need to be determined so as to ensure reliable, cost-effective power generation of a hybrid power system [39]-[45].

Considering the practical challenges associated with hybrid stand-alone power supply applications, the following are the main objectives of this thesis:

a. Components of a hybrid power system for stand-alone operation

Among various renewable energy sources, wind and solar energy are often available in remote and isolated areas. Other sources such as bio-mass, geothermal and

tidal energy are more geographically dependent. Favorable conditions for renewable energy are necessary, as the cost of electricity is heavily dependent on local weather patterns [46], [47]. In this project wind energy is considered, as wind turbine-based hybrid power systems offer a cheaper option compared with a solar energy-based hybrid renewable power supply [47].

Different types of energy storage systems such as pumped hydro, compressed air, flywheel, thermal, hydrogen, batteries, superconducting magnetic and super-capacitors are used in various applications for different purposes. Pumped hydro and compressed air energy storages are low cost options [25]. However, they have lower efficiency. Moreover, pumped hydro is dependent on the geographical location. Flywheel energy storage, batteries, superconducting magnetic energy storage and super-capacitors have a higher energy density and a very fast time response [25], [26]. As a result, they can support a sudden change of the power demand and provide better transient stability. On the other hand, fuel cells and electrolyzers have higher power density with slower time responses [27]- [31]. Therefore, they are more suitable for long-term load leveling applications. Considering the application of energy storage systems in the wind turbine-based hybrid power system, a combination of the fuel cell, electrolyzer and battery can represent the most suitable option. Firstly, excess power from wind can either be stored in the battery storage system or can be used to generate hydrogen by the electrolyzer. Secondly, batteries respond very quickly, ensuring better stability of the hybrid system during transient periods caused by sudden changes of wind and load. Thirdly, this combination can improve the efficiency of the system by sharing power so as to allow the operation of a fuel cell in a high efficiency region.

A diesel generator is considered as a back-up for the stand-alone system. In this project, the diesel generator is used only when the system suffers from severe conditions such as loss of wind turbine or lack of energy storage.

b. Control of each energy source

Each energy generation system has to be controlled optimally. In the proposed

hybrid power system applications, the main objective of the wind turbine control is to extract optimum power from wind. The energy storage is controlled such as to absorb excessive power from the wind in high wind conditions and release the necessary power during low wind conditions. Moreover, the energy storage is also responsible for ensuring a transient stability of the system under varying wind and load conditions. A back-up diesel generator is used to provide power only in emergency situations. It is controlled to run in droop mode (power sharing) or asynchronous mode (stand-alone).

c. Energy management and power regulation system

In this project, a supervisory controller (energy management and power regulation system) is developed to ensure optimum energy use and to coordinate local controllers at each energy generation source. Depending on wind and load conditions, this system generates reference dynamic operating points to the local controls of individual sub-systems. It also controls the load scheduling operation during unfavorable wind conditions with inadequate energy storage to avoid system black-outs.

The project aims to overcome the practical problem associated with renewable energy based power system application for stand-alone application. The major contribution of the thesis is listed below:

- Wind turbine control and optimum power extraction from varying wind.
- Energy storage modeling and control.
- Hydrogen storage system modeling and control
- Load side inverter control
- Dual-fuel diesel-hydrogen generator modeling and control.
- Energy management and power regulation system.

The overall system diagram is shown in Fig. 2.

The thesis organized as follows:

Chapter 1 presents a literature review of a renewable energy-based hybrid stand-alone power system. This chapter contains a general overview of hybrid power systems,

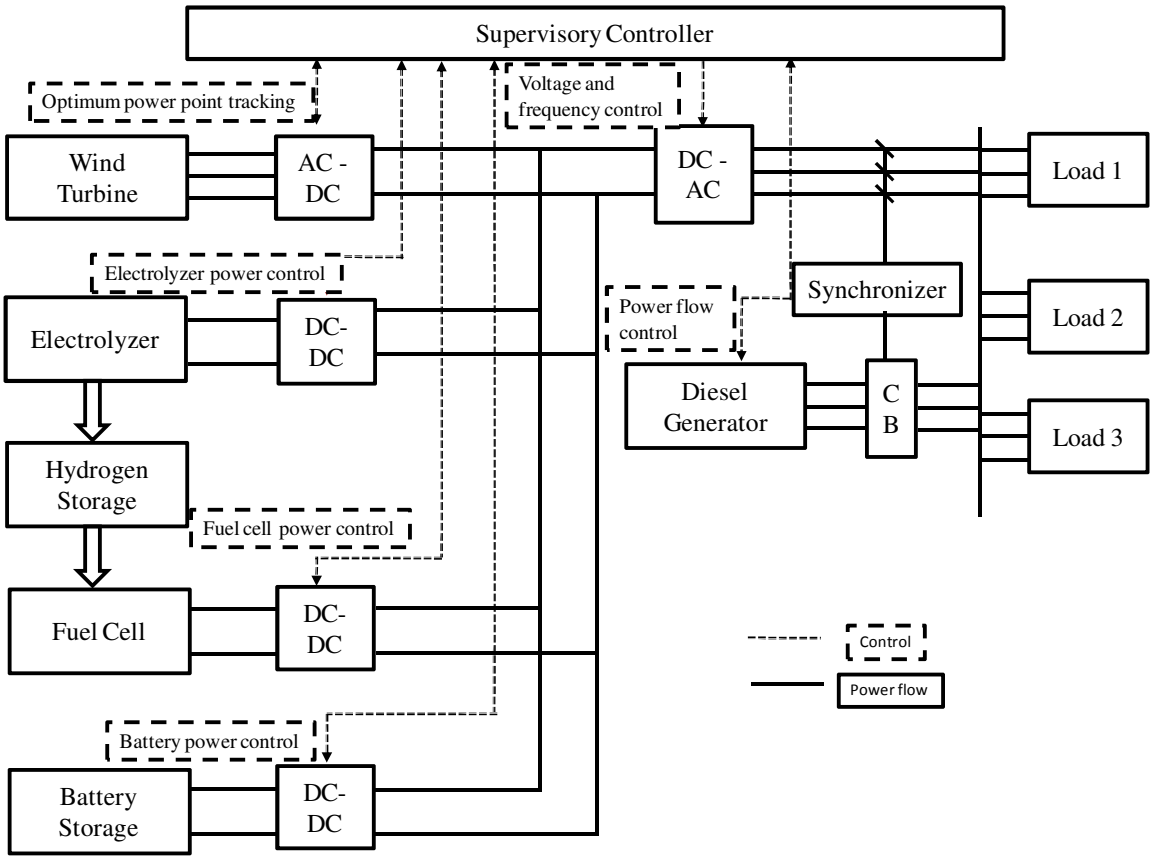

Fig.2. Block diagram of proposed hybrid power system.

their structure, different power generation sources, energy storages and associated control and coordination techniques of hybrid power systems.

Chapter 2 presents the wind turbine modelling and control. This chapter discusses a permanent magnet based variable speed wind turbine. The optimum power extraction technique is also presented.

Chapter 3 presents the energy storage system and load side inverter modelling and controls. It discusses about the modelling and control aspects of the battery storage system, fuel cell and electrolyzer. Moreover, this chapter focuses on the interaction of each energy storage system. This chapter also demonstrates the output voltage and frequency control in inverter system modelling and control part.

Chapter 4 presents the details modelling and control of a diesel generator. This chapter also discusses about the 'black-box' modelling of a dual fuel diesel-hydrogen generator. Power sharing techniques of diesel generator with other power generation sources are also included.

Chapter 5 presents the supervisory controller modelling. It discusses about the overall coordination of a hybrid system. A load shedding algorithm is proposed, which ensures continuous system operation, thus avoiding system black-outs.

Chapter 6 presents a case study of proposed hybrid system. A number of case studies are presented in different wind and loading conditions to justify the application of the proposed system for stand-alone operation.

Finally, a conclusion and future work recommendations are presented.

Chapter 1

Stand-Alone Hybrid Power System

This chapter presents an overview relevant to the scope of the proposed research project, comprised of different sections. Section 1.1 provides an overview of a renewable energy based hybrid power system. Section 1.2 presents different structures of the hybrid power supply system. Section 1.3 provides in-depth literature of a wind energy conversion system. Section 1.4 presents a detailed study of an energy storage system. Section 1.5 provides different control and co-ordination techniques for a stand-alone power system. Section 1.6 provides the challenges, issues and future vision of fully renewable energy based hybrid power system. Finally, some remarks are presented to conclude the chapter.

1.1 Overview of Hybrid Power System

With the rapid growth and challenges of power generation, distribution, and usages, renewable energy technologies can play an important role in future power supply due to increased awareness of environmental pollution. In the case of power supply system to remote and isolated communities, a renewable energy based stand-alone power system can be a particularly attractive cost-effective solution, as grid extension is often impractical due to economic and technical constraints.

Diesel generators are most commonly used as a stand-alone power supply system application to remote and isolated communities for their reliability, cheap installation, ease of starting, compact power density and portability [48], [49]. However, rising fuel prices make them very expensive to run. Moreover, they cause significant environmental pollutions. In most remote and isolated areas, renewable energy sources such as wind and solar are available, which can provide clean cost-effective power. However, due to the intermittent nature of renewable energy sources, hybrid combinations of two or more

energy sources along with energy storage can improve reliability and ensure a continuous and cost-effective power supply.

Different generation sources may operate in tandem to achieve higher energy efficiency and improve system performance. As an example, wind and solar power can complement each other on daily basis. Integration of battery or super-capacitor storage systems can improve transient stability of a fuel cell and wind turbine based hybrid power system in the event of wind and load changes [50]-[52].

In renewable energy-based hybrid power system applications, energy storage is considered as an integral part of the system [53]-[67]. Energy storage can improve transient stability of the system when wind and load variation occurs [53]-[55]. Most importantly, they are used for load leveling and peak shaving applications [56], [57]. However, proper technology selection, operation and control strategies, structure of the hybrid power system, and generation unit sizing are also vital to construct a robust renewable energy based hybrid power supply system [62]-[67].

A case study reported in [46] describes a cost-effective power supply solution in a remote area in Tunisia. The climate of Tunisia, located in North Africa, well-suited to the use of solar energy. There are many small, remote locations in Tunisia which rely on diesel generators for electric power, as grid extension is not economically feasible. The cost of running these generators can be quite expensive when accounting for the transportation costs and efficiency of diesel generators during off-peak periods. As a result, a hybrid solar power with battery storage-based power system was considered for continuous power supply in this area. It has been shown that the power generation cost of hybrid a solar and battery storage system is $240.65 per MWh, whereas a diesel generator based power supply system costs about $289.1 per MWh. In favorable wind conditions, wind turbine-based hybrid power systems can offer a cheaper solution compared with solar energy based hybrid renewable power supply [68].

1.2 Structure of Hybrid System

A well-defined framework of a hybrid system is vital, as various energy sources may have different operating characteristics. In an optimal framework, the renewable energy sources, energy storage, and loads are integrated and capable of operating autonomously as a unit [68]. A robust system should also have a "plug-and-play" capability which renders the system capable of integrating any number of devices without system re-configuration [68], [69].

There are various ways to integrate different energy sources and storage to form a hybrid power system. Among them, dc-coupled, ac-coupled and hybrid-coupled are the most popular options [70]-[74], which outlined as below:

1.2.1 DC-Coupled Systems

In a dc-coupled system, all renewable energy sources are connected to a dc bus either directly or through appropriate power electronic converters. A block diagram of the system is shown in Fig. 1.1. This system can be connected to the dc loads through appropriate dc-dc converter, ac loads through a dc-ac converter or utility grid through a bi-directional dc-ac converter. The system is flexible and can be connected to an ac load of 50/60 Hz frequency. The dc-coupling scheme is very simple and is not required to be synchronous with the ac system. However, a dc-coupled system suffers from various weaknesses. For example, if the system converter connecting the utility grid with the bus is out of service, the whole system will not be able to supply ac power. To rectify this, several inverters can be connected in parallel. As such, synchronization of output ac voltage and proper power sharing are required to achieve a desired load distribution [75].

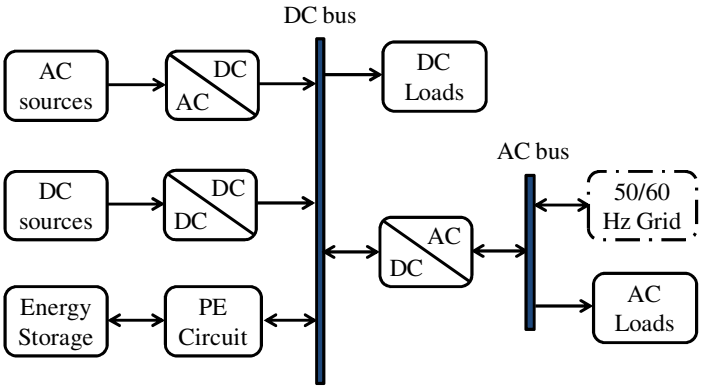

Fig. 1.1. Schematic diagram dc-coupled hybrid energy system.

1.2.2 AC-Coupled Systems

An ac-coupled system can be divided into two categories: power frequency ac-coupled (PFAC), and high frequency ac-coupled (HFAC) systems. The PFAC coupled system is shown in Fig. 1.2 (a), where the different energy sources are integrated through their own power electronic interfacing circuits to a power frequency ac bus. In this arrangement, coupling inductors are required between the power electronic interfacing circuits and power frequency ac bus to achieve the desired power flow management.

The HFAC system is shown in Fig. 1.2 (b), where different energy sources are coupled to a HFAC bus in which HFAC loads are located. This application is mainly used for HFAC loads (e.g., 400 hz) such as airplanes, vessels, submarines and space stations.

In both PFAC and HFAC systems, dc power can be obtained through an ac-dc converter. The HFAC may also include a PFAC bus and utility grid through an appropriate ac-ac and/ or ac-dc converter, where regular ac loads can be connected.

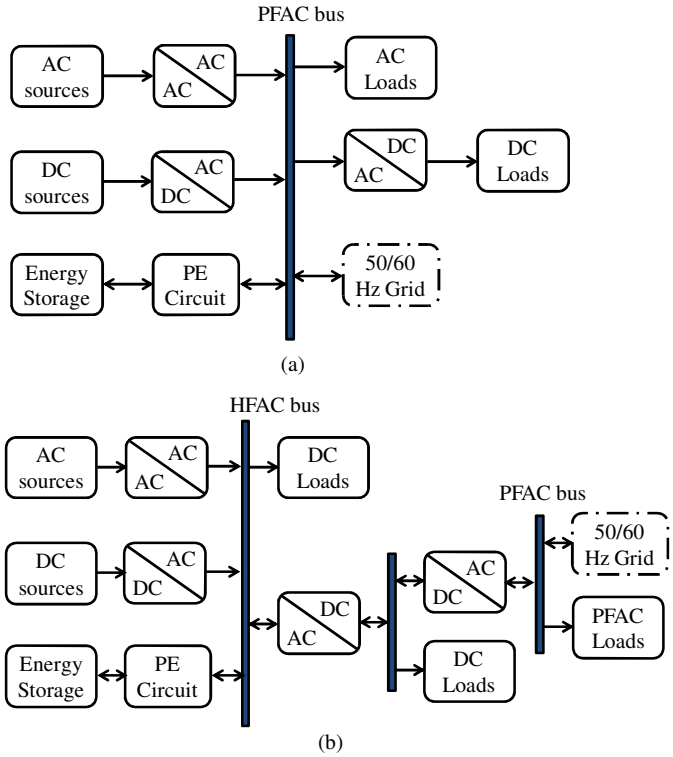

Fig. 1.2. Schematic diagram ac-coupled hybrid energy system.

1.2.3 Hybrid-Coupled Systems

In hybrid-coupled system as shown in Fig. 1.3, various DG sources are connected to the dc or ac buses of the hybrid system. In this application, some energy sources can be implemented directly without the use of a power electronic interfacing system. As a result, the system can operate with higher efficiency and reduced cost. However, control and energy management can be more complicated than with dc-coupled and ac-coupled systems.

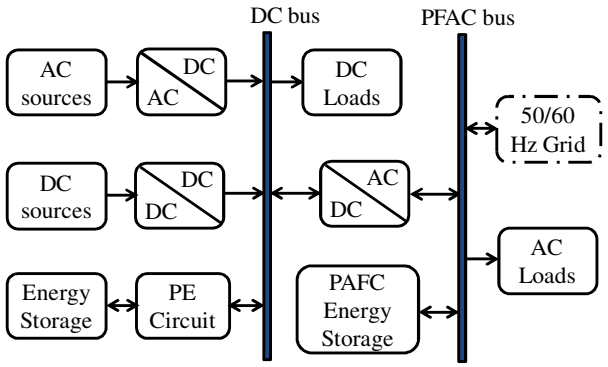

Fig. 1.3. Schematic diagram of hybrid-coupled hybrid energy system.

Different coupling schemes have their own appropriate applications. If the major generation sources generate dc power and there is a substantial dc load in the system, a dc-coupling system is preferable. On the other hand, if the main power systems are ac with substantial ac loads, an ac-coupled system is preferred. If the major power generation system is a combination of ac and dc power, then hybrid coupled system is the best.

1.3 Wind Energy Conversion System

In the last decade, wind power generation systems have experienced tremendous growth and been recognized as an alternative environmentally-friendly and cost-effective means of power generation. The major components of a typical wind energy conversion system (WECS) include a wind turbine, generator and control systems. Fig. 1.4 shows a WECS. The generators conventionally used in WECSs are the doubly-fed induction generator (DFIG), cage induction generator (IG), and synchronous generators (SG). The power electronics correspond to a back-to-back converter. The WECS can be connected to a large utility, a micro-grid (weak grid), or a stand-alone load.

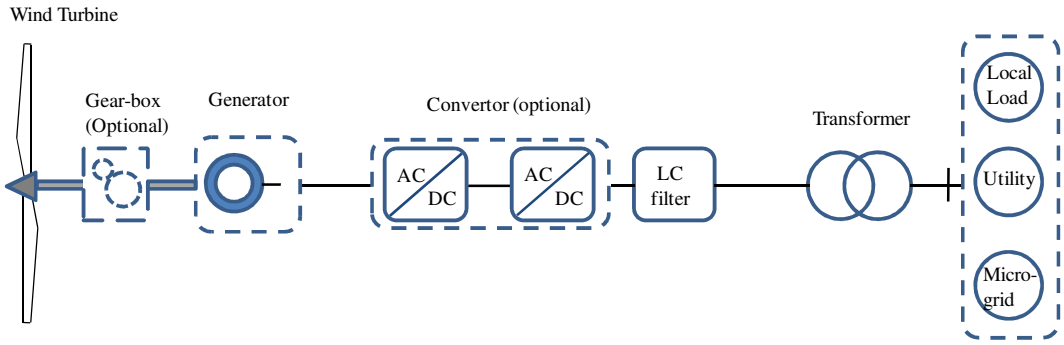

Fig. 1.4. Wind energy conversion system.

1.3.1 DFIG- based WECS

The DFIG is widely used for variable-speed generation and is one of the most important generators for wind-energy applications [76]-[81]. The DFIG-based WECS is shown in Fig. 1.5. Nowadays, the DFIG-based wind turbine accounts for about 50% of wind energy market share. For a typical DFIG, a back-to-back power converter is connected to the rotor for a restricted speed range of operation, typically 30% of its rated value [78], [79]. In DFIG-based WECS, slip rings connect the machine-side converter to the rotor, and gearboxes are also required, since a multi-pole low-speed DFIG is not technically feasible [57].

DFIG-based WECS speed can be regulated for desired electrical torque via the rotor-side converter. Speed regulation is mainly used to optimize power extraction from the wind. The possibility of controlling the active and reactive power gives this system rolling capacity on the grid [82]-[84].

A DFIG-based WECS can contribute to the short-circuit power because the stator is directly coupled to the grid. Therefore, during a grid fault, relatively high currents may be produced in the DFIG stator windings. However, direct connection between stator and grid may limit the capacity of this generator to remain connected to the system during a fault period. To improve the fault handling capacity, a crowbar is usually adopted to limit the currents and voltages to a safe level in the rotor circuit where the back-to-back power

converter is used. The three-phase rotor winding is short-circuited via the closed crowbar switch which transfers the DFIG in a standard IG. During the switching operation, the high currents produced may cause sudden torque loads on the drive train.

Most major wind turbine producers manufacture WECSs based on DFIGs. However, difficulties in complying with grid fault ride-through requirements may limit its use in the future [85], [86].

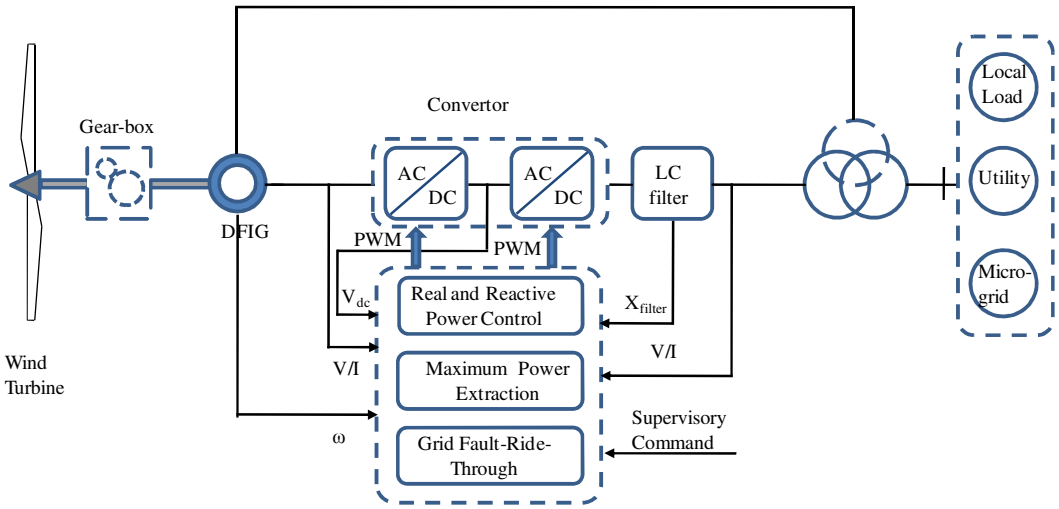

Fig. 1.5. DFIG-based WECS.

1.3.2 SCIG-based WECS

The squirrel-cage IG (SCIG) shown in Fig. 1.6, is a very popular machine due to its mechanical simplicity and robust construction [76]. Unlike the DFIG, no brushes are required for the machine's operation. Minimal maintenance is necessary, apart from bearing lubrication. The SCIG was widely used in fixed-speed WECS [76] (first Danish wind turbines), and it is still used for variable-speed wind-energy generation. The IG with a frequency converter is completely decoupled from the grid; hence this system has a complete grid connection capacity.

The main drawbacks of the SCIG reside in the fact that two full power converters are required for operation and a multi-pole direct-drive operation is not technically feasible [76]. Therefore, SCIGs do not have the advantage of variable-speed operation using reduced-size power converters (as in the DFIG). SCIGs cannot be used in direct-driven WECS [as in permanent-magnet generators (PMGs)]. Hence, the number of WECS producers manufacturing topologies based on SCIGs is relatively low.

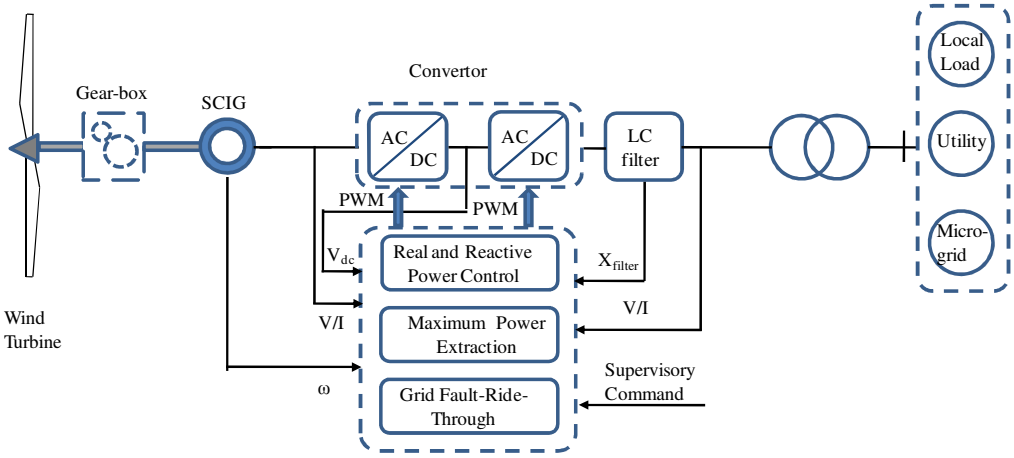

Fig. 1.6. SCIG-based WECS.

1.3.3 SG-based WECS

In SG based WECS shown in Fig. 1.7, an excitation is provided via rotor windings. Hence, a full-scale power converters (FSCs) are needed, and a reduced scale converter for the excitation is required for synchronous machines.

The cost, weight and size of the SG based wind turbine are higher than its DFIG counterpart. The reliability of direct drive SG is very high due to the absence of a gearbox, the slipping ring, and brushes. As a result, they are more suitable for applications where the logistics could be a problematic and robustness is of paramount importance; e.g., offshore wind parks. Moreover, they can have a better ride-through capability.

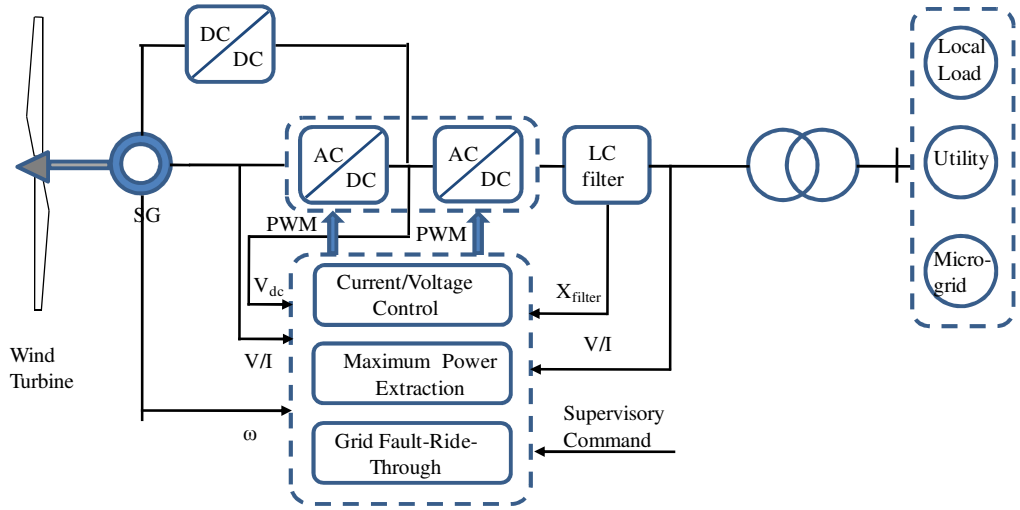

Fig. 1.7. SG-based WECS.

1.3.4 PMSG-based WECS

PMSGs are considered to be one of the most promising technologies for wind energy systems [76], [87]. In PMSG-based WECS, full-scale power converters (FSCs) are needed.

The direct-drive permanent-magnet SG (PMSG) shown in Fig. 1.8, is considered to be the most efficient, as power losses are about 65% of a typical DFIG-based WECS [88]. However, the cost, weight and size of the PMSG-based wind turbine is higher than its DFIG counterpart. The reliability of direct drive PMSG is very high due to the absence of a gearbox, slipping rings, and brushes. As a result, they are more suitable for applications where the logistics could be a problematic and robustness is of paramount importance; e.g., offshore wind parks. Moreover, they can have a better ride-through capability.

Multi-pole PMSGs with full-power back-to-back converters appear likely to be the configuration adopted by most large wind-turbine manufacturers in the near future, replacing the doubly-fed generator as the main generator in the wind-energy market. An additional advantage of direct-drive generators is noise reduction achieved when the

gearbox is eliminated from the WECS [89]. For offshore applications, increased reliability and the elimination of possible oil spills from the gearbox is another advantage.

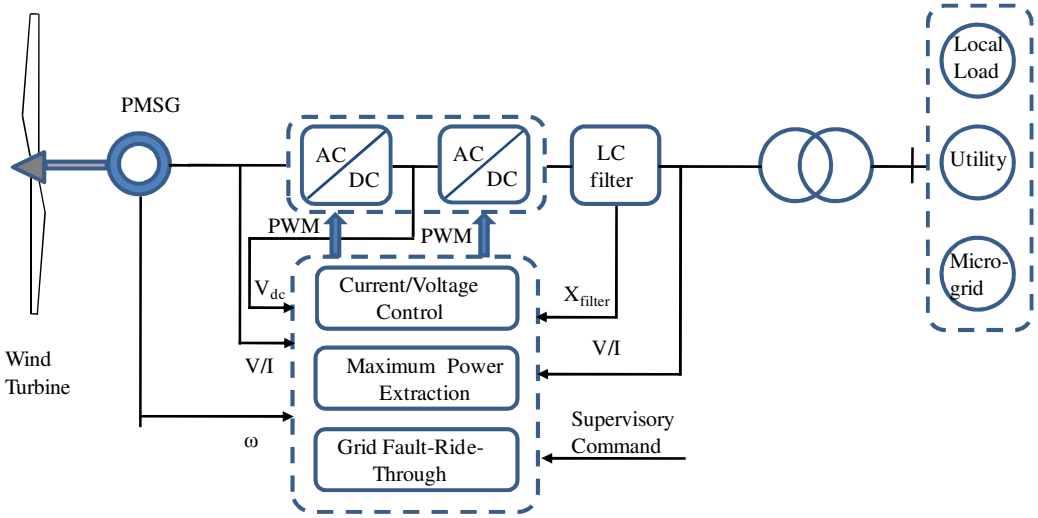

Fig. 1.8. PMSG-based WECS.

1.3.5 Multibrid Concept (PMSG with Single Gearbox)

With the increase in WECS rated power, the direct-drive operation of generators may require electrical machines of considerable size, weight and cost. In this case, a topology introduced by the German company Multibrid is shown in Fig. 1.9. The Multibrid concept developed a WECS comprised of a medium-speed PMSG and a single-stage gearbox with a gear ratio of 6–10 [90], [91]. This allows weight and size reduction of the generators combined with gearbox technology which is lighter, more reliable and cheaper than the standard three-stage gearbox with a typical ratio of 80–100.

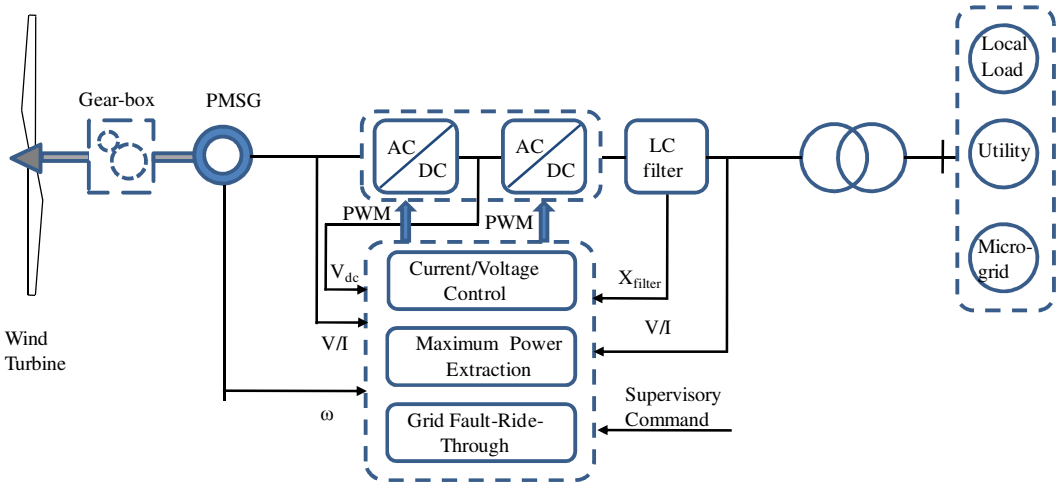

Fig. 1.9. Multibrid concept.

Among different types of WECS, the DFIG based WECS is very popular as the lightest, low cost solution with standard components. However, it has a low energy yield due to high losses in the gearbox. Since it is mainly built from standard components consisting of copper and iron, major improvements in performance or cost reduction cannot be expected.

The direct drive PMG generator seems far more feasible, since the active material weight of the generator for the same air-gap diameter is nearly halved, while the energy yield is several percent higher. While having the highest energy yield, it is more expensive than the generator systems with a gearbox. Further improvements can be expected since the cost of the permanent magnets and the power electronics is decreasing.

1.4 Energy Storage System

Energy storage systems are an integral part of a hybrid renewable stand-alone power system, which is critical for ensuring a high level of power quality, reliability and security. An ideal storage system would offer fast access to power as required, provide high capacity power and energy, have a long life expectancy, and at a competitive price.

However, an ideal storage system is not currently available. As a result, it is important to select the appropriate storage technology for the application of renewable energy based hybrid power systems. The preliminary applications of energy storage systems for a stand-alone hybrid renewable energy based power system are as follows:

• Renewable matching and power smoothing

Renewable energy sources are intermittent in nature. As a result, power generation frequently fails to match the load profile or demand cycle. Energy storage can be used to match the output of renewable sources to any load profile.

• Load leveling application

In load leveling application, bulk energy is stored during peak wind conditions and then discharged during low or no wind conditions. As a result, proper management of energy storage can ensure continuous system operation.

• Power quality

Utility power sometimes suffers disturbances such as momentary voltage sags or even outages. Along with harmonic distortions, and other imperfections can affect sensitive equipment requiring high quality power. Energy storage systems can be used to provide reliable, high quality power to sensitive loads.

Based on the application, the energy storage can be classified as long-term and short-term. Capacity-oriented energy storage technologies such as pumped hydroelectric systems, compressed air energy storage and hydrogen storage do not generally have a fast response time and are used for long-term energy storage. On the other hand, storage devices with a fast response time such as batteries, fly-wheels, super-capacitors and super-conducting magnetic energy storage (SMES) are used for responding to short time disturbances such as fast load transients, and for power quality related problems. Fig.

1.10 shows the typical storage capacity versus discharge time for different energy storage systems.

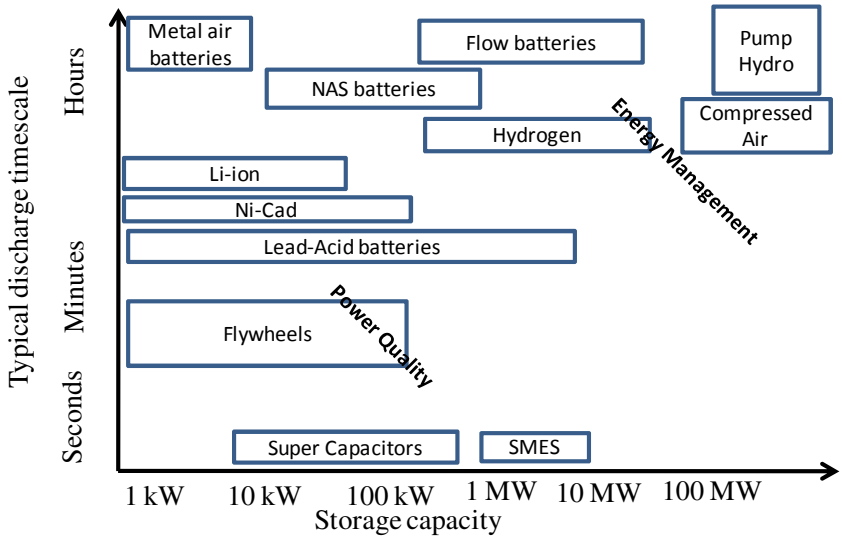

Fig. 1.10. Capacity versus discharge time for different energy storage systems.

Energy storage can be electrochemical, mechanical, electromagnetic, thermal or hydrogen-based.. Electrochemical energy storage includes lead-acid, lithium-ion, flow and sodium-sulfur batteries. Mechanical energy storage includes pumped hydroelectric, compressed air energy and fly-wheel. Electro-magnetic storage systems such as superconducting magnetic energy storage (SMES) and thermal energy storage can include solar thermal and thermal storage for heating, ventilation and air conditioning. Hydrogen storage includes electrolyzer and fuel cells.

1.4.1 Electrochemical Energy Storage

Batteries used to store and supply power to renewable energy based power systems must be reliable, durable and safe. Several promising battery technologies exists for grid connected or stand alone based renewable energy system applications including lead-acid, lithium-ion, flow, sodium-sulfur batteries.

- **Lead-acid batteries**

Lead-acid batteries are mature and proven technology in a number of applications including frequency regulation, bulk energy storage for variable energy renewable energy integration and distributed energy storage systems. These batteries are a viable option owing to relatively low cost, ease of manufacture, rapid electrochemical reaction kinetics and good life cycle under controlled conditions [92]. Conventional lead acid batteries typically achieve 20-30 Wh/kg, with a power density of 4 kW/kg [92]. Maintenance free valve-regulated lead-acid (VRLA) batteries, also known as sealed lead acid batteries, have largely replaced conventional high maintenance flooded cell batteries in a variety of applications such as automotive, marine, telecommunications and uninterruptible power supply system. However, for large storage system applications for grid support, flooded lead-acid technology is still considered as the best alternative [93].

The lifetime of lead-acid batteries varies significantly depending on the application, discharge rate and number of deep discharge cycles. In the case of a renewable energy based power system, traditional lead-acid batteries may experience a short life-cycle and require significant maintenance due to uncontrollable charging and discharging operating cycles.

- **Nickel-based batteries**

Nickel-based batteries can be in the form of Nickel/Cadmium (NiCad) and Nickel Metal Hydride (NiMH) systems. The main application for NiCad batteries is portable electronics. Compared with the lead-acid battery, NiCad batteries have a longer life, higher energy density and lower maintenance. NiMH batteries are a feasible alternative to NiCad batteries owing to better performance and environmental benefits. Compared with lead-acid and NiCad batteries, NiMH does not contain toxic substance such as cadmium or lead. The energy density of NiCad cells is 25 - 30% higher than NiCad cells but well below rechargeable Li-ion batteries [94].

- **Lithium-ion batteries**

Lithium is an attractive material for battery technology as it has a higher reduction potential and lighter weight [93]. Rechargeable Li-ion batteries are commonly found in consumer electronic products, comprising most of the global production volume of 10 to 12 Giga-watt hours per year [93]. These batteries are widely used in plug-in hybrid electric vehicles (PHEV) and electric vehicles (EV).

Compared to the long history of lead-acid batteries, Li-ion technology is relatively new. It is expected that the EV and energy storage market will substantially benefited from advancements in Li-ion battery technology. The high energy density and relatively low weight results in a viable choice for electric vehicles and other applications where space and weight are important. Given their long cycle life and compactness, higher roundtrip energy of 85 – 90% [95], Li-ion battery manufacturers may be used for various utility grid-support applications including distributed energy storage systems at community scale, commercial end-user energy management, home back-up energy management systems, frequency regulation and wind and photovoltaic power smoothing applications.

- **Flow batteries**

A flow battery is a rechargeable battery where electrolyte containing one or more dissolved electro-active species flow through an electrochemical cell which converts chemical energy to electricity [93]. Vanadium redox battery technology is one of the most mature flow battery systems available, with an expected life of about 15 years [93]. However, the physical scale of this battery is mainly due to the large volume of electrolyte required when sized for utility-scale projects.

Flow batteries are an attractive energy storage option for the grid because of their ability to store a large amount of energy with a potentially longer life-cycle. However, such technology is still young, with an associated cost barrier. Moreover, the presence of

active species in the anode and cathode electrolytes may lead to efficiency loss and contamination.

- **Sodium sulfur batteries**

The sodium sulfur battery possesses high energy and power density and electrical efficiency. Its long life results in an excellent choice for electric power system applications [93]. Sulfur is used as an active material at the positive electrode and sodium is used at the negative electrodes. Electrodes are separated by sodium-ion-conductive ceramic solid electrolyte. High temperature maintains the electrode active materials in a liquid state while the electrode is solid. This reduces resistance and enables efficient battery performance averaged over lifetime discharge [93].

- **Super-capacitors**

Super-capacitors are devices that store electrical energy as charge separation in porous electrodes with large surface areas. Some key benefits of ultra capacitors include highest capacitance density of any capacitor technology, low cost per farad, reliable, long life, high cycle-life, maintenance-free operation, environmentally safe, a wide range of operating temperatures high power density and good energy density [92].

Of these features, the greater power and energy densities bridge the gap between standard batteries and traditional capacitors for high-power, short-duration energy storage. As a result, they are widely used in utility applications for transmission line stability, spinning reserve, frequency control, voltage regulation, power quality and uninterruptible power supply applications [74].

1.4.2 Mechanical Energy Storage

Pumped hydro, compressed air energy storage and flywheels can be classified as mechanical energy storage.

- **Pumped hydro**

Pumped hydro electric storage is the oldest, most widespread commercially available energy storage technology. Such schemes consist of two large reservoirs at different levels with a store of water. Off-peak electricity is used to pump water up to the top reservoir, which can then be discharged as required, typically to a lower reservoir at the other end of a height differential. This flow of water drives turbines in the same way as hydro-electric dams.

The technology can provide reliable power at short notice, typically within one minute, with efficiency in the range of 70-85% [95]. Overall the technology is one of the most mature on the market and further technological advances are considered unlikely. Pumped hydro is the main form of energy storage globally and has been used since the 1890s. There is approximately 90GW of pumped storage in operation worldwide, accounting for 3% of global generation capacity [96]. A limiting factor is the large capital costs involved in construction (although cost is highly dependent on local topography and other factors). For example, the 1080 MW Goldisthal plant in Germany cost $700 million in 2002 [96].

- **Fly wheel**

Flywheels represent a mechanical form of energy storage in which the kinetic energy of a fast-spinning cylinder contains stored energy. Recent technological advances of fly-wheel have improved the efficiency of the traditional flywheel [93]. Modern flywheel systems are typically comprised of a massive rotating cylinder, supported on a stator by magnetically levitated bearings that eliminate wear and extend system life. To increase efficiency, the flywheel is operated in a low pressure environment to reduce air friction. This energy storage system draws electricity from a primary source to spin the high density cylinder at speeds greater than 20,000 rpm. When the primary source loses its power, the motor acts as a generator. As the flywheel continues to rotate, this generator supplies power to the grid.

Flywheels have a high energy density of 50 – 100 Wh/kg and an efficiency of around 90%, depending on the flywheel's speed range [96]. With no chemical management or disposal to consider, flywheels have certain environmental advantages over battery systems.

- **Compressed air energy storage**

In compressed air energy storage system (CAES), air is compressed into underground mines or caverns by using off-peak electricity, which improves the efficiency of the gas turbine [93]. When required, the compressed air is utilized in conjunction with a gas turbine to generate electricity, resulting in gas consumption reductions of 60% relative to the same amount of electricity generation directly from gas [93]. Compressed air energy storage can be integrated with a wind farm in order to store additional power during high wind conditions. The energy efficiency of CAES is around 80%. The availability or generation of large underground storage spaces can have possible environmental impacts, and constraint on this technology is constrained by the absence of suitable locations for underground air storage.

1.4.3 Electro-magnetic storage

- **Superconducting magnetic energy storage**

Superconducting magnetic energy storage (SMES) can store electrical energy in a magnetic field within a cooled super-conducting coil. The coil is cooled beyond its super-conducting temperature (-269^{o}C), where the resistance of the material is very low. This limited electrical resistance allows SMES to achieve high efficiency of up to 97%. Since the SMES can release immediate energy, It is useful where customers require an extremely high quality power output. As the SMES is currently undergoing research and development, very limited information available regarding costs.

Extremely low temperatures are required for the superconducting system, representing a safety issue. Larger scale SMES systems could require significant protection to deal with magnetic radiation in the immediate vicinity.

1.4.4 Hydrogen Energy Storage

Hydrogen-based energy storage systems are currently receiving considerable attention due to the long period over which hydrogen can be stored, and owing to the potential hydrogen holds for replacing petroleum products as the energy carrier for the transport sector. When coupled with a renewable energy source or low carbon energy technology, hydrogen energy storage has the potential to reduce greenhouse gas emissions.

The essential elements of a hydrogen storage system consist of an electrolyzer unit, to convert electrical input to hydrogen during off-peak periods, the storage component and an energy conversion component to convert the stored chemical energy into electrical energy when demand is high or for use in transportation systems.

The electrolyzer and fuel cell components can be dedicated or “reversible”: capable of electrochemically producing hydrogen or operating in fuel cell mode and converting the hydrogen back to electricity. Proton Exchange Membrane (PEM) fuel cell technology has been most extensively explored for reversible electrolyzer operation, but solid oxide fuel cell (SOFC) and alkaline fuel cell (AFC) technologies can also be applied reversibly. One of the principal concerns regarding hydrogen systems is the whole cycle efficiency. Energy loss is inherent in the system when electricity is converted to hydrogen, stored, transported and then re-converted to electricity in a fuel cell. Estimates of this energy loss range from 60 - 75% [97]. More advanced fuel cell technologies are under development and include: Direct Methanol Fuel Cells (DMFC); Molten Carbonate Fuel Cells (MCFC) and Solid Oxide Fuel Cells (SOFC). MCFCs and SOFCs operate at extremely high temperatures of around 620°C and 1,000 °C respectively. MCFCs are approaching 60% efficiency for the conversion of fuel to

electricity, and it is anticipated that SOFCs will achieve similar efficiency levels [93]. When the waste heat is captured and used, efficiencies can reach 85% for both technologies [93].

1.5 Control Strategy and Energy Management

Proper control and the energy management strategy of stand-alone hybrid power system systems with multiple renewable energy sources and energy storage is absolutely critical in order to achieve a continuous, reliable and cost efficient operation. The overall control and energy management system of a typical hybrid power system is responsible for proper management of energy storage, allowing renewable energy based hybrid system to provide the necessary power to the connected load at any given time of adequate quality.

Typically, in a stand-alone power system, the control system must determine and assign the active and reactive output power of each energy source while maintaining its output voltage and frequency at the desired level. Moreover, the control system has to ensure power supply security of the renewable energy based hybrid power system in case of adverse conditions such as no wind or solar to avoid system black-outs.

1.5.1 Control Structure of Hybrid Power System

The control structure of such systems can be classified into centralized, distributed, and hybrid control paradigms. In all three cases, each energy source is assumed to have its own controller which can determine optimal operation of the corresponding unit, based on current information. A brief description of each control paradigm is discussed in the following:

- **Centralized control paradigm**

In a centralized control paradigm, the measurement signals of all energy units are sent to a centralized controller, as shown in Fig. 1.11. This acts as a supervisory

controller which makes decisions. The main objective of this is to optimize energy use among the various energy sources of the system.

The control signals are then sent to the corresponding energy sources. The advantage of this control structure is that the multi-objective energy management system can achieve global optimization based on all available information. However, the scheme suffers from a heavy computation burden and is subject to single-point failure.

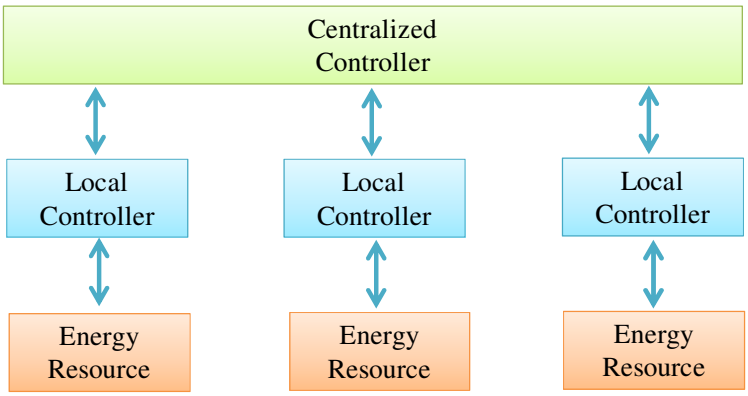

Fig. 1.11. Centralized control paradigm.

- **Distributed control paradigm**

In a fully distributed control paradigm, the measured signals of the energy sources of the hybrid system are sent to their corresponding local controller, as shown in Fig. 1.12. The controllers communicate with one another to make decisions to achieve specific goals. An advantage of this scheme is "plug-and-play operation". With this control structure, the computation burden of each controller is greatly reduced, with no single-point failure problems. The main disadvantage is the potential complexity of its communication system. A promising approach for distributed control problems is the multi-agent system (MAS) [101], and MAS has been used for power system integration, restoration, reconfiguration and power management of micro-grids [100]–[104].

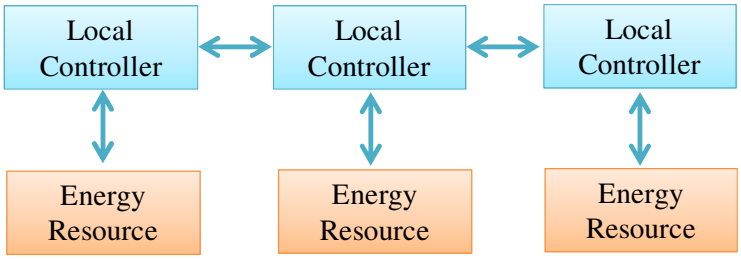

Fig. 1.12. Distributed control paradigm.

- **Hybrid centralized and distributed control paradigm**

The hybrid control paradigm combines centralized and distributed control schemes, as shown in Fig. 1.13 [105], [106]. The distributed energy sources are grouped within a sub-system. A centralized control is used within each group, while distributed control is applied to a set of groups. The computational burden of each controller is reduced, and single-point failure problems are mitigated.

A hybrid control scheme, termed multilevel control framework, is shown in Fig. 1.14. This is similar to the hybrid control scheme discussed above, with an additional supervisory (strategic) control level. At the operational level, basic decisions related to real-time operation are made, and actual control of each energy unit is performed very rapidly based on the unit's control objectives, within a millisecond range. The tactical level aims to make operational decisions for a group of local control units or the entire subsystem, with a relatively higher timeframe, ranging from seconds to minutes. Strategic decisions concerning the system's overall operation such as system "startup" or "shutdown," are made at the top level [107]. Two-way communication exists between the different levels in order to execute decisions.

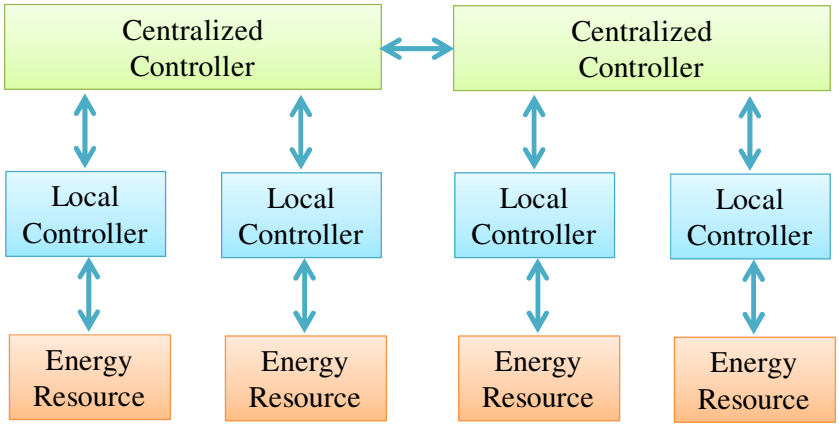

Fig. 1.13. Hybrid centralized and distributed control paradigm.

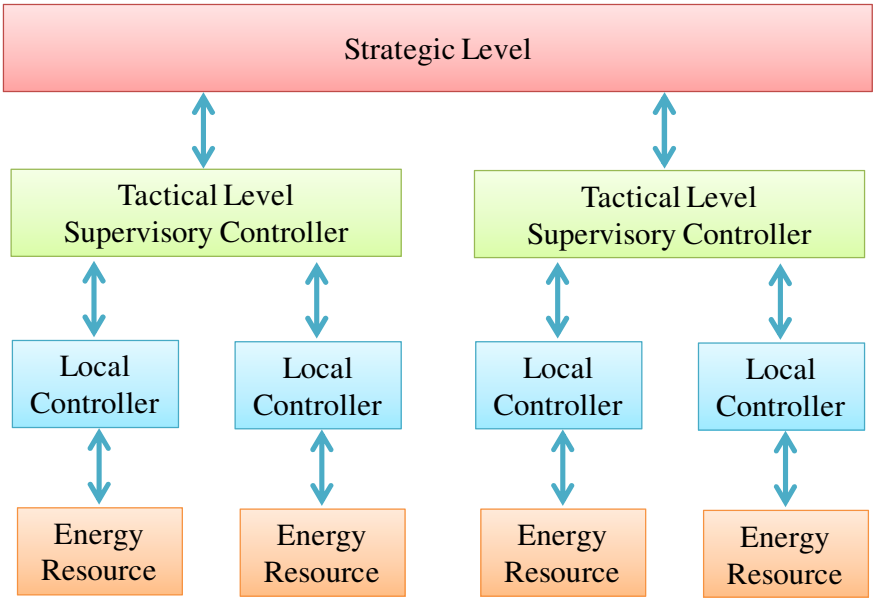

Fig. 1.14. Multi-level control paradigm.

Globally, renewable energy sources have been the fastest growing sources of electricity production in the last decade. According to the projection of the US Energy Information Administration (EIA), non-hydro renewable power generation will continue to grow well in the near future. However, at present, most non-hydroelectric renewable energy technologies are not economically competitive with fossil fuel based generation

sources. As a result, federal and local government incentives are often the primary driving force for installing renewable energy generation plants.

1.6 Challenges for the Fully Renewable Energy based Hybrid Power System Technologies

Although renewable energy sources provide significant benefits to the environment and are recognized as having a good potential for sustainable energy development, they are costly compared to the fossil fuel based power generation system because of high installation costs compared with traditional electricity generation technologies. In the majority of cases, incentives from federal and state governments and local utilities are necessary to make a hybrid system economically viable.

Energy storage is required for stand-alone hybrid renewable energy systems to a have continuous, reliable power supply with desired quality. Energy storage is also one of the enabling technologies for accommodating grid-scale renewable generation sources to power systems at high penetration. Among the different energy storage techniques, only pumped hydroelectric storage and underground CAES can provide a competitive system cost [108]. However, these are heavily constrained geographically and only suitable for large grid-scale energy storage applications. Batteries are the most common energy storage technologies for distributed hybrid renewable energy systems. Though the requirements of energy and power density are not so critical to stationary energy storage applications, system cost and durability remains the key barriers for battery storage systems. Moreover, it is highly challenging to accurately estimate the state of charge (SOC) and state of health (SOH) of batteries [109]–[114]. Therefore, new battery technologies deserve more research attention and efforts to improve their durability and performance, while lowering their cost.

As the deployment of hybrid renewable energy systems in the form of independent stand-alone power systems increases, the need for real-time energy

management of such systems and robust communication between the individual energy sources become important task which require further attention.

Conclusion

This chapter provides a summary of available approaches and those currently under research for optimal design of hybrid renewable energy systems. Different approaches for the configuration, control and energy management of hybrid systems are presented. A detailed review of a wind energy conversion and energy storage systems are presented. Technical and financial challenges of renewable energy based stand-alone systems are also included. In the next chapter, the control strategy of the wind turbine which is considered the primary power source of a proposed hybrid system will be discussed.

Chapter 2

Wind Energy Conversion System Modelling and Control

This chapter focuses on the modelling and control of wind energy conversion systems. The proposed system consists of a variable speed wind turbine, an interior type permanent magnet synchronous generator and a PWM controlled rectifier. The variable speed wind turbine captures aerodynamic power from the wind. The interior type synchronous generator converts this wind power to useable electrical power. The PWM controlled rectifier is used to capture optimum aerodynamic power by controlling the generator's rotor speed. The structure of the wind energy conversion system is shown in Fig. 2.1.

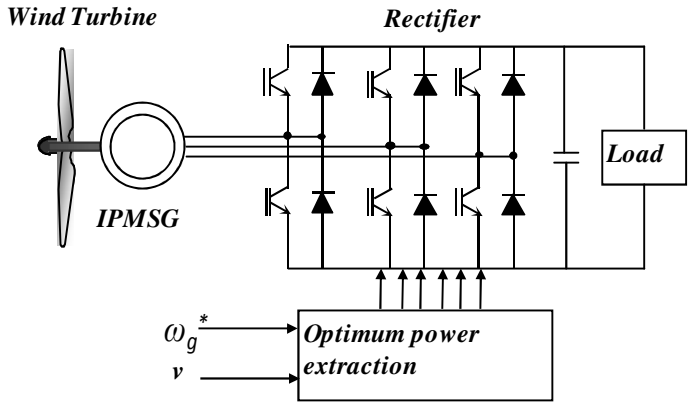

Fig. 2.1. Configuration of wind energy conversion system.

2.1 Variable Speed Wind Turbine Model

A wind turbine basically consists of a blade and generator. The blade transforms the linear kinetic wind energy into rotational kinetic energy, which is then transformed to usable electrical energy with the help of a generator [91]-[96].

The amount of kinetic energy (E) of a small particle having a mass of (m) of wind with a velocity of (v) can be expressed as [91]-[93]:

$$E = \frac{1}{2} m v^2 \tag{2.1}$$

Substituting the particle mass as a product of air density (ρ), wind speed (v), and time (t), that applies a rotor blade of a circular swept area (A) with radius (r), the expression of mass of the air particle can be expressed as [91]-[93]:

$$m = \rho A v t = \rho \pi r^2 v t \tag{2.2}$$

Substituting m from (2.2) in (2.1), the expression of the kinetic energy can be as follows [91]-[93]:

$$E = \rho A v^3 t \tag{2.3}$$

The available power (P_{wind}) is the time derivative of the energy given below [91]-[96]:

$$P_{wind} = \frac{dE}{dt} = \frac{1}{2} \rho A v^3 \tag{2.4}$$

The power coefficient (C_p) is defined as the ratio of the aerodynamic rotor power (P) to the power (P_{wind}) available from the wind as given below [91]-[96]:

$$C_p = \frac{P}{P_{wind}} \tag{2.5}$$

The aerodynamic rotor power can be expressed as a function of aerodynamic torque (τ_{aero}) and rotor angular speed (ω) as given by [91]-[96]:

$$P = \tau_{aero} \omega \tag{2.6}$$

The torque applied to the generator (τ_c) can be given by [91]-[96]:

$$\tau_c = K \omega^2 \tag{2.7}$$

where K is given by

$$K = \frac{1}{2}\rho A R^3 \frac{C_p}{\lambda} \tag{2.8}$$

Assuming that the rotor is rigid, the angular acceleration $\dot{\omega}$ is given by

$$\dot{\omega} = \frac{1}{J}(\tau_{aero} - \tau_e) \tag{2.9}$$

where J is the combined rotational inertial of the rotor, gearbox, generator, and shafts.

Depending on wind speed, a variable-speed wind turbine has three main regions of operation as shown in Fig. 2.2. In region 1, the wind speed is below the cut in speed (v_o) which is not enough to start a turbine. Region 2 is an operational region of wind turbine where the wind speed remains between the cut in speed (v_o) and cut out (v_i) region. In region 3, the turbine must limit the captured wind power as the wind speed is above the cut out speed (v_i), so as to ensure safe electrical and mechanical operating limits.

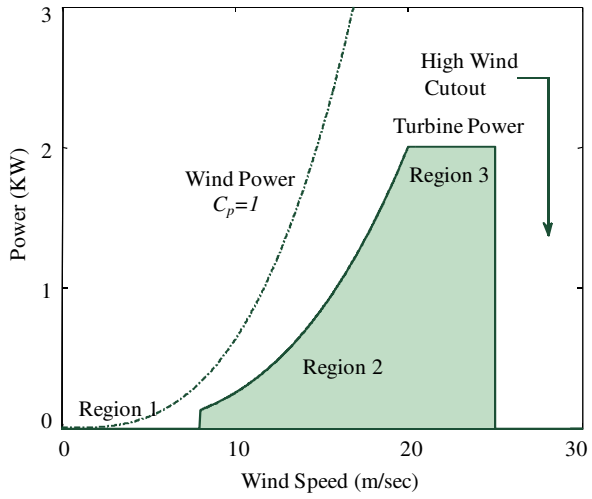

Fig. 2.2 Steady-state power curve of wind turbine.

Fig. 2.2 demonstrates the steady-state relationship between extracted aerodynamic power and wind speed. The dotted line represents the power in the unimpeded wind passing through the rotor swept area, while the solid curve represents the power extracted by a typical variable speed wind turbine.

Classic control techniques such as proportional, integral and derivative (PID) control of blade pitch are typically used to limit power and speed on both the low and high-speed shafts for turbines operating in region 3, while generator torque control is usually used in region 2.

For a variable speed wind turbine operating in region 2, the control objective is to ensure maximum energy capture by operating the wind turbine at the peak of the C_p – TSR as shown in Fig. 2.3. The power coefficient $C_p(\lambda, \beta)$ is a function of the tip speed ration (TSR) λ and the blade pitch β. The TSR is defined as [91]-[96]:

$$\lambda = \frac{\omega R}{v} \tag{2.10}$$

From (2.5), the rotor aerodynamic power P increases with C_p. As a result, the wind turbine should be operated at the maximum power coefficient C_{pmax}.

The relationship between TSR λ and blade pitch can be expressed as follows:

$$\lambda = \frac{1}{\frac{1}{\lambda + 0.02\beta} - \frac{0.03}{\beta^3 + 1}} \tag{2.11}$$

To calculate C_P for the given value of λ and β, the following numerical approximation has been used:

$$C_p(\lambda, \beta) = 0.73\left[\frac{151}{\lambda} - 0.58\beta - 0.002\beta^2 - 13.2\right]\exp\left(\frac{-184}{\lambda}\right) \tag{2.12}$$

From (2.9), the relationship between C_p and λ for different β is shown in Fig. 2.3.

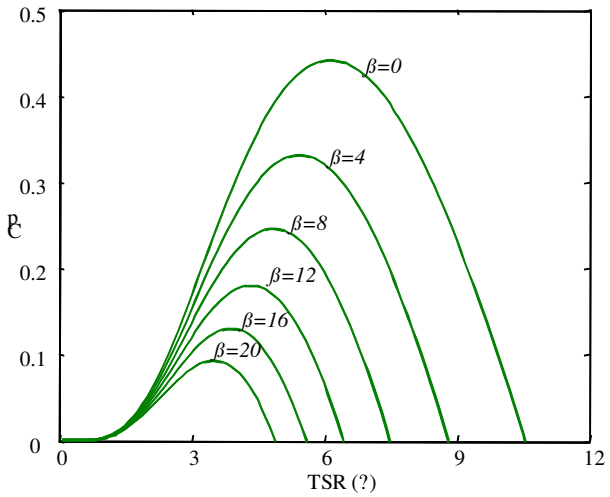

Fig. 2.3. C_p – λ curves for different pitch angles (β).

The steady-state power curve of the wind turbine for different wind speeds is given in Fig. 2.4.

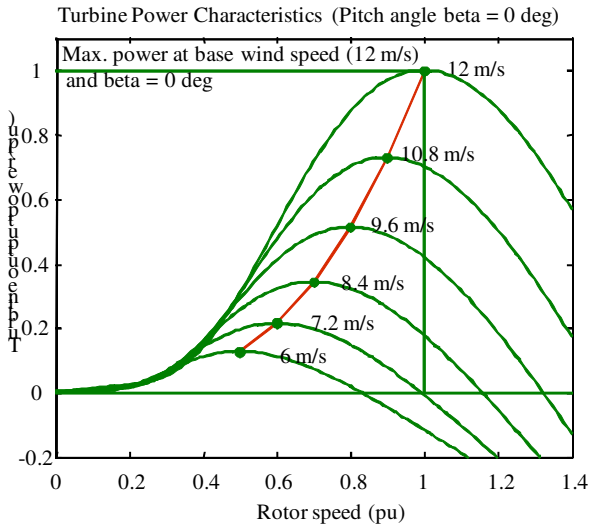

Fig. 2.4. Steady-state power curve of wind turbine at different wind and rotor speed.

2.2 Permanent Magnet Synchronous Generator (PMSG) Model

PMSGs are synchronous ac machines. The PMSG consist of 3-phase stator winding similar to the SCIG, while the rotor winding is replaced by the permanent magnets. The advantage of eliminating the rotor field winding are reduced copper losses, higher power density, lower rotor inertia and more robust rotor construction. The demerits are loss of flexibility in field flux control, possible demagnetization/saturation of magnetic material and parameter variation over time. Depending on the magnet placement on the rotor, PMSGs are divided into two categories: surface permanent magnet machines (SPM) and interior permanent magnet machines (IPM) as shown in Fig. 2.5.

In SPM synchronous machines, the permanent magnets are mounted on the rotor surface as shown in Fig. 2.5(a). The rotor has an iron core which may be solid or made of punched laminations with skewed poles to minimize cogging torque, and the simple design makes it easy to build. This configuration is used for low speed operation, since the magnet may fly during high speed operation. The permeability of magnetic material approximates air, producing an effectively large air gap. Moreover, the smooth rotor surface design minimizes saliency in the rotor, contributing to a low armature reaction effect due to low magnetization inductance.

In IPM synchronous machines, magnets are installed inside the rotor as shown in Fig. 2.5(b). The IPM rotor is difficult to fabricate, although the robust design makes it more suitable for high speed applications. The unequal effective air gap distribution renders it a salient pole machine, where the direct axis inductance is less than quadrature axis inductance (L_d<L_q).

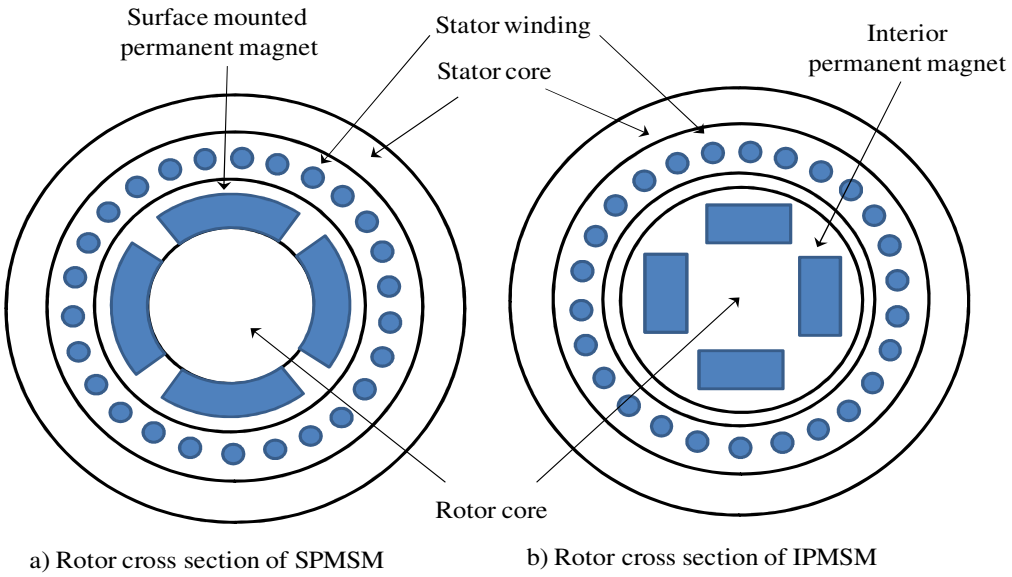

Fig. 2.5. Cross sectional view of rotor design of a) SPMSG and b) IPMSG.

2.2.1 Operating Principle of PMSG

In permanent magnet synchronous machines, magnets are placed on the rotor as alternate *N* and *S* poles. These magnets cause the development of magnetic flux in the air gap. When the stator windings are excited, they develop their own magnetic flux, and the close interaction between rotor and stator magnetic fields produces electromagnetic torque in the rotor.

Fig. 2.6 shows a simplified cross-section view of 3-phase, 2-pole PMSG with symmetrical stator windings, displaced from each other at a 120° electrical angle. The relative motion between rotor and stator induces sinusoidal MMF waves on the magnetic axes of the respective phases. The phase difference between rotor magnetic flux and the magnetic axis of stator phase-a winding is known as rotor position angle (θ_r). The rate of change of rotor position angle further calculates the angular rotor speed (ω_r).

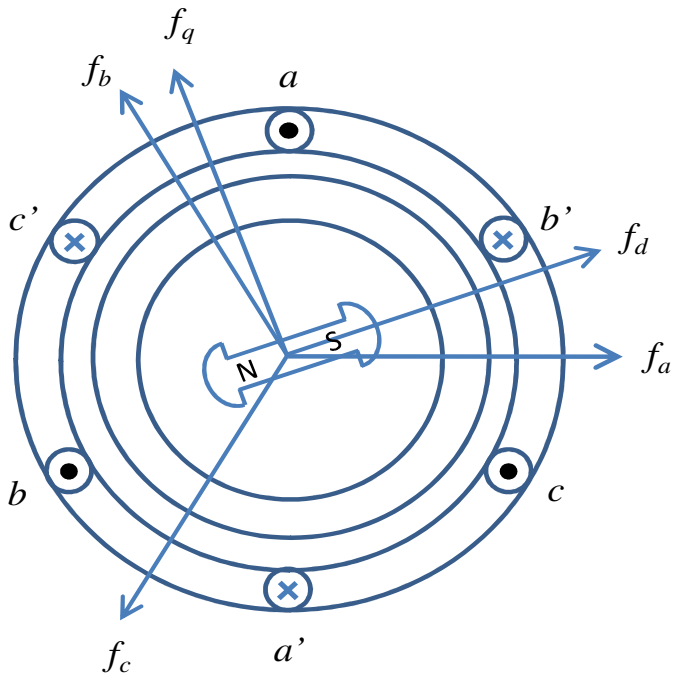

Fig. 2.6. Cross-section view of 3-phase, 2-pole PMSG.

2.2.2 Generalized Model of PMSG

For a PMSG with sinusoidal flux distribution, there is no difference between the back e.m.f. induced by a permanent magnet rotor or wound rotor. Hence, the mathematical model of PMSG is similar to that of a wound rotor synchronous machine.

The PMSG stator voltage equations in *abc* ref. frame can be expressed in terms of instantaneous currents and stator flux linkages as [97]:

$$V_{abc} = R_{sabc} i_{abc} + p.\lambda_{abc} \tag{2.13}$$

where $V_{abc} = [V_a \quad V_b \quad V_c]^T$, $i_{abc} = [i_a \quad i_b \quad i_c]^T$ $\lambda_{abc} = [\lambda_a \quad \lambda_b \quad \lambda_c]^T$, and $R_{sabc} = diag\,[R_s \quad R_s \quad R_s]$

R_s is the stator resistance and p is the differentiating operator d/dt. For a linear magnetic system, the stator flux linkage can be calculated as follows:

$$\lambda_{abc} = L_{abc}\, i_{abc} + \lambda_{mabc} \tag{2.14}$$

where $$L_{abc} = \begin{bmatrix} L_{aa} & L_{ab} & L_{ac} \\ L_{ba} & L_{bb} & L_{bc} \\ L_{ca} & L_{cb} & L_{cc} \end{bmatrix} \tag{2.15}$$

and $$\lambda_{mabc} = \lambda_m \begin{bmatrix} \cos\theta_r \\ \cos\left(\theta_r - \frac{2\pi}{3}\right) \\ \cos\left(\theta_r + \frac{2\pi}{3}\right) \end{bmatrix} \tag{2.16}$$

The stator winding inductances in equation (2.15) can be expressed as:

$$L_{aa} = L_{ls} + L_{0s} + L_{2s}\cos 2\theta_r \tag{2.17}$$

$$L_{bb} = L_{ls} + L_{0s} + L_{2s}\cos 2\left(\theta_r - \frac{2\pi}{3}\right) \tag{2.18}$$

$$L_{cc} = L_{ls} + L_{0s} + L_{2s}\cos 2\left(\theta_r + \frac{2\pi}{3}\right) \tag{2.19}$$

$$L_{ab} = L_{ba} = -\frac{1}{2}L_{0s} + L_{2s}\cos 2\left(\theta_r - \frac{\pi}{3}\right) \tag{2.20}$$

$$L_{ac} = L_{ca} = -\frac{1}{2}L_{0s} + L_{2s}\cos 2\left(\theta_r + \frac{\pi}{3}\right) \tag{2.21}$$

$$L_{bc} = L_{cb} = -\frac{1}{2}L_{0s} + L_{2s}\cos 2\left(\theta_r + \pi\right) \tag{2.22}$$

In the above given equations, L_{aa}, L_{bb}, and L_{cc} are the self inductances of each phase, L_{ab}, L_{bc} and L_{ca} are the mutual inductances and λ_m is the flux linkage established by the rotor magnets. The leakage inductance L_{ls} consists of magnetizing inductance components L_{0s} and L_{2s}, which are further dependent on the rotor position. Here, L_{2s} is generally negative and L_{0s} is positive in the case of an interior permanent magnet (IPM) synchronous machine, due to their unique rotor design. Therefore, the quadrature-axis magnetizing inductance L_{mq} is larger than the direct-axis magnetizing inductance L_{md} of

the interior PM motor, which is the opposite to general salient-pole synchronous machines.

The stator flux linkage in equation (2.14) can be written in extended form as:

$$\begin{bmatrix}\lambda_a\\ \lambda_b\\ \lambda_c\end{bmatrix}=\begin{bmatrix}L_{aa} & L_{ab} & L_{ac}\\ L_{ba} & L_{bb} & L_{bc}\\ L_{ca} & L_{cb} & L_{cc}\end{bmatrix}\begin{bmatrix}i_a\\ i_b\\ i_c\end{bmatrix}+\lambda_m\begin{bmatrix}\cos\theta_r\\ \cos\left(\theta_r-\frac{2\pi}{3}\right)\\ \cos\left(\theta_r+\frac{2\pi}{3}\right)\end{bmatrix} \tag{2.23}$$

2.2.3 Modelling of PMSG in *d-q* Reference Frame

The electromagnetic analysis of a PMSG is conveniently carried out in a *d-q* rotating reference frame, introduced by R. H. Park in the late 1920s. According to Park's transformation, the 3-phase machine is analyzed on the basis of a two – axis theory, where the fictitious direct- and quadrature-axis currents (i_d, i_q) flow through the virtual stator windings. Park's transformation eliminates all time-varying inductances from the voltage equations of the synchronous machine, which occurs due to electric circuits both in relative motion and with varying magnetic reluctance. Park's transformation and its inversion can be mathematically expressed in the following:

$$\begin{bmatrix}f_d\\ f_q\\ f_0\end{bmatrix}=\left(T_{abc\to dq0}\right)\begin{bmatrix}f_a\\ f_b\\ f_c\end{bmatrix}=\frac{2}{3}\begin{bmatrix}\cos\theta_r & \cos\left(\theta_r-\frac{2\pi}{3}\right) & \cos\left(\theta_r+\frac{2\pi}{3}\right)\\ -\sin\theta_r & -\sin\left(\theta_r-\frac{2\pi}{3}\right) & -\sin\left(\theta_r+\frac{2\pi}{3}\right)\\ \frac{1}{2} & \frac{1}{2} & \frac{1}{2}\end{bmatrix}\begin{bmatrix}f_a\\ f_b\\ f_c\end{bmatrix} \tag{2.24}$$

$$\begin{bmatrix}f_a\\ f_b\\ f_c\end{bmatrix}=\left(T_{abc\to dq0}\right)^{-1}\begin{bmatrix}f_d\\ f_q\\ f_0\end{bmatrix}=\begin{bmatrix}\cos\theta_r & -\sin\theta_r & 1\\ \cos\left(\theta_r-\frac{2\pi}{3}\right) & -\sin\left(\theta_r-\frac{2\pi}{3}\right) & 1\\ \cos\left(\theta_r+\frac{2\pi}{3}\right) & -\sin\left(\theta_r+\frac{2\pi}{3}\right) & 1\end{bmatrix}\begin{bmatrix}f_d\\ f_q\\ f_0\end{bmatrix} \tag{2.25}$$

In the equations 2.24 and 2.25, f can represent either voltage, current or flux linkage vector variables. The frame of reference may rotate at any constant or varying

angular velocity or may remain stationary as in the Clark transformation. For a three-phase balanced system, the transformation matrix in 2.24 can be reduced to:

$$\begin{bmatrix} f_d \\ f_q \end{bmatrix} = (T_{abc\to dq}) \begin{bmatrix} f_a \\ f_b \\ f_c \end{bmatrix} = \frac{2}{3} \begin{bmatrix} \cos\theta_r & \cos\left(\theta_r - \frac{2\pi}{3}\right) & \cos\left(\theta_r + \frac{2\pi}{3}\right) \\ -\sin\theta_r & -\sin\left(\theta_r - \frac{2\pi}{3}\right) & -\sin\left(\theta_r + \frac{2\pi}{3}\right) \end{bmatrix} \begin{bmatrix} f_a \\ f_b \\ f_c \end{bmatrix} \tag{2.25}$$

Now the equation 2.13 can be rewritten in rotating reference frame as given below:

$$V_{dq0} = R_s i_{dq0} + T_{abc\to dq0} \cdot p \cdot \left[\left(T_{abc\to dq0} \right)^{-1} \right] \lambda_{dq0} + p.\lambda_{dq0} \tag{2.26}$$

where $V_{dq0} = [V_d \quad V_q \quad V_0]^T$ (2.27)

$$i_{dq0} = [i_d \quad i_q \quad i_0]^T \tag{2.28}$$

$$\lambda_{dq0} = [\lambda_d \quad \lambda_q \quad \lambda_0]^T \tag{2.29}$$

Similarly, the stator flux linkage as calculated in equation 2.14 can be written in rotating reference frame as:

$$\lambda_{dq0} = L_{dq0}\, i_{dq0} + \lambda_{dq0} \tag{2.30}$$

where the magnetizing flux linkage lies in the direction of *d*- axis, and hence can be written in matrix form as below:

$$\lambda_{dq0m} = [\lambda_m \quad 0 \quad 0]^T \tag{2.31}$$

$$L_{dq0} = \begin{bmatrix} L_d & 0 & 0 \\ 0 & L_q & 0 \\ 0 & 0 & L_0 \end{bmatrix} \tag{2.32}$$

$$L_d = L_{ls} + L_{md} = L_{ls} + \frac{3}{2}(L_{0s} + L_{2s}) \tag{2.33}$$

$$L_q = L_{ls} + L_{mq} = L_{ls} + \frac{3}{2}(L_{0s} - L_{2s}) \tag{2.34}$$

$$L_0 = L_{ls} \tag{2.35}$$

Further, the interrelationship between L_d, L_q and L_{0s}, L_{2s} can be given as:

$$L_{md} = \frac{3}{2}(L_{0s} + L_{2s}) \tag{2.36}$$

$$L_{mq} = \frac{3}{2}(L_{0s} - L_{2s}) \tag{2.37}$$

$$L_{0s} = \frac{2}{3}\left(\frac{L_{md}+L_{mq}}{2}\right) = \frac{1}{3}(L_{md} + L_{mq}) \tag{2.38}$$

$$L_{2s} = \frac{2}{3}\left(\frac{L_{md}-L_{mq}}{2}\right) = (L_{md} - L_{mq}) \tag{2.39}$$

where L_d is termed as direct-axis stator inductance and L_q as the quadrature axis stator inductance.

Similarly we can have

$$p \cdot \left[\left(T_{abc\to dq0}\right)^{-1}\right] = \omega_r \begin{bmatrix} -\sin\theta_r & -\cos\theta_r & 0 \\ -\sin\left(\theta_r - \frac{2\pi}{3}\right) & -\cos\left(\theta_r - \frac{2\pi}{3}\right) & 0 \\ -\sin\left(\theta_r + \frac{2\pi}{3}\right) & -\cos\left(\theta_r + \frac{2\pi}{3}\right) & 0 \end{bmatrix} \tag{2.40}$$

Thus, we can have

$$T_{abc\to dq0} \cdot p \cdot \left[\left(T_{abc\to dq0}\right)^{-1}\right] = \omega r \begin{bmatrix} 0 & -1 & 0 \\ 1 & 0 & 0 \\ 0 & 0 & 0 \end{bmatrix} \tag{2.41}$$

Substituting all these terms from equations 2.27 to 2.41 in equation 2.26:

$$\begin{bmatrix} V_d \\ V_q \\ V_0 \end{bmatrix} = \begin{bmatrix} R_S & 0 & 0 \\ 0 & R_S & 0 \\ 0 & 0 & R_S \end{bmatrix} \begin{bmatrix} i_d \\ i_q \\ i_0 \end{bmatrix} + \omega_r \cdot \begin{bmatrix} 0 & -1 & 0 \\ 1 & 0 & 0 \\ 0 & 0 & 0 \end{bmatrix} \begin{bmatrix} L_d & 0 & 0 \\ 0 & L_q & 0 \\ 0 & 0 & L_0 \end{bmatrix} \begin{bmatrix} i_d \\ i_q \\ i_0 \end{bmatrix} + \begin{bmatrix} \lambda_m \\ 0 \\ 0 \end{bmatrix} + p \cdot \begin{bmatrix} 0 & -1 & 0 \\ 1 & 0 & 0 \\ 0 & 0 & 0 \end{bmatrix} \begin{bmatrix} L_d & 0 & 0 \\ 0 & L_q & 0 \\ 0 & 0 & L_0 \end{bmatrix} \begin{bmatrix} i_d \\ i_q \\ i_0 \end{bmatrix} \quad (2.42)$$

Simplifying the equation 2.42 and written in extended form as:

$$V_d = R_S i_d + L_d \frac{di_d}{dt} - \omega_r L_q i_q \quad (2.43)$$

$$V_q = R_S i_q + L_q \frac{di_q}{dt} + \omega_r L_d i_d + \omega_r \lambda_m \quad (2.44)$$

For balanced operation of PMSG, the zero sequence equation can be neglected. The *d*- and *q*- axes equivalent diagram of PMSG is shown in Fig 2.6. Here, E_d and E_q are the back e.m.f. of direct and quadrature axes respectively, which can be expressed as:

$$E_d = -\omega_r \lambda_q = -\omega_r L_q i_q \quad (2.45)$$

$$E_q = \omega_r \lambda_d = \omega_r L_d i_d + \omega_r \lambda_m \quad (2.46)$$

The mechanical power developed inside PMSG can be expressed as:

$$P_m = \frac{3}{2}\left(E_d i_d + E_q i_q\right) = \frac{3}{2}\left(\omega_r \lambda_d i_q - \omega_r \lambda_q i_d\right) \quad (2.47)$$

Similarly, from the above derived equations, the expression for electromagnetic torque in rotating reference frame can be written as:

$$T_e = \frac{P_m}{\omega_m} = \left(\frac{P}{2}\right)\frac{P_m}{\omega_r} \quad (2.48)$$

where ω_m is the mechanical speed and P is the number of poles.

Substituting (2.47) in (2.48), the expression for electromagnetic torque can be re-written as:

$$T_e = \left(\frac{3}{2}\right)\left(\frac{P}{2}\right)\left(\lambda_d i_q - \lambda_q i_d\right) \tag{2.49}$$

Substituting the appropriate values for stator flux linkage from (2.30) in (2.49), the equation for electromagnetic torque can be rewritten as:

$$T_e = \left(\frac{3}{2}\right)\left(\frac{P}{2}\right)\left(\lambda_m i_q - \left(L_q - L_q\right) i_d i_q\right) \tag{2.50}$$

As the PMSG is to be operated in generating mode, the flow of current in stator winding is considered to be the opposite direction and is hence negative. Considering the copper and core loss components of the PMSG, the *d*- and *q*- axes equivalent circuit diagram of PMSG is shown in Fig. 2.7.

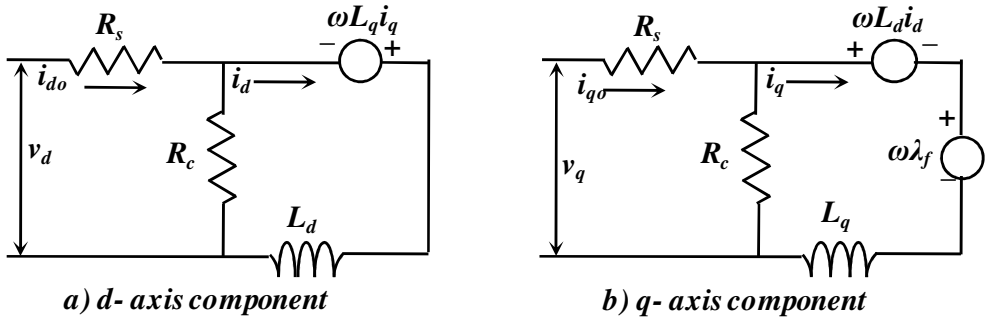

Fig. 2.7. *d*- and *q*- axes equivalent circuit diagram of PMSG.

2.2.4 PMSG Controller Modelling

The primary objective of the PMSG control is to extract optimum power from varying wind. The PMSG controller also ensures efficient operation of the PMSG [97]-[111].

- **Optimum power control**

The optimum power extraction concept can be defined as the extraction of required power from a wind turbine under varying wind conditions [108]-[125]. In a variable speed wind turbine, the relationship between rotor speed and the output power for a given wind speed is shown in Fig. 2.4. The detailed relationship between the rotor speed and the output power for a given wind speed is discussed in the variable speed wind turbine model section.

From (2.6) and (2.7), the applied torque or the extracted power from the wind can be controlled by regulating the rotor speed. By rearranging (2.7), the relationship between the applied torque and the rotor speed can be defined as follows:

$$\tau_{copt} = K_{opt}\omega^2 \tag{2.51}$$

where K_{opt} is given by

$$K_{opt} = \frac{1}{2}\rho A R^3 \frac{C_{popt}}{\lambda} \tag{2.52}$$

The optimum power can be as follows:

$$P_{opt} = \omega\tau_{copt} = K_{opt}\omega^3 \tag{2.53}$$

From (2.53), the rotor speed at optimum power point can be expressed as follows:

$$\omega = \sqrt[3]{\frac{P_{opt}}{K_{opt}}} \tag{2.54}$$

From (2.53), optimum power can be extracted by controlling the rotor speed. Fig. 2.8 demonstrates the power generated by a turbine as a function of the rotor speed for different wind speeds. As an example, for a particular wind speed (v_6), the optimum power (P_{Wopt}) can be generated by keeping the rotor speed either equal to ω_1 or ω_3. However, as ω_3 is higher than the base rotor speed, the control system must choose the

rotor speed ω_1. If the wind speed drops to v_5 from v_6, the control system sets the rotor speed to ω_2 to extract the required power.

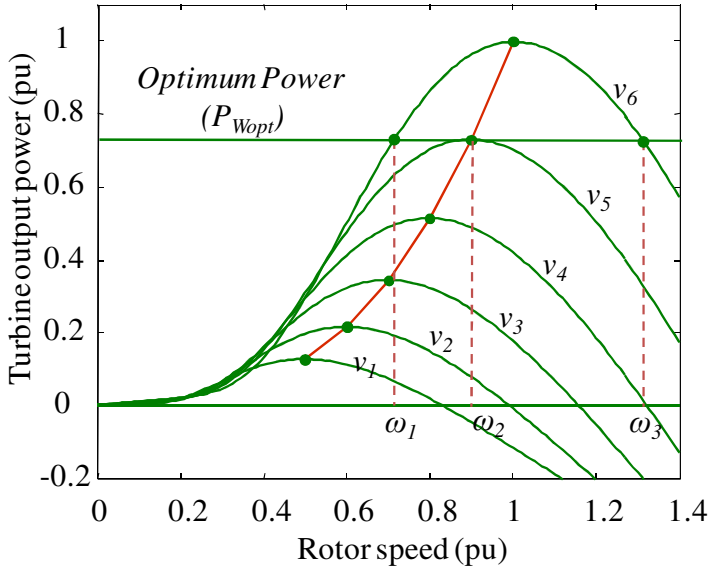

Fig. 2.8. Power generation of wind turbine in different rotor and wind speeds.

- **Efficient operation of PMSG**

Optimum power extraction algorithms can be implemented in wind energy conversion stages in different ways. An unregulated two-level rectifier with a boost or a buck-boost converter is used to regulate the dc-link voltage or rotor speed. This arrangement causes high harmonic distortion which reduces generator efficiency [105]. A regulated two-level rectifier can improve these distortions [105].

The primary objective of the controller is to regulate *d*- and *q*- axis components of the stator current. The reference optimum value of *d*- and *q*- axis current determines the operational loss of the IPMSG. The losses of a PMSG can be divided into four components: stator copper loss, core loss, mechanical loss and stray-load loss. Only the stator copper and core losses are explicitly dependent on the fundamental components of the stator currents. Therefore, optimum reference values of *d*- and *q*- axis components of

stator current have to be calculated to reduce the operation loss. An algorithm is developed to obtain the optimum reference value of *d*- and *q*- axis current to ensure minimum operational loss of IPMSG as discussed in the following.

From (6), the *q*-axis stator current component (i_q) for constant torque can be expressed as a function of the *d*-axis stator current component (i_d):

$$i_q = \frac{2T_g}{3P_m\{\lambda_f + (L_d - L_q)i_d\}} \tag{2.55}$$

The maximum efficiency of the IPM synchronous generator operation can be achieved by minimizing copper and core losses. From Fig. 3, the copper (P_{Cu}) and core (P_{Core}) loss for the IPM synchronous generator can be determined as follows [127], [103]:

$$P_{cu} = R_s\left(i_d^2 + i_q^2\right) \tag{2.56}$$

$$P_{core} = \frac{\omega^2\{(L_d i_d + \psi_f)^2 + (L_q i_q)^2\}}{R_c} \tag{2.57}$$

$$P_{core} = \frac{\omega^2\{(L_d i_d + \psi_f)^2 + (L_q i_q)^2\}}{R_c} \tag{2.58}$$

where R_c is the core loss component.

The output power from the generator can be given as:

$$\begin{aligned} P_{out} &= P_w - P_{Cu} - P_{Core} \\ &= T_g\omega - R_s(i_d{}^2 + i_d{}^2) - \frac{\omega^2\{(L_d i_d + \psi_f)^2 + (L_q i_q)^2\}}{R_c} \end{aligned} \tag{2.59}$$

The optimum value of i_d can be determined from the output power (P_{out}) vs *d*-axis stator current (i_d) curve based on (2.55)-(2.59) as shown in Fig. 2.9. From Fig. 2.9, the

optimum value of the *d*- axis current component is chosen where the output power from IPMSG is maximum. The controller is shown in Fig. 2.10.

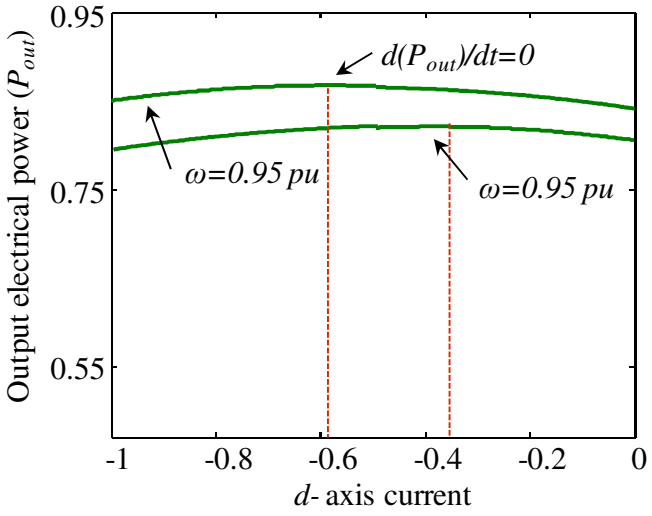

Fig. 2.9. The *d*-axis current vs output electric power.

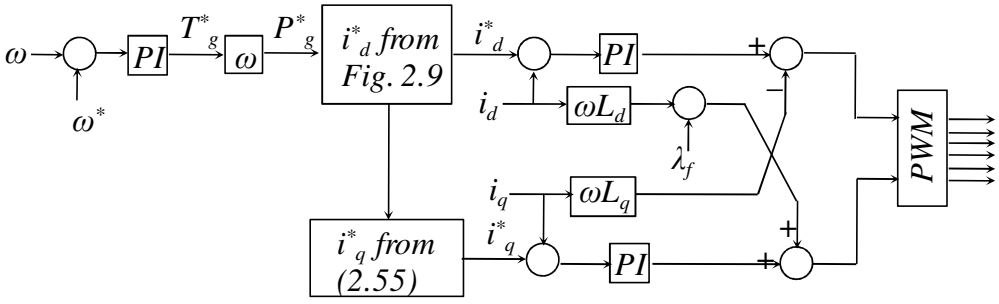

Fig. 2.10. Machine side controller.

2.3 Simulation Results

Simulation studies are conducted to verify the performance of the wind energy conversion system controller. The proposed system shown in Fig. 2.1 is implemented in a Matlab/Simpower environment. The system's performance is simulated for different

wind and load conditions. The parameters of the wind turbine and IPM synchronous generator are shown in Table 2.1.

Table 2.1. Parameters of the wind turbine and IPM synchronous generator.

Permanent Magnet Synchronous Generator	
Number of pole pairs	4
Rated speed (rpm)	1260
Rated power (kw)	1
Stator resistance (ohm)	5.8
Direct inductance (mh)	0.0448
Quadrature inductance (mh)	0.1024
Inertia	0.011
Wind Turbine	
Rated power (kW)	1.1
Base wind speed (m/s)	12

- **Wind and load profile**

Fig 2.11 shows the hypothetical wind and load profiles. The wind speed changes from 10.5 m/sec to 11.1 m/sec at t=10.5 sec; 11.1 m/sec to 11.7 m/sec at t=17.5 sec; and 11.7 m/sec to 10.5 m/sec at t=23 sec. The load changes from 720 watt to 750 watt at t=13.5 sec; from 750 watt to 900 watt at t=17.5 sec; from 900 watt to 800 watt at t=22.5 sec.

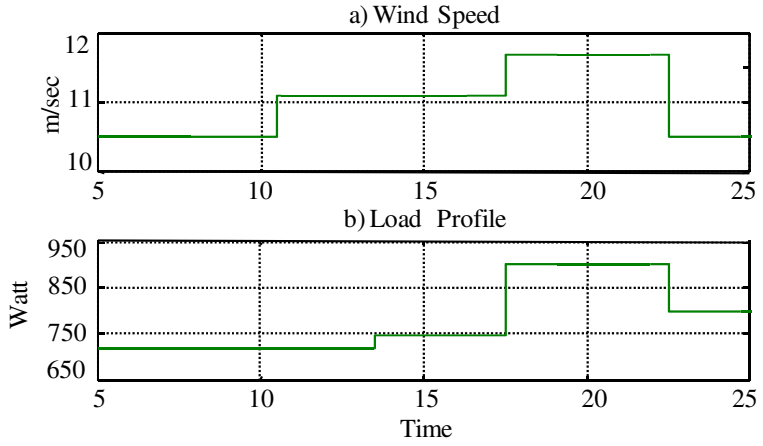

Fig. 2.11. Hypothetical a) wind speed and b) load profile.

- **Machine-side converter performance**

Fig. 2.12 shows maximum power extraction from the wind by regulating the generator speed. From Fig. 2.12, it can be seen that the proposed controller is able to extract maximum power at different wind speeds.

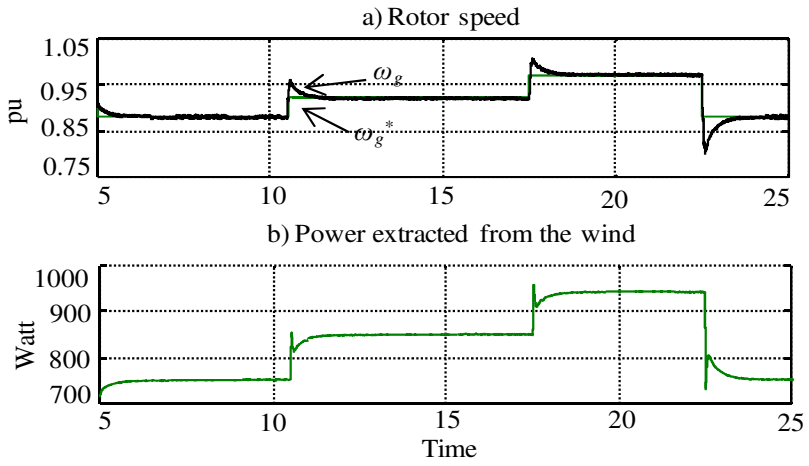

Fig. 2.12. Rotor speed regulation for maximum power extraction.

Fig. 2.13 shows the maximum efficiency operation of the IPM synchronous generator. It is seen that the controller regulates the *d*-and *q*-axis stator currents in order to maintain a high efficiency operation of the IPM synchronous generator.

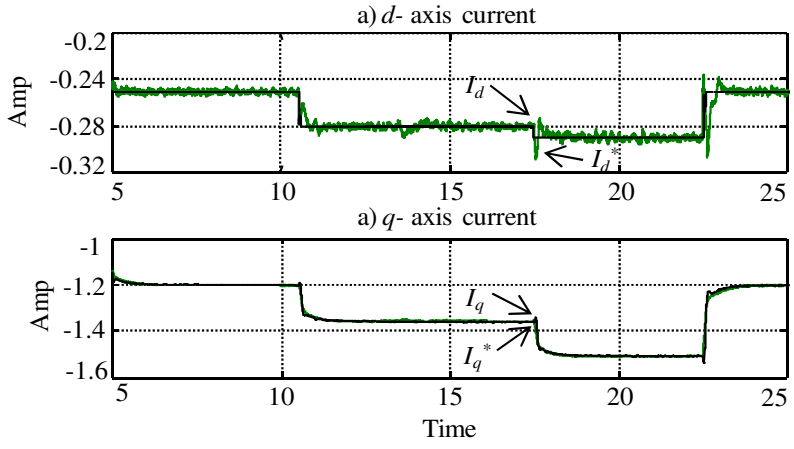

Fig. 2.13. Stator current regulation.

Fig. 2.14 (a) shows the converted electrical power and power loss of the IPM synchronous generator. Fig. 2.14(b) shows that the IPM synchronous generator maintains high efficiency operation.

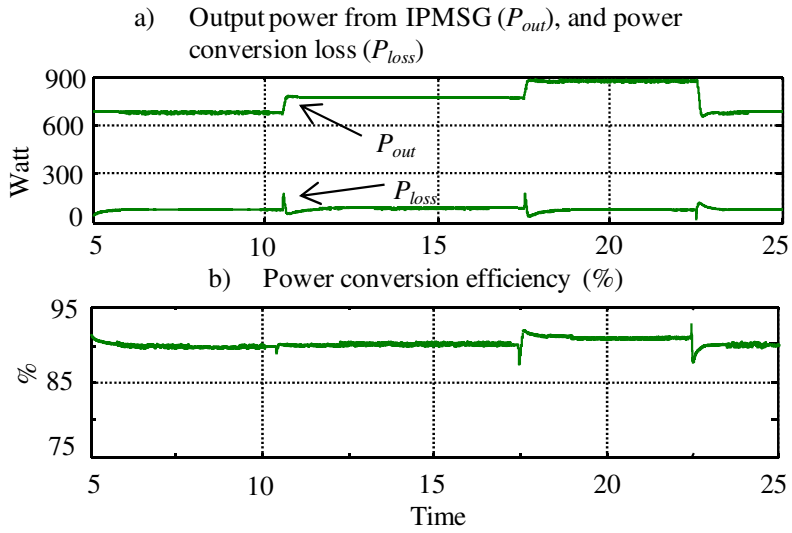

Fig. 2.14. Performance of PMSG.

Conclusion

This chapter outlines the modeling and control aspects of a wind energy conversion system. The optimum wind power is regulated by controlling the rotor speed. To ensure the efficient operation of IPMSG, the *d*- and *q*- axis currents are also controlled. The control system's performance is presented using MATLAB simulation.

Chapter 3

Energy Storage and Inverter System Control

This chapter outlines the modelling and control strategies of *i)* energy storage systems, and *ii)* the load side inverter system of the proposed renewable energy based hybrid stand-alone power system. The proposed energy storage system consists of both hydrogen and battery storage systems. The hydrogen storage system consists of an electrolyzer, hydrogen tank and fuel cell unit. The control systems of energy storage and inverter systems are implemented in a MATLAB/ Simpower environment and results are presented.

3.1 Overview of Energy Storage System

Renewable energy sources such as photovoltaic, solar thermal or wind are inherently intermittent and fluctuating. As a result, proper control and management of the energy storage system is critical for ensuring reliable, continuous operation.

Different energy storage systems such as pumped hydro, compressed air , flywheel , thermal, hydrogen, batteries, superconducting magnetic storage and super-capacitors are used in various applications for different purposes in the proposed wind power based stand-alone power system. The relative advantages and disadvantages of each storage system are discussed in the introductory chapter. In this project, adopting a combination of the fuel cell, electrolyzer and battery is considered for various reasons. Firstly, excess power from wind can either be stored in the battery storage system or used to generate hydrogen via the electrolyzer. Secondly, batteries respond very quickly [137], [138], ensuring better hybrid system stability during transient periods in the event of sudden wind and load changes. Thirdly, this combination can improve the system's efficiency by sharing power such as to allow the operation of a fuel cell in a high efficiency region. In

the following, the control strategy, battery energy and hydrogen storage system will be presented.

3.2 Battery System Modelling and Control

3.2.1 Battery System Modelling

In the proposed project, lead-acid batteries have been chosen for their ability to improve the system during transient stability and to support it with bulk energy. A lead-acid battery is an electrical storage device that uses a reversible chemical reaction to store energy. The charging and discharging equations are shown below [139]-[141]:

Discharging mode:

$$V_{batt} = E_0 - Ri - K\frac{Q}{Q-it}(it + i^*) + A\exp(t) \tag{3.1}$$

Charging mode:

$$V_{batt} = E_0 - Ki - K\frac{Q}{it-0.1Q}i^* - K\frac{Q}{Q-it}it + A\exp(t) \tag{3.2}$$

where V_{batt} is the battery output voltage (V); E_0 is the battery constant voltage (V); K is the polarization constant ($V/(Ah)$) or polarization resistance (Ω); Q is the battery capacity (Ah); $it = \int idt$ is the actual battery charge (Ah); A is the exponential zone time constant inverse $(Ah)^{-1}$; R is the internal resistance (Ω); i is the battery current (A); i^* is the filtered current (A).

The state-of-charge (SOC) is defined as the available capacity remaining in the battery, expressed as a percentage of the rated capacity. The SOC is defined as [139]:

$$SOC = 100\left(1 - \frac{\int idt}{Q}\right)\% \tag{3.3}$$

The following assumptions are considered of the model [139], [140]:

- The internal resistance is assumed to be constant during charging and discharging cycles and does not vary with current amplitude.
- The model's parameters are deduced from the discharge characteristics and assumed to be the same for charging.
- The battery capacity does not change with the amplitude current.
- The temperature does not affect the model's behaviour.
- The battery has no memory effect.

3.2.2 Battery System Control

A bidirectional dc-dc converter [142] – [151] is a popular interface circuit shown in Fig. 3.1, which is used to regulate charging and discharging of the battery storage system. During the charging cycle, the converter works as a boost converter while operating as a buck converter during the discharging cycle. The boost converter operation is achieved by modulating Q_2 switch with anti-parallel diode D_1. With the direction of power supply reserve, the converter works as a buck converter through the modulation of Q_1 switch with anti-parallel diode D_2.

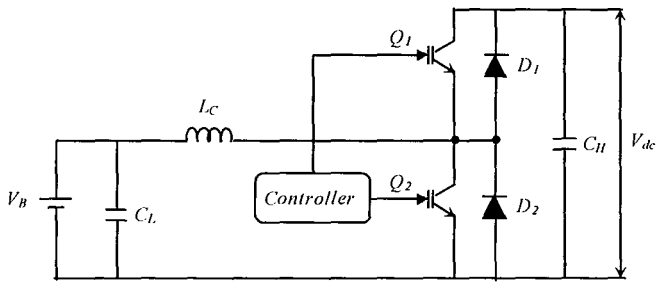

Fig. 3.1. Bidirectional dc-dc converter.

The bidirectional dc-dc converter must be operated in a continuous condition mode for charging and discharging applications. Switches Q_1 and Q_2 are switched so that the converter operates in a steady state with four sub-intervals. These are intervals 1 ($t_0 \rightarrow t_1$); 2 ($t_1 \rightarrow t_2$); 3 ($t_2 \rightarrow t_3$); and 4 ($t_3 \rightarrow t_4$). During intervals 1 and 2, the converter

works as a boost-converter in battery charging mode, while during interval 3 and interval 4, the converter works as a buck-converter in battery discharging mode. It should be noted that the low voltage battery side is considered as V_B and the high voltage dc-link voltage as V_{dc}. A brief description of the operation of four different interval times is below:

Interval 1($t_0 \rightarrow t_1$)

At the time of $t_0 \rightarrow t_1$ the lower switch Q_2 is ON and upper switch Q_1 is OFF with diode D_1 and D_2 on reversed bias as shown in Fig. 3.2. During this time, the inductor is charged and the current through the inductor increases. The battery voltage (V_B) and the increased inductor current $(\Delta i_B(+))$ are expressed as follows:

$$V_B = L_C \frac{di_B}{dt} = L_C \frac{\Delta i_B}{\Delta T} \tag{3.4}$$

$$\Delta i_B(+) = \frac{V_B}{L_C} T_{ON} \tag{3.5}$$

where T_{ON} is the on time of lower switch Q_2.

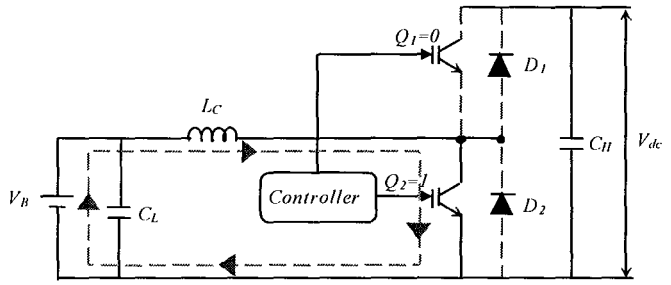

Fig. 3.2. Bidirectional dc-dc converter operation (time interval t_0-t_1).

Interval 2($t_1 \rightarrow t_2$)

At the time of $t_1 \rightarrow t_2$ switches Q_1 and Q_2 are OFF. The diode D_1 of the upper switch Q_1 conducts as shown in Fig. 3.3. In this condition, the inductor current starts

decreasing. The decrease of the induction current decreases $(\Delta i_B(-))$ during the off state, given by:

$$\Delta i_B(-) = \frac{(V_{dc}-V_B)}{L_C} T_{OFF} = \frac{(V_{dc}-V_B)}{L_C}(T - T_{ON}) \tag{3.6}$$

where T_{OFF} is the OFF time of lower switch Q_2. T is the total time of operation.

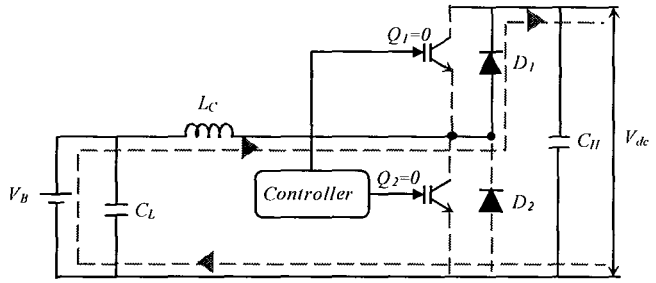

Fig. 3.3. Bidirectional dc-dc converter operation (time interval t_1-t_2).

In steady state operation, $\Delta i_B(+)$ during ON time and $\Delta i_B(-)$ during OFF time has to be equal. Consequently, (3.5) and (3.6) are equated as follows:

$$\frac{V_B}{L_C} T_{ON} = \frac{(V_{dc}-V_B)}{L_C}(T - T_{ON}) \tag{3.7}$$

From (3.7), the relationship between battery voltage (V_B) and dc link voltage (V_{dc}) as a function of duty ration can be expressed as:

$$V_B = DV_{dc} \tag{3.8}$$

where $D = \frac{T_{ON}}{T}$

Interval 3 ($t_2 \rightarrow t_3$)

At time of $t_2 \rightarrow t_3$ the upper switch Q_1 is ON and lower switch Q_2 is OFF with diode D_1 and D_2 on the reversed bias, as shown in Fig. 3.4. During this interval, the

converter works as a buck converter. The inductor current increases, expressed as follows:

$$\Delta i_B(+) = \frac{(V_{dc} - V_B)}{L_C} T_{ON} \tag{3.9}$$

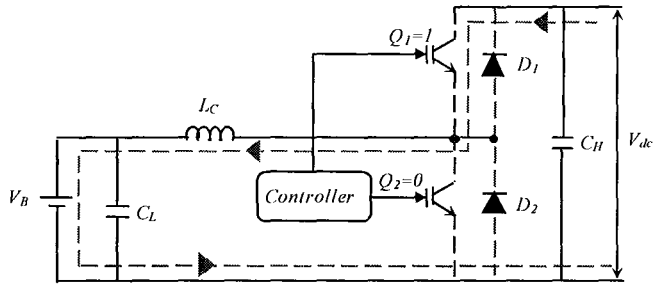

Fig. 3.4. Bidirectional dc-dc converter operation (time interval t_2-t_3).

Interval 4 ($t_3 \rightarrow t_4$)

At time of $t_3 \rightarrow t_4$, both upper switch Q_1 and lower switch Q_2 are OFF and the diode D_2 of the lower switch conducts as shown in Fig. 3.5. During this interval, the converter works as a buck converter. The inductor current decreases, expressed as follows:

$$\Delta i_B(-) = \frac{V_B}{L_C} T_{OFF} = \frac{V_B}{L_C}(T - T_{ON}) \tag{3.10}$$

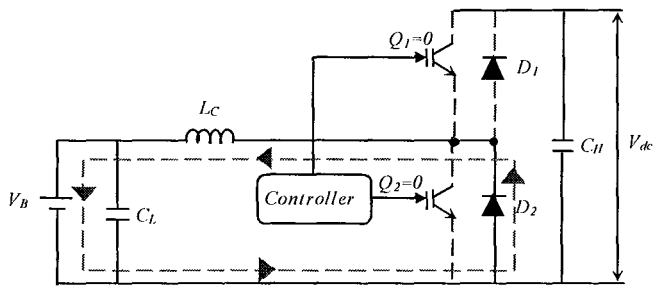

Fig. 3.5. Bidirectional dc-dc converter operation (time interval t_3-t_4).

In steady state operation, $\Delta i_B(+)$ during ON time and $\Delta i_B(-)$ during OFF time have to be equal. As a result, (3.9) and (3.10) are equated as follows:

$$\frac{(V_{dc}-V_B)}{L_C}T_{ON} = \frac{V_B}{L_C}(T - T_{ON}) \tag{3.11}$$

From (3.11), the output voltage can be expressed as a function of duty ration as:

$$V_{dc} = \frac{1}{1-D}V_B \tag{3.12}$$

where $D = \frac{T_{ON}}{T}$

The gate pulse Q_1 and Q_2 are shown in Fig. 3.6.

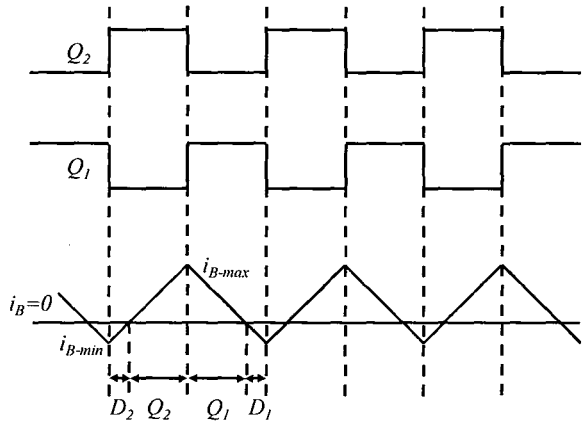

Fig. 3.6. Control of the bidirectional dc-dc converter.

The inductor value is crucial for operation of the bi-directional dc-dc converter in conduction mode. This mode of operation depends on input and output voltage and current, duty cycle frequency and inductor value. The value of the inductor is as follows:

$$L = \frac{V_B(V_{dc}-V_B)}{i_B f_s V_{dc}} \tag{3.13}$$

where f_s is the switching frequency.

The control circuit of the bi-directional dc-dc converter is shown in Fig. 3.7. The control circuit consists of the voltage and current regulator. In the outer loop, a reference current signal is generated based on the voltage error. The battery current signals are also compared. Based on the error signal, the *PI* controller generates the appropriate value to generate a suitable pulse-width modulation (PWM) signal for the switch.

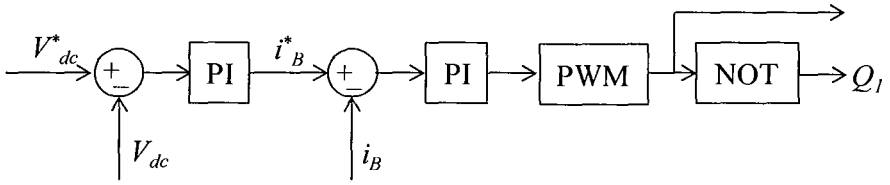

Fig. 3.7. Control of the bidirectional dc-dc converter.

3.2.3 Simulation of Battery Controller

The battery controller system performance is simulated in a MATLAB environment and results are presented. The overall system is shown in Fig. 3.8. The parameters of the battery system and controller are shown in Table 3.1.

Table 3.1. Parameters of battery system and controller

Number of batteries in series	5
Number of batteries in parallel	8
Rated Voltage (volt)	12
Rated Current (Amp)	0.5
Rated Capacity (amp-hour)	0.1
Inductor (mhenry)	2.7
Capacitor (micro Farad)	64
Switching frequency (k Hz)	20

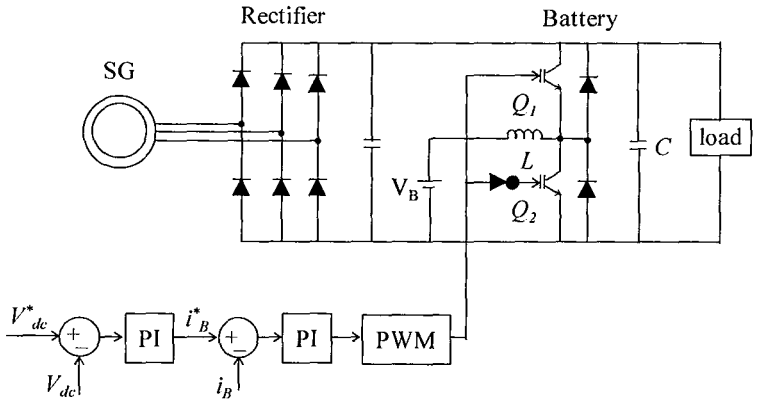

Fig. 3.8. A battery storage system with control.

From Fig. 3.8, a synchronous generator with constant power output is connected to the load via a back-to-back converter. A battery storage system is connected via a bi-directional dc-dc converter in the dc-link. The bi-directional converter is controlled so that the output dc-voltage is constant during different loading conditions.

In the simulation study, the synchronous generator's power is assumed to be constant (2.7 kW). However, the load is variable, and the load profile is shown in Fig. 3.9. From Fig. 3.9, it is seen that the initial load is 0.65 kW. The load changes from 0.65 kW to 2kW at a time of 5 seconds; from 2 kW to 3.5 kW at 8 seconds; from 3.5 kW to 2.25 kW at 11 seconds; and 2.25 kW to 0.75 kW at 14 seconds.

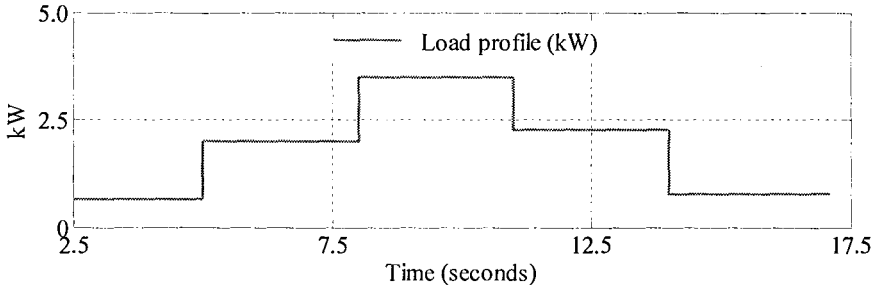

Fig. 3.9. Load profile.

The battery charging and discharging power is shown in Fig. 3.10. It is seen that from 2.5 to 8 seconds the battery charges, as the load requirement is less than the synchronous machine's power generation. However, from 8 to 11 seconds the battery discharges, as the load requirement is higher than generated power. From 11 seconds onwards, the battery charges again as the load demand is less than the power generated by the synchronous generator.

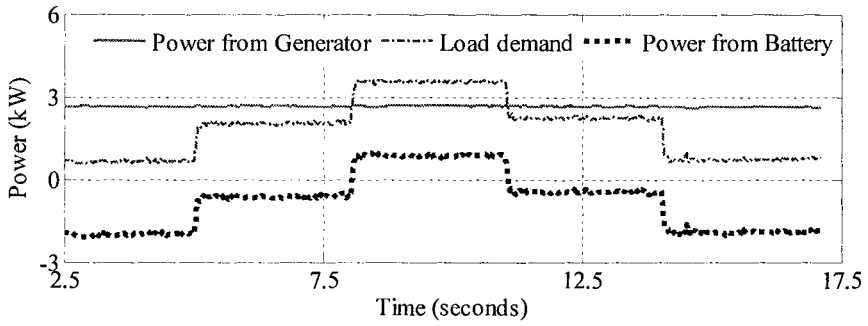

Fig. 3.10. Battery storage system charging and discharging..

The battery voltage, current and state of charge (SOC) as a result of charging and discharging actions are shown in Figs 3.11, 3.12 and 3.13. The dc-link voltage is shown in Fig. 3.14.

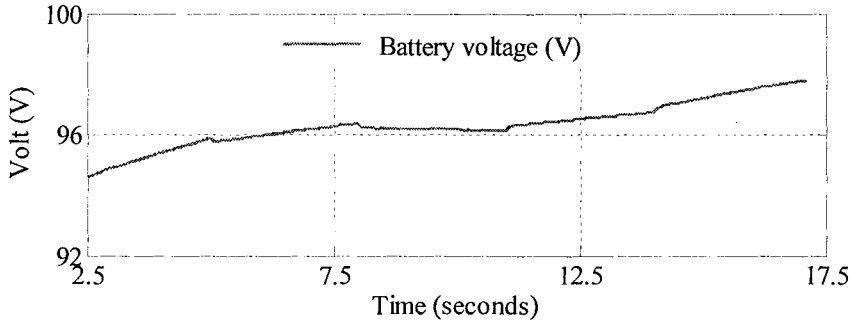

Fig. 3.11. Battery voltage.

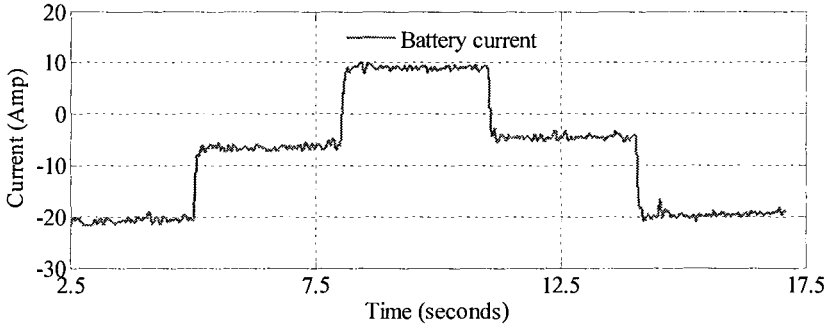

Fig. 3.12. Battery current.

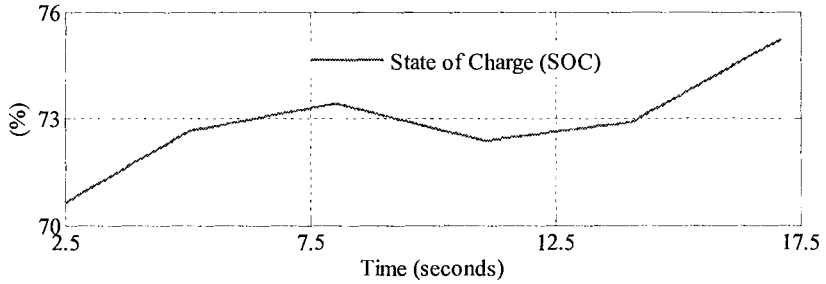

Fig. 3.13. SOC of battery storage system.

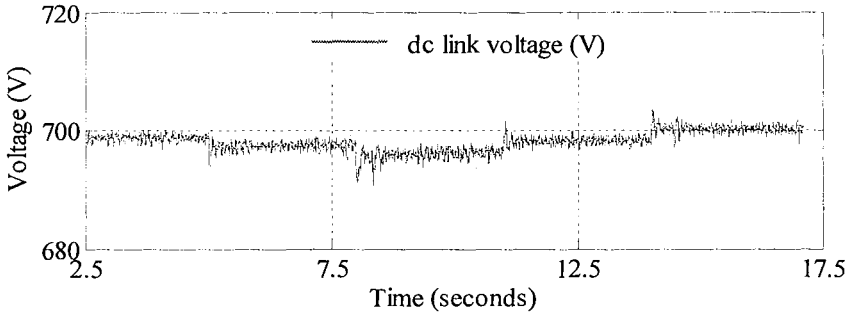

Fig. 3.14. dc link voltage.

From Figs 3.9 to 3.14, it is shown that the dc-dc bi-directional converter controller can balance the power difference of the synchronous generator and load demand.

3.3 Hydrogen Storage System Modelling and Control

The overall hydrogen storage system consists of electrolyzer, fuel cell and hydrogen tank as shown in Fig. 3.15. The electrolyzer and the fuel cell are connected to the dc bus by power electronic interface circuits. The fuel cell and electrolyzer are controlled by the fuel cell and electrolyzer controller as shown in Fig. 3.15, and the hydrogen tank is connected to the electrolyzer and fuel cell. The modelling and control system strategies of electrolyzer, fuel cell and hydrogen tank are as follows:

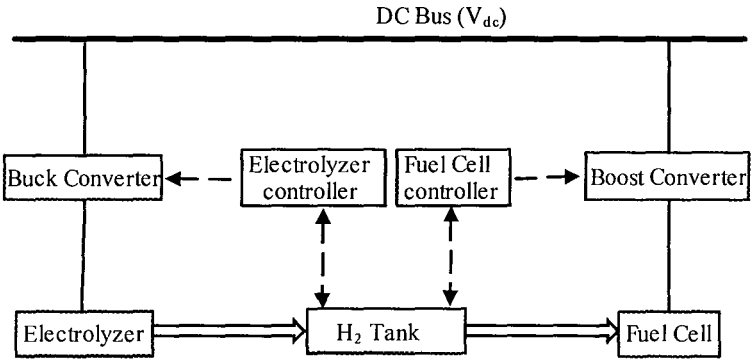

Fig. 3.15. Hydrogen storage system.

3.3.1 Fuel Cell Modelling and Control

The proton exchange membrane (PEM) fuel cells have shown great promise for use as distributed generation sources [152]-[161]. The PEMFCs are a good source of power, providing a reliable supply at a steady state. However, they cannot respond to electric load transients as rapidly as desired, due to slow internal electro-chemical and thermodynamic reactions. The PEM fuel cell is shown in Fig. 3.16 [152], [153].

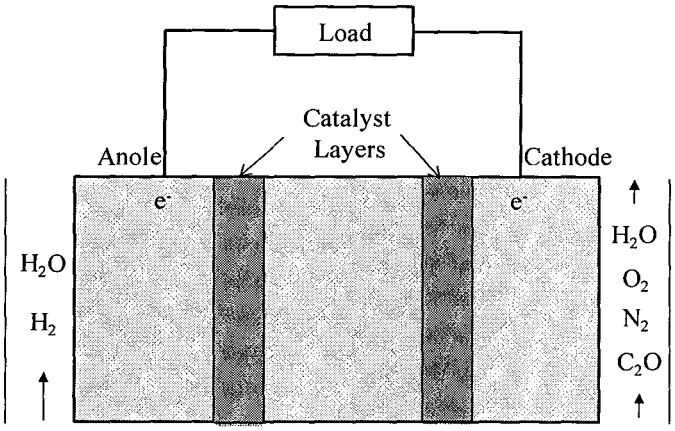

Fig. 3.16. PEM fuel cell.

The overall reaction of PEMFC can be written as:

$$H_2 + \frac{1}{2}O_2 = H_2O_{(l)} \tag{3.14}$$

where H_2, O_2, and $H_2O_{(l)}$ are hydrogen, oxygen and water (in liquid state) molecule, respectively.

The corresponding Nernst equation is used to calculate the reversible potential [152], [153]:

$$E_{cell} = E_{0,cell} + \frac{RT}{2F} ln\left[\frac{p_{H2}.(p_{O2})^{0.5}}{(p_{H2O})^{0.5}}\right] - E_{d,cell} \tag{3.15}$$

where p_{H2}, p_{O2}, and p_{H2O} are the partial pressure of hydrogen, oxygen and water; $E_{o,cell}$ is the reference potential of the cell; R is the gas constant equal to 8.3143 J/(mol.K), and F is the Faraday constant equal to 96487 coulombs/mol.

The terms p_{H2}, p_{O2}, and p_{H2O} can be expressed using the following differential equation [152], [153]:

$$\begin{cases} p_{H2} = \frac{1}{\tau_{H2}}\left\{p_{H2} + \frac{1}{K_{H2}}\left(q_{H2}^{in} - 2K_r I\right)\right\} \\ p_{H2O} = \frac{1}{\tau_{H2O}}\left\{p_{H2O} + \frac{2}{K_{H2O}}\left(2K_r I\right)\right\} \\ p_{O2} = \frac{1}{\tau_{O2}}\left\{p_{O2} + \frac{1}{K_{O2}}\left(q_{O2}^{in} - 2K_r I\right)\right\} \end{cases} \tag{3.16}$$

where K_{H2}, K_{H2O}, and K_{O2} are constants. K_r is a constant, which can be defined by the relationship between the rate of reactant hydrogen (q_{H2}^r) and the fuel cell current [10].

$$q_{H2}^r = \frac{N_{cell} I}{2F} = 2K_r I \tag{3.17}$$

The reference potential is a function of temperature and can be expressed as follows:

$$E_{0,cell} = E_{0,cell}^0 - k_E(T - 298) \tag{3.18}$$

where $E_{0,cell}^0$ is the standard reference potential at standard state (298^{O}K and 1-atm pressure).

From (3.2), the term $E_{d,cell}$ is developed due to the overall effect of the fuel and oxidant delay. The steady-state value of $E_{d,cell}$ is zero. However, during transient it affects the output voltage. The expression of $E_{d,cell}$ is as follows [152], [153]:

$$E_{d,cell} = \lambda_e\left[i(t) - i(t) * \exp\left(-\frac{t}{\tau_e}\right)\right] \tag{3.19}$$

The internal reversible potential (E) developed by the fuel cell can be expressed as [152], [153]:

$$E = N_{cell} E_{cell} = E_0^0 + f_1(I, T) + f_1(I) \tag{3.20}$$

where $E_0^0 = N_{cell} E_{0,cell}^0$; (3.21)

$$f_1(I,T) = \frac{N_{cell}RT}{2F} ln\left[\frac{p_{H_2}(p_{O_2})^{0.5}}{(p_{H_2O})^{0.5}}\right] - N_{cell}k_E(T-298); \quad (3.22)$$

$$f_2(I) = N_{cell}E_{d,cell} \quad (3.23)$$

where N_{cell} is the number of cells in the stack.

Fig. 3.17 shows the electrical circuit diagram for internal reversible potential.

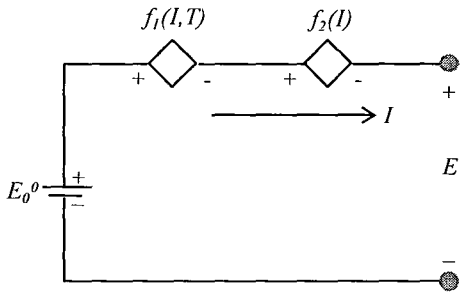

Fig. 3.17. Electrical circuit for internal reversible potential E.

Under normal operating conditions, due to losses the fuel cell output voltage is less than E_{cell}. These losses are determined by activation loss, ohmic resistance voltage drop and concentration over-potential voltage drop. The voltage losses across the fuel cell are as follows:

- **Activation voltage drop**

The activation voltage (V_{act}) drop is calculated using the Tafel equation as follows [152], [153]:

$$V_{act} = \frac{RT}{\alpha zF} ln\left(\frac{I}{I_0}\right) = T.[a + b.ln(I)] = V_{act1} + V_{act2} \quad (3.24)$$

where α is the electron transfer coefficient, z is the number of electron particles and a and b are the constant terms (volts/Kelvin) in the Tafel equation.

From Eq. (3.9), the activation voltage drop has two components. The first component (V_{act1}) is affected by the internal PEM fuel cell temperature as mentioned below [152], [153]:

$$V_{act1} = T.a = \eta_0 + (T - 298)\, a \tag{3.25}$$

where η_0 is the temperature invariant part of activation voltage drop.

The second component of activation voltage drop depends on both temperature (T) and current(I). As a result, the equivalent resistance (R_{act}) corresponding to V_{act2} can be expressed as follows [152]-[153]:

$$R_{act} = \frac{V_{act2}}{I} = \frac{T.b.\ln(I)}{I} \tag{3.26}$$

Fig. 3.18 represents an electrical circuit diagram for activation voltage drop.

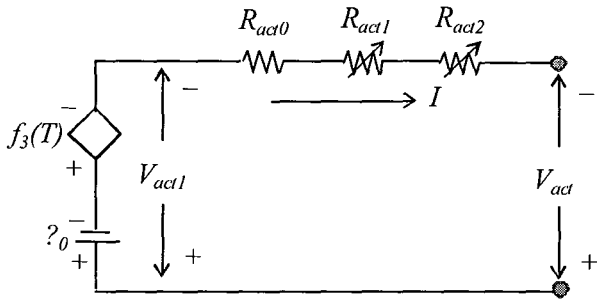

Fig. 3.18. Electrical circuit for activation voltage drop.

- **Ohmic voltage drop**

The ohmic resistance of a PEM fuel cell is the resistance of polymer membrane($V_{ohm,a}$), the conduction resistance between membrane and electrodes ($V_{ohm membrane}$) and resistance of the electrodes($V_{ohm,c}$). The overall ohmic voltage drop can be expressed as [152]-[153]:

$$V_{ohm} = V_{ohm,a} + V_{ohm,membrane} + V_{ohm,c} = IR_{ohm} \tag{3.27}$$

where R_{ohm} is also a function of current and temperature as below [152]-[10]:

$$R_{ohm} = R_{ohm0} + k_{RI}I - k_{RI}T \tag{3.28}$$

where R_{ohm0} is the constant part of R_{ohm}.

Fig. 3.19 represents an electrical circuit diagram for ohmic voltage drop.

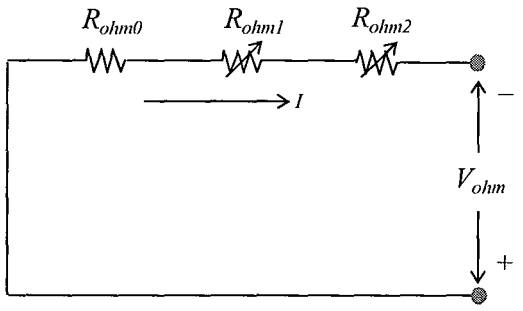

Fig. 3.19. Electrical circuit for ohmic voltage drop.

- **Concentration voltage drop**

During the reaction process, concentration gradients can be formed due to mass diffusions from the flow channels to the reaction sites. At high current densities, slow transportation of the reactant (products) to (from) the reaction sites is the main reason for the concentration voltage drop(V_{conc}). The concentration over-potential in the fuel cell is defined as [152], [153]:

$$V_{conc} = -\frac{RT}{zF}\ln\frac{C_S}{C_B} \tag{3.29}$$

where C_S is the surface concentration and C_B is the bulk concentration.

According to the Fick's First Law, Eq. (3.29) can be rearranged as:

$$V_{conc} = -\frac{RT}{zF} ln\left(1 - \frac{i}{i_{limit}}\right) \tag{3.30}$$

The equivalent resistance for the concentration loss is:

$$R_{conc} = \frac{V_{conc}}{i} = -\frac{RT}{zFi} ln\left(1 - \frac{i}{i_{limit}}\right) \tag{3.31}$$

Fig. 3.20 represents a electrical circuit diagram for concentration voltage drop.

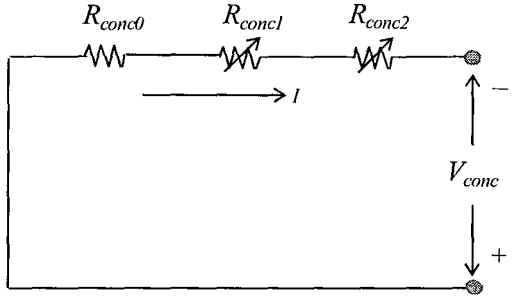

Fig. 3.20. Electrical circuit for concentration voltage drop.

- **Double layer charging effect**

From Fig. 3.16, the two electrodes are separated by a solid membrane which only allows the H^+ ions to pass, which blocking electron flow. The electrons will flow from the anode through the external load and gather at the surface of the cathode, to which the protons of hydrogen will be simultaneously attracted. Thus, two charged layers of opposite polarity are formed across the boundary between the porous cathode and membrane. This layer is known as the electro-chemical double layer which can store electrical energy and behave as a super-capacitor. The equivalent fuel cell circuit considering this effect is shown in Fig. 3.21.

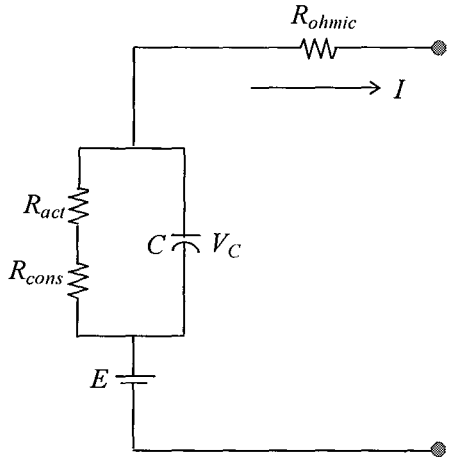

Fig. 3.21. Equivalent circuit of the double-layer charging effect of PEM fuel cells.

From Fig. 3.6, C is the equivalent capacitor due to the double-layer charging effect. Since the PEM fuel cell electrodes are porous, the capacitance C can be very large, and in the order of several Farads. The voltage across the C can be expressed as follows [152], [153]:

$$V_C = \left(I - C\frac{dV_C}{dt}\right)(R_{act} + R_{conc}) \tag{3.32}$$

The double-layer charging effect is integrated into the model by using V_C instead of V_{act2} and V_{conc}. The output voltage can be expressed as follows:

$$V_{out} = E - V_C - V_{act1} - V_{ohm} \tag{3.33}$$

The output power of the fuel cell can be written as follows:

$$P_{out} = V_{out} I \tag{3.34}$$

The *V-I* and *power–current* characteristics of a fuel cell can be seen in Fig. 3.22.

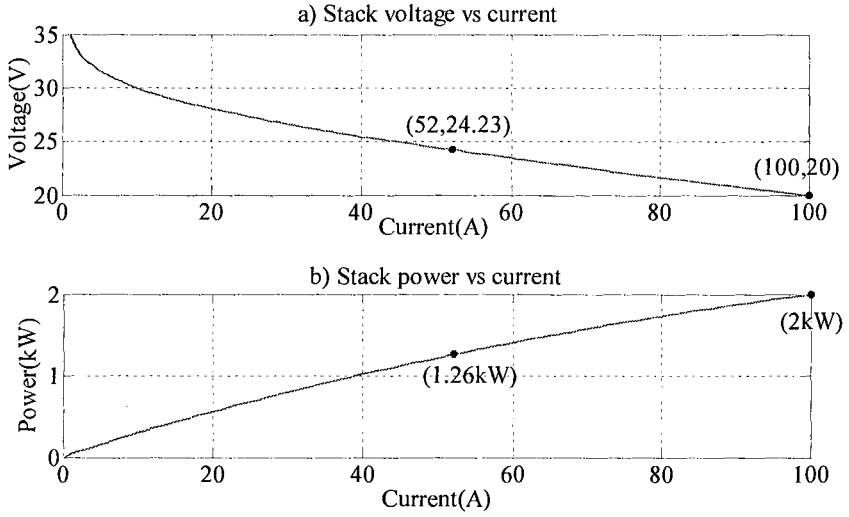

Fig. 3.22. The *V-I* and *power–current* characteristics of a PEM fuel cell.

In order to design a fuel cell control strategy, hydrogen flow has to be regulated to achieve the output power based on (3.15) - (3.34). Moreover, as fuel cell voltage varies according to the operating point as shown in Fig. 6, a controlled boost converter is used to interface the fuel cell with the system's dc link.. The fuel cell controller is shown in Fig. 3.23.

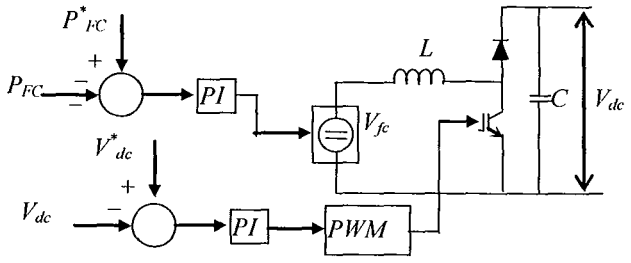

Fig. 3.23. PEM fuel cell controller.

3.3.2 Simulation of Fuel Cell Controller

The fuel cell controller performance is simulated in a MATLAB environment and results are presented. The fuel cell parameters are shown in Table 3.2.

Table 3.2. Parameters of fuel cell and controller

Type of fuel cell	PEM
Nominal voltage (volt)	24.23
Nominal current (Amp)	52
Number of cells	42
Operating temperature (Oc)	55
Rated power (KW)	1.26
Dc-link voltage	700
Switching frequency (k Hz)	20

In the simulation study, a fuel cell is connected to a variable load. The load profile is shown in Fig. 3.24, showing the fuel cell is connected to 0.6 kW of load. At a time of 10 seconds, the load is increased from 0.6 kW to 0.9 kW, and at 15 seconds, it is increased again from 0.9 kW to 1.1 kW. The fuel cell response is shown in Fig. 3.25.

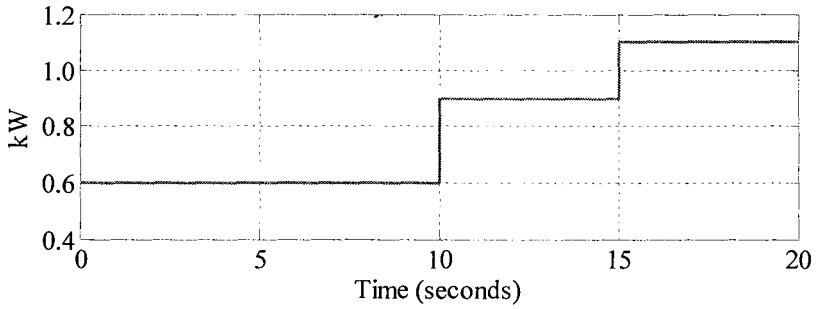

Fig. 3.24. Load profile.

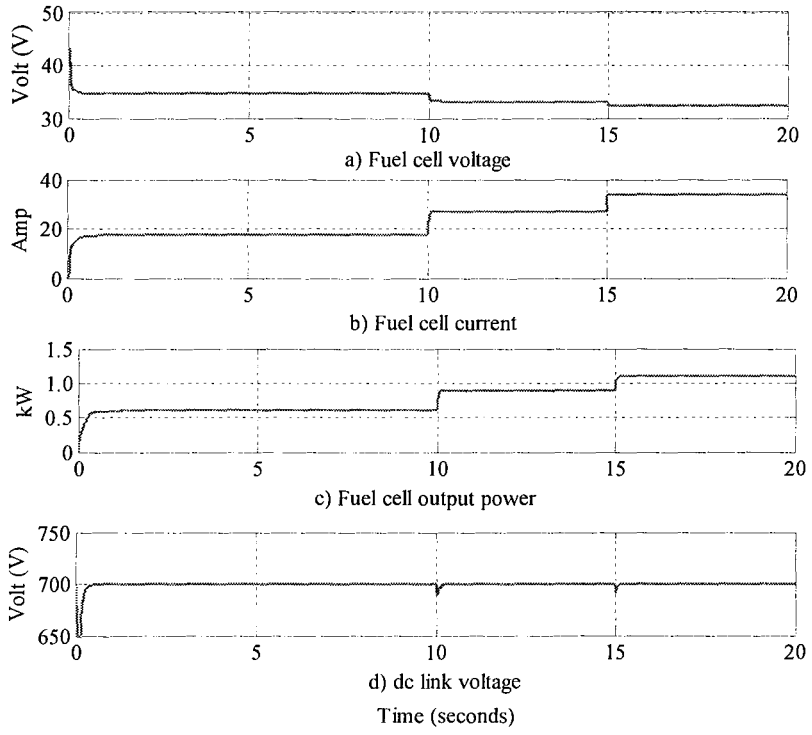

Fig. 3.25. Fuel cell response due to load changes.

3.3.3 Electrolyzer Modelling and Control

Electrolyzers decompose water into hydrogen and oxygen by passing a dc current between two electrodes, separated by aqueous electrolyte with good ionic conductivity [162] – [170]. The reaction for splitting water is as follows [162], [163]:

$$H_2O + electrical\ energy = H_2(g) + \frac{1}{2}O_2(g) \tag{3.35}$$

A minimum electric voltage has to be applied for this reaction to occur. The minimum electric voltage is also known as 'reversible voltage' which can be determined by Gibbs energy for water splitting. In an alkaline electrolyzer, the electrolyte is usually aqueous potassium hydroxide (KOH), where the potassium ion K^+ and hydroxide ion OH- facilitate the ionic transport. The anodic and cathodic reactions occur as follows:

Anode: $2OH^-(aq) \rightarrow \frac{1}{2}O_2(g) + H_2O(l) + 2e^-$

Cathode: $2H_{2O} + 2e^- \rightarrow H_2(g) + 2OH^-(aq)$

The electrolyzer modelling has three parts – electrochemical, electrical and thermal and hydraulic part. In this model, the thermal modelling is excluded and constant temperature mode is adopted, assuming the large time constant of the thermal model as proposed in [162], [163].

The electrode kinetic of an electrolyzer cell can be modelled using an empirical current-voltage (*I-U*) relationships as follows [162], [163]:

$$U = U_{rev} + \frac{r}{A}I + slog\left(\frac{t}{A}I + 1\right) \tag{3.36}$$

Fig. 3.26 shows the cell voltage vs the current density at different operating temperatures. It is noted that the difference between the two *I-U* curves is mainly due to the temperature dependence of the over-voltages.

Eq. (3.35) can be depicted as a more detailed *I-U* model, which takes into account the temperature dependence of the ohmic resistance parameter (r) and the over-voltage co-efficients s and t. A temperature dependent *I-U* model has been adopted from (3.36) as follows:

$$U = U_{rev} + \frac{r_2 + r_1 T}{A}I + slog\left(\frac{t_2 + \frac{t_1}{T} + \frac{t_0}{T^2}}{A}I + 1\right) \tag{3.37}$$

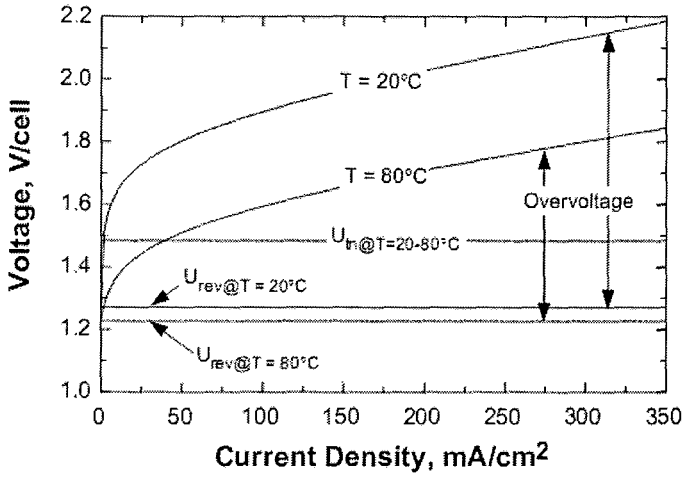

Fig. 3.26. *I-U* characteristics of an electrolyzer cell at high and low temperature.

The Faraday efficiency is defined as the ratio between the actual and theoretical maximum amount of hydrogen produced in the electrolyzer as follows [162], [163]:

$$\eta = \frac{f_{elz}^2}{f_2 + f_{elz}^2} f_2 \tag{3.38}$$

where $f_1 = 50 + 2.5T_{elz}$ and $f_2 = 1 - 0.00075T_{elz}$

According to Faraday's law, the production rate of hydrogen in an electrolyzer cell is directly proportional to the transfer rate of electrons at the electrodes, which is equivalent to the external electric current. Hence, the hydrogen production rate in an electrolyzer can be as follows [162], [163]:

$$M_{H2,pro} = \eta\,(T_{elz}, J_{elz}) \frac{N_{elz}}{2F} I \tag{3.39}$$

In normal operation, the hydrogen outlet rate should equal the hydrogen production rate, allowing the pressure and stored hydrogen quantity in the cathode to remain constant. Based on the ideal gas law, the resultant hydrogen pressure of hydrogen can be written as [162], [163]:

$$\frac{\vartheta_{elz}}{RT}\frac{dp_{H2,elz}}{dt} = M_{H2,pro} - M_{H2,out} \tag{3.40}$$

where ϑ_{elz} is the cathode volume , $p_{H2,elz}$ is the partial pressure of hydrogen in cathode, and $M_{H2,out}$ is the molar hydrogen outflow rate.

In order to control the power flow of the electrolyzer, the input current has to be controlled. A buck converter is used to regulate the power flow of the electrolyzer by regulating its current based on (3.36) – (3.40) as shown in Fig. 3.27.

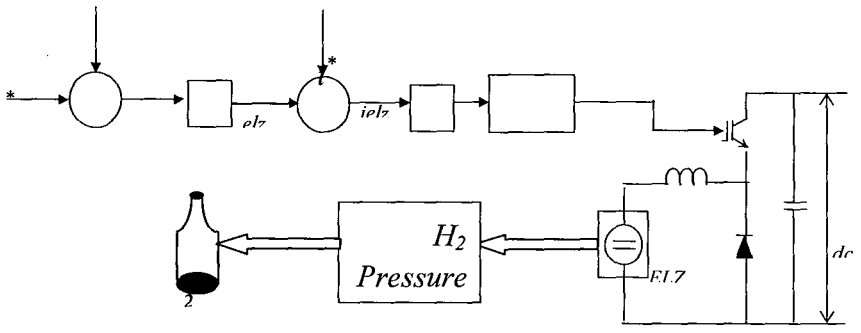

Fig. 3.27. The electrolyzer controller.

3.3.4 Simulation of Electrolyzer Controller

The battery controller system performance is simulated in a MATLAB environment and results are presented. In the simulation study, an electrolyzer is connected to a synchronous generator and variable load, as shown in Fig. 3.28.

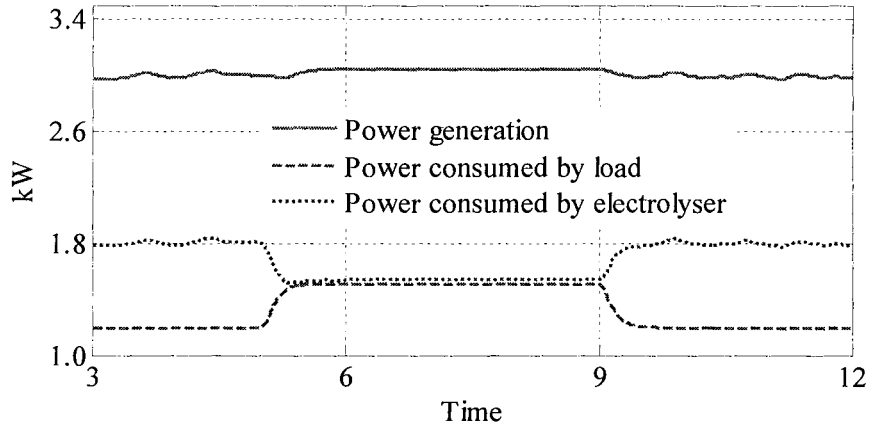

Fig. 3.28. The electrolyzer load consumption.

3.3.5 Compressor and Tank Model

The relationship between the molar flow rate $(M_{H2,pro})$ from the electrolyzer and compressor power (Pcomp) is given below, according to the polytrophic model [163]:

$$M_{H2,pro} = \frac{\alpha_{comp}}{w} P_{comp} \tag{3.41}$$

where $w = \frac{kRT_{ele}}{k-1}\left[\left(\frac{p_{tank}}{p_{ele}}\right)^{\frac{k-1}{k}} - 1\right]$

where α_{comp} is the compression efficiency and w is the polytropic work. k is the polytrophic coefficient and $p_{tank}$is the storage tank pressure.

Hydrogen storage $M_{H2,storage}$ is the difference between the hydrogen produced by the electrolyzer $M_{H2,pro}$and hydrogen used by the fuel cell $M_{H2,FC}$ as:

$$M_{H2,storage} = M_{H2,pro} - M_{H2,FC} \tag{3.42}$$

The pressure of stored hydrogen (p_{H2}) in the hydrogen tank can be derived as:

$$\frac{d}{dt}(p_{H2}) = \frac{RT_{Tank}}{\theta_{Tank}} M_{H2,storage} \tag{3.43}$$

where θ_{Tank} is the hydrogen storage tank volume and T_{Tank} is the tank temperature.

3.4 Inverter Control

The inverter is used in the proposed system to regulate the system's output voltage and frequency. The inverter's circuit diagram is shown in Fig. 3.30.

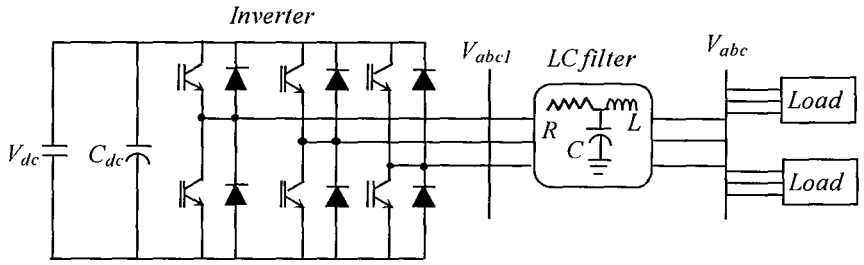

Fig. 3.30. Load side inverter.

From Fig. 3.30, the voltage relationship of the output and load sides of the inverter can be as follows:

$$\begin{bmatrix} V_{a1} \\ V_{b1} \\ V_{c1} \end{bmatrix} = R \begin{bmatrix} I_a \\ I_b \\ I_c \end{bmatrix} + L \frac{d}{dt} \begin{bmatrix} I_a \\ I_b \\ I_c \end{bmatrix} + \begin{bmatrix} V_a \\ V_b \\ V_c \end{bmatrix} \tag{3.44}$$

Eq. (3.44) can be expressed in *d-q* reference form as follows:

$$\begin{cases} V_d = V_{d1} - RI_d - L\frac{dI_d}{dt} + \omega LI_q \\ V_q = V_{q1} - RI_q - L\frac{dI_q}{dt} - \omega LI_d \end{cases} \tag{3.45}$$

The three powers can be expressed as:

$$P = V_a I_a + V_b I_b + V_c I_c \tag{3.46}$$

The expression of power in *d-q* axes can be:

$$S = P + jQ \tag{3.47}$$

$$\text{where} \begin{cases} P = \frac{3}{2}(V_d I_d + V_q I_q) \\ Q = \frac{3}{2}(V_d I_q + V_q I_d) \end{cases} \tag{3.48}$$

From (3.47), if the reference frame is as $V_d = |V|$ and $V_q = 0$, the active and reactive power can be expressed as:

$$\begin{cases} P = \frac{3}{2} V_d I_d = \frac{3}{2} |V| I_d \\ Q = \frac{3}{2} V_d I_q = \frac{3}{2} |V| I_q \end{cases} \tag{3.49}$$

From (3.48), regulating the active and reactive power can occur by controlling the direct and quadrature voltage components. The inverter controller measures the *d-* and *q-* components of output voltage. These are compared with the reference values ($V_d = |V|$ and $V_q = 0$). Based on the error, two PI controllers generate the appropriate control signal for the inverter, shown in Fig. 3.31.

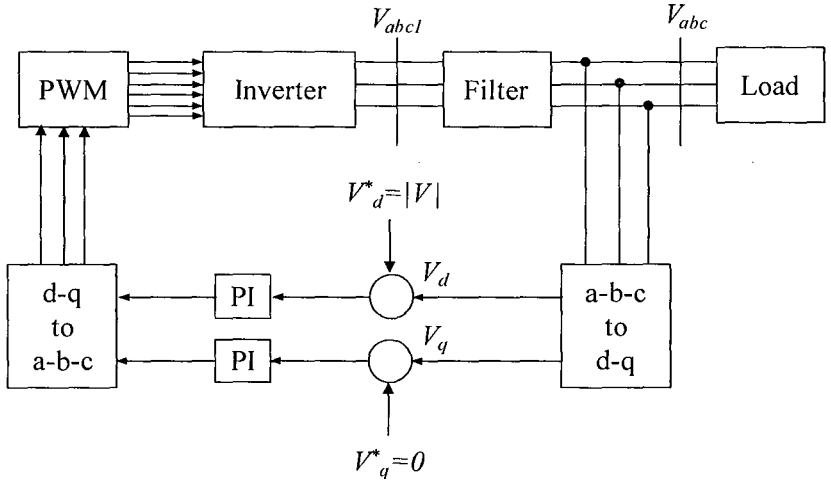

Fig. 3.31. Block diagram of inverter controller.

3.4.1 Simulation of Load Side Inverter

The load side inverter system performance is simulated in a MATLAB environment and results are presented. In the simulation study, constant power is supplied by a dc source.

Fig. 3.32 depicts the a) voltage, b) frequency and c) current response of the inverter. It is seen that the inverter controller can maintain constant voltage and frequency despite load changes. From Fig. 3.33, it is seen that the inverter controller controls the *d*- and *q*- axes component of output voltage to obtain a constant voltage. The real and reactive inverter power output is shown in Fig. 3.34. The instantaneous voltage and current of each phase due to load disturbance is shown in Fig. 3.35. Here, it is evident that the inverter controls the sinusoidal voltage and current web during load changes.

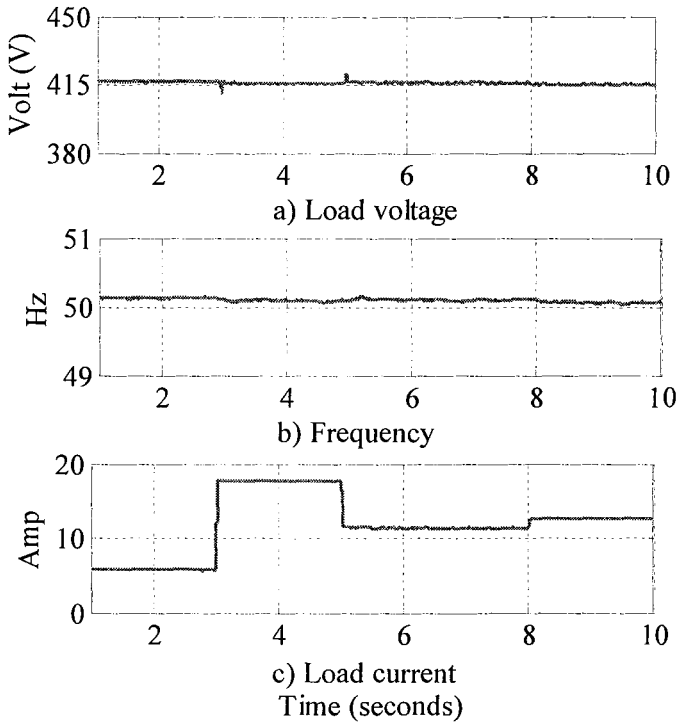

Fig. 3.32. Inverter response a) voltage b) frequency and c) current.

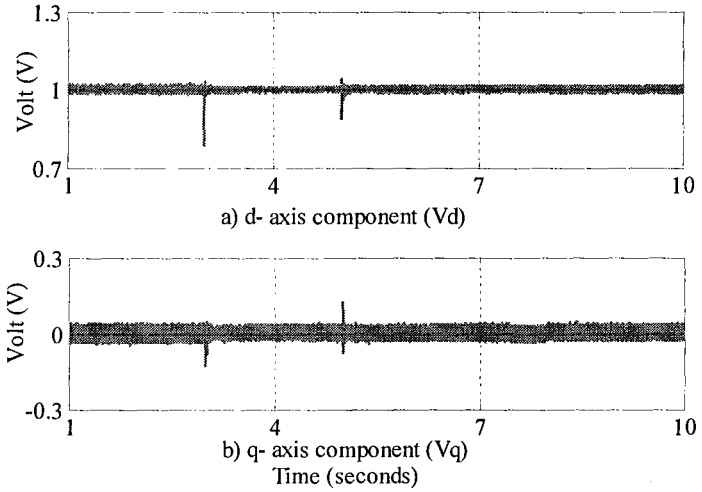

Fig. 3.33. Inverter voltage a) *d*-axis and b) *q*-axis component.

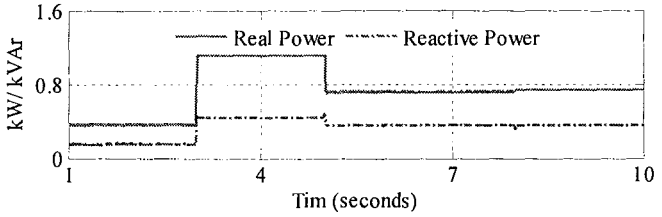

Fig. 3.34 Inverter output power.

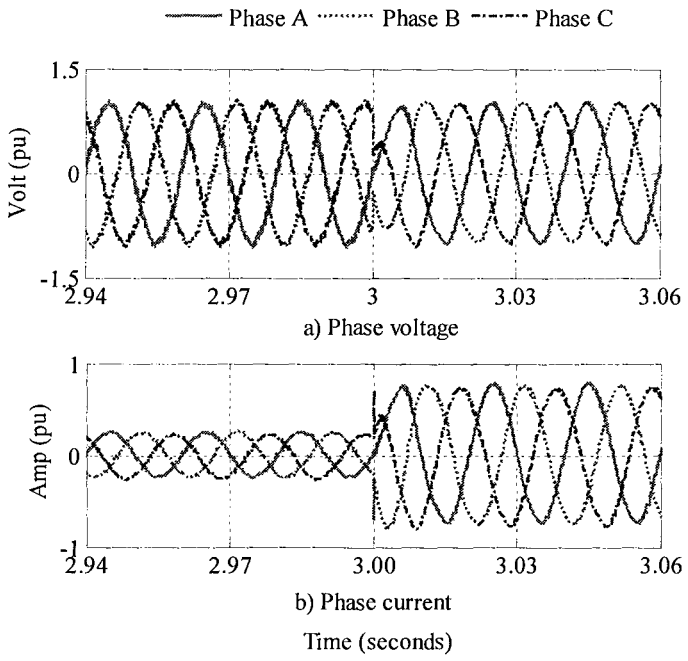

Fig. 3.35. Inverter response at time of 3:00 second a) voltage and b) frequency.

Conclusion

This chapter outlines the modelling and control aspects of the energy storage and inverter of the proposed hybrid power system. The modelling and the control strategies of the energy storage systems are conducted in a MATLAB/Simulink environment. The energy storage system is comprised of battery and hydrogen storage systems. The battery storage system is controlled by a bi-directional dc-dc converter. From the simulation study, it can be seen that this converter controls the charging and discharging of the battery storage system. The hydrogen storage system consists of an electrolyzer, fuel cell and hydrogen storage system. The electrolyzer and fuel cell are controlled by the buck and boost converters, respectively. From the simulation studies, it is also seen that these converters can control the power flow of the electrolyzer and fuel cell units.

Chapter 4

Diesel Generator Modelling and Control

This chapter focuses on the modelling and simulation of a diesel generator used in the hybrid power supply system as a stand-by generator. A mathematical model of the diesel generator and a 'black-box' model of the diesel-hydrogen generator will be presented. A power sharing algorithm of the diesel generator with other generation sources will also be discussed.

4.1 Mathematical Model of Diesel Generator

A diesel generator is the combination of a diesel engine with an electrical generator or alternator. A diesel engine uses compression ignition to burn the fuel, which is injected into the combustion chamber during the final compression stage.. The fuel injection is controlled by a set of devices called the governor, which effectively controls the frequency and real power flow of the system. An alternator is a generator producing electrical power from mechanical torque obtained from the diesel engine. The alternator controls the output voltage and reactive power flow to the system.

4.1.1 Diesel Engine and Governor System Model

The efficiency of the combustion process is the ratio of the effective power developed by the engine and the available power on the crank shaft simultaneously during the combustion chamber, shown in the following equation [166], [167], [171]-[173]:

$$\varepsilon = \frac{zW_i v}{\dot{m}_B H_u} \tag{4.1}$$

where ε is the combustion efficiency, z is the number of cylinders in the diesel engine, W_i is the diesel engine mean effective work, v is the stroke cycle per second, $\dot{m}_B$ is the diesel engine combusted fuel rate (kg/sec), H_u is the heat value of the fuel (kJ/kg).

After combustion, the engine's effective mean pressure (p_i) is developed, defined in the following [166] - [168]:

$$p_i = \frac{W_i}{V_h} \tag{4.2}$$

where V_h is diesel engine stroke volume (m^3),

By solving Eqs. (4.1) and (4.2), the effective mean pressure (p_i) is as follows:

$$p_i = \frac{\dot{m}_B H_u}{z V_h v} = C_1 \dot{m}_B \varepsilon \tag{4.3}$$

where C_1 is the proportionality constant. For normal or stable operation of the power system, the value of v is imposed to maintain system frequency constant at 50 Hz.

The mean pressure of mechanical losses (p_f) is assumed to be proportional to the mean mechanical speed/ system frequency follows:

$$p_f = C_3 \omega \tag{4.4}$$

The mean real pressure (p_k) is the difference between the effective mean pressure (p_i) and mean pressure of mechanical losses (p_f), shown as follows:

$$p_k = p_i - p_f \tag{4.5}$$

The real mechanical power of the diesel engine depends on the real mean power as follows:

$$P_{Dm} = zV_h v p_k = zV_h \frac{\omega_m}{\pi k} p_k \tag{4.6}$$

In a diesel generator shown in Fig. 4.1, per unit mechanical torque (T_{Dm}) generated by the engine is shown as:

$$T_{Dm} = \frac{P_{Dm}}{\omega_m T_b} = \frac{V_H}{\pi k T_b} p_k = C_2 p_k \tag{4.7}$$

where T_b is the base torque, V_H is the diesel total stroke volume (m^3), k is the number of stroke of diesel engine, and $C_2 = \frac{V_H}{\pi k T_b}$.

The differential equations depicting the diesel engine and speed regulation are shown below [167]:

$$\frac{dP_C}{dt} = -\frac{K_I}{\omega_O} \Delta\omega \tag{4.8}$$

$$\frac{d\dot{m}_B}{dt} = \frac{1}{\tau_2}\left(K_2 P_C - \frac{K_2}{\omega_O R} \Delta\omega - \dot{m}_B \right) \tag{4.9}$$

$$\dot{m}_B(t) = \dot{m}_B(t - \tau_1) \tag{4.10}$$

where $\dot{m}_B$ is the diesel engine fuel consumption rate (kg/sec), K_I is the governor summing-loop amplification factor and R is the diesel engine permanent speed droop.

The electrical rotor angle (δ) is related to the electrical angular velocity:

$$\frac{d\delta}{dt} = \omega - \omega_O = \Delta\omega \tag{4.11}$$

The mechanical motion equation is determined as [2]:

$$\frac{d\omega}{dt} = \frac{\omega_O}{2H}\left(T_{Dm} - T_{De} - \frac{D}{\omega_O}\Delta\omega\right) \tag{4.12}$$

where D is the load damping coefficient and $D = \frac{\partial P_L}{\partial f}$ and H is the generator's inertia constant. A schematic diagram of a diesel engine with governor system is shown in Fig. 4.1.

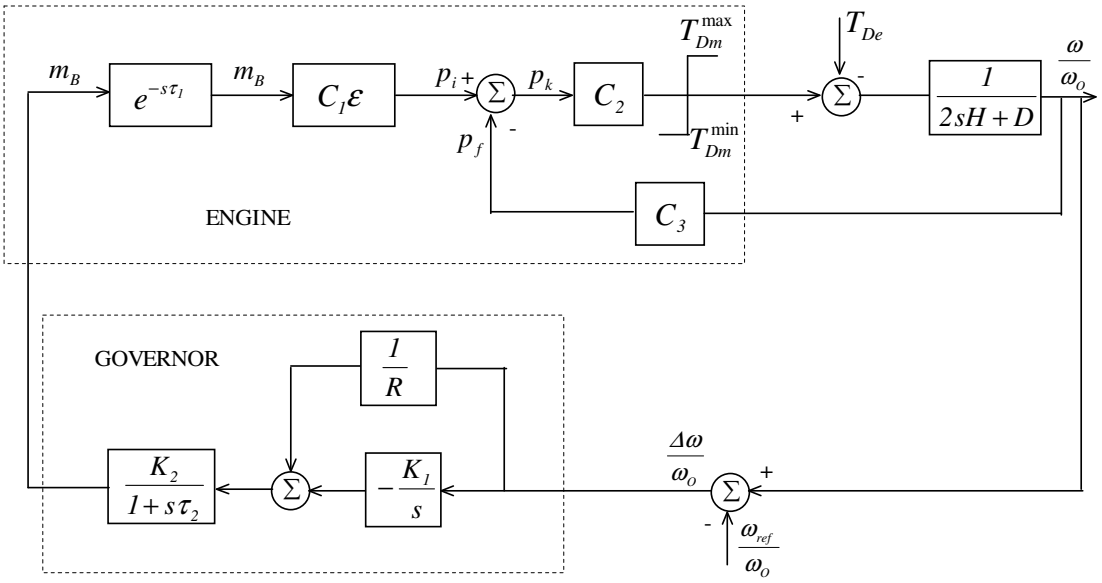

Fig. 4.1. Block diagram of diesel engine and governor system.

4.1.2 Excitation System Model

The main function of an excitation system is to supply direct current to the field winding of a synchronous generator. The excitation system also performs the power

system's essential control and protective functions by regulating the field voltage and current. The exciter's control functions include voltage and reactive power flow control to enhance a system's stability. The exciter's protective functions ensure that the required voltage and reactive power flow do not exceed the capability limits of the synchronous machine, excitation system and other equipment [169].

The performance requirements of an excitation system are mainly determined by the status of the synchronous generator and power system. The excitation system is required to supply and adjust the synchronous generator's field current to maintain a voltage within the continuous capability limit. From the power system point of view, the excitation system should contribute to the effective control of system voltage and enhance stability. It should also respond rapidly to any disturbance and minimize transient instability [170].

Elements of an excitation system

The excitation system consists of an exciter, regulator, terminal voltage transducer and load compensator, power system stabilizer and limiters and protective circuits as shown in Fig. 4.2. A brief description of these components follows [169]:

1. **Exciter.** The exciter provides dc power to the synchronous machine field winding.
2. **Regulator.** The regulator processes and amplifies the input control signals to a desired level and generates appropriate control signals for the exciter.
3. **Terminal voltage transducer and load compensator.** A terminal voltage transducer senses terminal voltage, rectifies and filters it to a dc quantity and compares it with the reference voltage. Moreover, it provides load compensation such as line drop or reactive compensation. It is also capable of holding constant voltage at a point electrically remote from the generator terminal.
4. **Power system stabilizer.** The power system stabilizer provides an input signal (based on rotor speed variation, accelerating power, and frequency deviation) to the regulator, to encounter the damp power system oscillation.

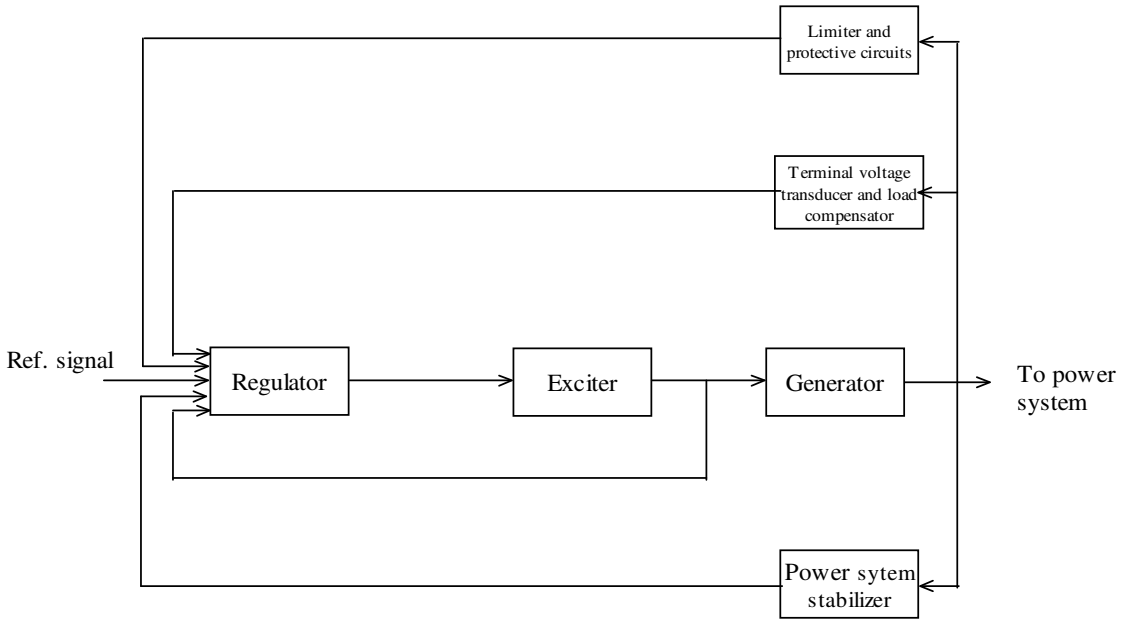

Fig. 4.2. Block diagram of an exciter system.

5. Limiter and protective circuits. This system provides proper control and protective functions to ensure that capability limits of the exciter and synchronous generator are not exceeded.

Types of excitation systems

Excitation systems can be divided into three main categories [170]:

- DC excitation system which utilizes direct current generation with a commutator as the system's source.
- AC excitation system which uses an alternator and either a stationary or rotating rectifier to produce a direct current to the field winding of a synchronous generator.
- Static excitation system which utilizes a transformer or auxiliary generator windings and rectifiers as a power source.

The basic elements of the different types of excitation systems are self or separately-excited dc exciters, ac exciters, controlled or non-controlled rectifiers,

magnetic or rotating or electronic amplifiers, excitation system stabilizer feedback circuits and signal sensing and processing circuits. Detailed modelling of these elements is discussed below.

Separately-excited dc exciter

The circuit for a separately-excited dc exciter is shown as in Fig. 4.3. [169].

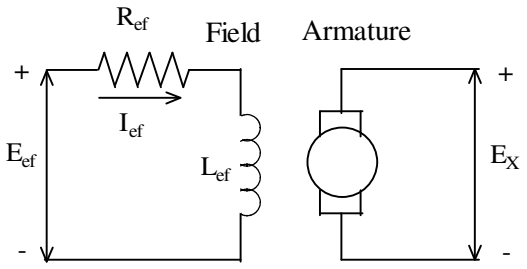

Fig. 4.3. Separately- excited dc exciter.

From Fig. 4.3 the exciter field circuit can be described as follows [169]:

$$E_{ef} = R_{ef} I_{ef} + \frac{d\psi}{dt} \tag{4.13}$$

where E_{ef} is the input field voltage, R_{ef} is the field resistance, I_{ef} is the field current, and ψ is the flux linkage of the field winding.

Neglecting the field leakage flux, the exciter output voltage E_X can be written as

$$\begin{cases} E_X = K_X \psi \\ or \quad \psi = \dfrac{E_X}{K_X} \end{cases} \tag{4.14}$$

where K_X is a constant that depends on the speed and winding configuration of the exciter armature.

The output voltage of an exciter is a non-linear function of the exciter current, owing to the magnetic saturation. This effect is shown in Fig. 4.4.

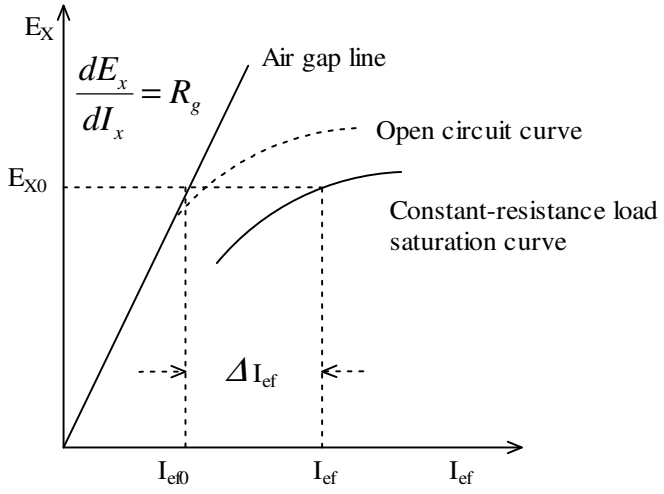

Fig. 4.4. Exciter load saturation curve.

In Fig. 4.4, R_g is the slope of the air gap line, I_{ef} is the current needed for the required output of the exciter under a constant loading condition. From Fig. 4.3, it is seen that:

$$I_{ef} = I_{ef\,0} + \Delta I_{ef} \tag{4.15}$$

where ΔI_{ef} is a non-linear function of E_X and can be expressed as follows:

$$\Delta I_{ef} = E_X S_e(E_X) \tag{4.16}$$

where $S_e(E_X)$ is a non-linear saturation function which depends on E_X.

Substituting the value ΔI_{ef} (4.16) and ψ (4.14) to (4.13), the following can be obtained:

$$E_{ef} = R_{ef} I_{ef} + \frac{d\psi}{dt}\frac{R_{ef}}{R_g} = E_X + R_{ef} S_e(E_X) E_X + \frac{1}{K_X}\frac{dE_X}{dt} \tag{4.17}$$

The per unit values of Eq. (4.17) can be obtained by considering the rated output voltage of the exciter (E_{Xbase}) as base voltage, and rated exciter current (I_{efbase}) as base current:

- Base voltage: E_{Xbase}
- Base current: $I_{efbase} = \dfrac{E_{Xbase}}{R_{gbase}}$

The per unit expression of Eq. (4.17) is obtained as follows:

$$\begin{cases} \dfrac{E_{ef}}{E_{Xbase}} = \dfrac{R_{ef}}{R_g}\dfrac{E_X}{E_{X\,base}} + R_{ef}\,Se(E_X)\dfrac{E_X}{E_{X\,base}} + \dfrac{1}{K_X}\dfrac{d}{dt}\left(\dfrac{E_X}{E_{X\,base}}\right) \\ \quad or \quad \dddot{E}_{ef} = \dfrac{R_{ef}}{R_g}\dddot{E}_X\left(1+\dddot{S}_e\left(\dddot{E}_X\right)\right) + \dfrac{1}{K_X}\dfrac{d\dddot{E}_X}{dt} \end{cases} \tag{4.18}$$

In (4.18), $\dddot{S}_e\left(\dddot{E}_X\right)$ can be defined as:

$$\dddot{S}_e\left(\dddot{E}_X\right) = \frac{\Delta\dddot{I}_{ef}}{\dddot{E}_X} = R_g S_e(E_X)$$

The parameter K_X can be defined as:

$$K_X = \frac{E_X}{\psi} = \frac{E_X}{L_{ef} I_{ef}} = \frac{R_g \dddot{E}_X}{L_{ef}\dddot{I}_{ef}}$$

Now let us consider

$$K_X = \frac{E_X}{\psi} = \frac{E_X}{L_{ef} I_{ef}} = \frac{R_g \ddot{E}_X}{L_{ef}\ddot{I}_{ef}} = \frac{1}{T_E};$$

$\dfrac{R_{ef}}{R_g} = K_E$; and $\dddot{S}_e\left(\dddot{E}_X\right)\dfrac{R_{ef}}{R_g} = S_e\left(\dddot{E}_X\right)$

By substituting the values of K_X, $\frac{R_{ef}}{R_g}$, and $\dddot{S}_e\left(\dddot{E}_X\right)\frac{R_{ef}}{R_g}$, Eq. (4.18) can be written as:

$$\dddot{E}_{ef} = K_E\dddot{E}_X + \dddot{E}_X S_e\left(\dddot{E}_X\right) + T_E\frac{d\dddot{E}_X}{dt} \tag{4.19}$$

Applying a Laplace transformation in (4.19),

$$\dddot{E}_{ef} = K_E\dddot{E}_X + \dddot{E}_X S_e\left(\dddot{E}_X\right) + T_E S\dddot{E}_X \tag{4.20}$$

Eq. (4.20) represents the mathematical model of a separately-excited excitation system, shown as a block diagram in Fig. 4.5:

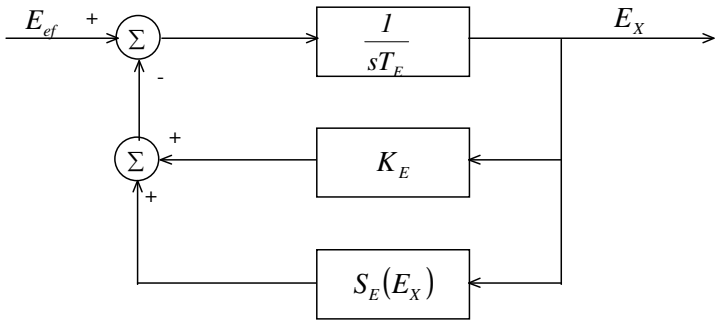

Fig. 4.5. Block diagram of separately-excited dc exciter.

Self-excited dc exciter

The circuit of a self-excited dc exciter is shown in Fig. 4.6 [169].

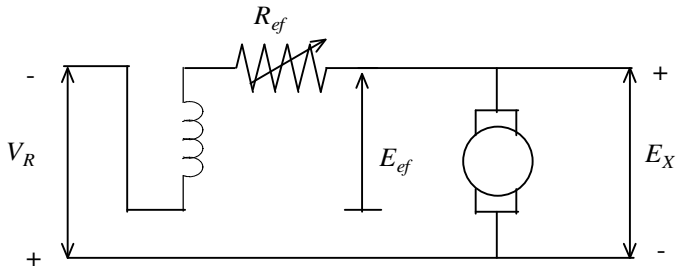

Fig. 4.6. Self-excited dc exciter.

From Fig. 4.6, it is seen that

$$E_{ef} = V_R + E_X$$

The relationship between E_{ef} and E_X can be developed as in the case of a separately-excited machine. Substituting the value of E_{ef} in Eq. (4.20), we have

$$\begin{cases} \ddot{E}_X + \ddot{V}_R = \ddot{E}_X\left(K_E + S_e\left(\ddot{E}_X\right)\right) + T_E S\ddot{E}_X \\ or \quad \ddot{V}_R = K'_E\ddot{E}_X + \ddot{E}_X S_e\left(\ddot{E}_X\right) + T_E S\ddot{E}_X \end{cases} \tag{4.21}$$

where $K'_E = \dfrac{R_{ef}}{R_g}$

Eq. (4.21) represents the mathematical model of a self-excited excitation system, in block diagram form in Fig. 4.7.

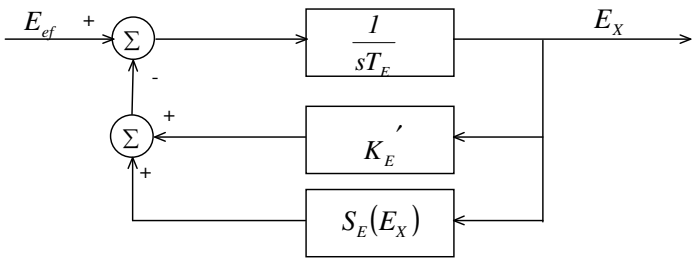

Fig. 4.7. Block diagram of self-excited dc exciter.

AC exciter and rectification system

The general structure of the ac exciter model is similar to that of the dc exciter. However, for an ac system, armature reaction affects the performance in load regulation. A block diagram of an ac exciter system is shown in Fig. 4.8. Generator field current (I_{FD}) represents the exciter load current and $K_D I_{FD}$ the armature reaction demagnetizing effect [169].

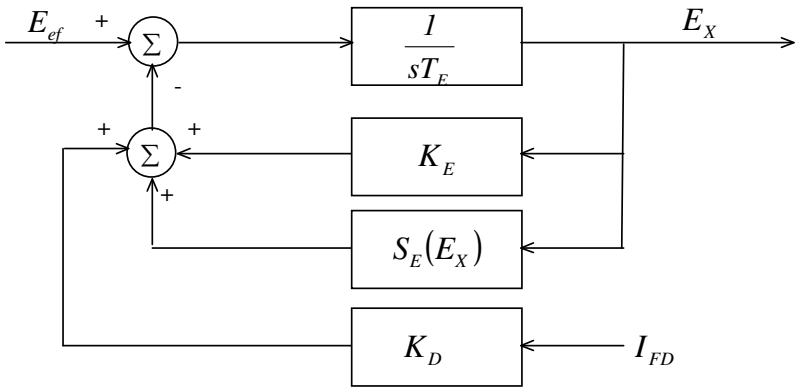

Fig. 4.8. Block diagram of ac excitation system.

A three-phase full wave diode rectifier is used to convert the ac to dc current. The diode rectifier operates in three different modes depending on commutating voltage drop as the rectifier current varies from no load to short circuit level. Eqs. (4.22) – (4.24) represent the rectifier regulation as a function of commutation voltage drop:

$$E_{FD} = F_{EX} V_E \tag{4.22}$$

$$F_{EX} = F(I_N) \tag{4.23}$$

$$I_N = \frac{K_C I_{FD}}{V_E} \tag{4.24}$$

In Eqs. (4.22) - (4.24), constant K_C depends on the commutating reactance. The expression for the function $f(I_N)$ characterizes the three different models of rectifier circuit operation shown below:

Model 1: $f(I_N) = 1 - 0.577 I_N \qquad if\ I_N \le 0.433$

Model 2: $f(I_N) = \sqrt{0.75 - I_N^{\,2}} \qquad if\ 0.433 < I_N \le 0.75$

Model 3: $f(I_N) = 1.732(1 - I_N) \qquad if\ 0.75 \le I_N \le 1$

The exciter output voltage (E_{FD}) is calculated as the product of ac exciter internal voltage (E_{FD}), accounting for the effects of armature reaction and rectifier regulation in the form of a block diagram shown in Fig. 4.9.

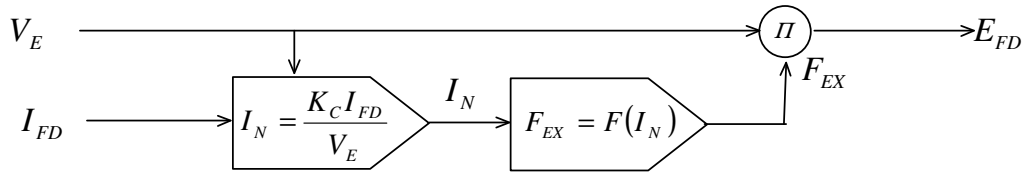

Fig. 4.9. Block diagram of a rectifier regulation model.

Excitation system stabilizer modelling

The excitation system stabilizer model is shown as in Fig. 4.10. The transformer equations in a Laplace domain are as follows:

$$\begin{cases} V_1 = R_1 i_1 + sL_1 i_1 + sMi_2 \\ V_2 = R_2 i_2 + sL_2 i_2 + sMi_1 \end{cases} \tag{4.25}$$

In Eq. (4.25), subscripts 1 and 2 denote the primary and secondary quantities; R, L and M denote the respective resistance, inductance and mutual inductance of the transformer.

As the secondary transformer is connected to the high impedance circuit, i_2 can be neglected to obtain the following expression:

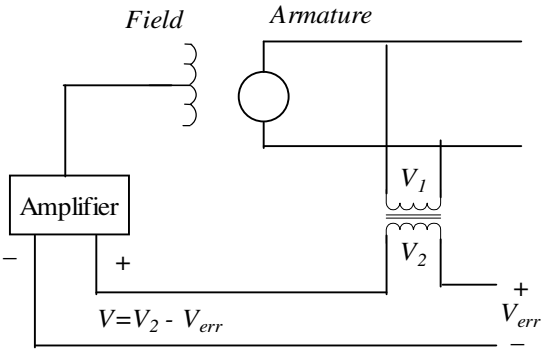

Fig. 4.10. Block diagram of excitation system stabilizer transformer.

$$V_1 = R_1 i_1 + sL_1 i_1 \tag{4.26}$$

$$V_2 = sMi_1 \tag{4.27}$$

Thus, $$\frac{V_2}{V_1} = \frac{sM}{R_1 + sL_1} = \frac{sK_F}{1 + sT_F} \tag{4.28}$$

where $K_F = \frac{M}{R}$ and $T_F = \frac{L_1}{R}$.

Terminal voltage transducer and load compensator modelling

Load compensation is used to maintain a constant voltage either within or external to the generator. A block diagram of a terminal voltage transducer and load compensator is shown in Fig. 4.11 [169].

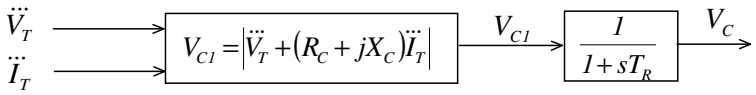

Fig. 4.11. Block diagram of terminal voltage transducer and load compensator.

The detailed modelling of an excitation system is shown in Fig. 4.12. [4].

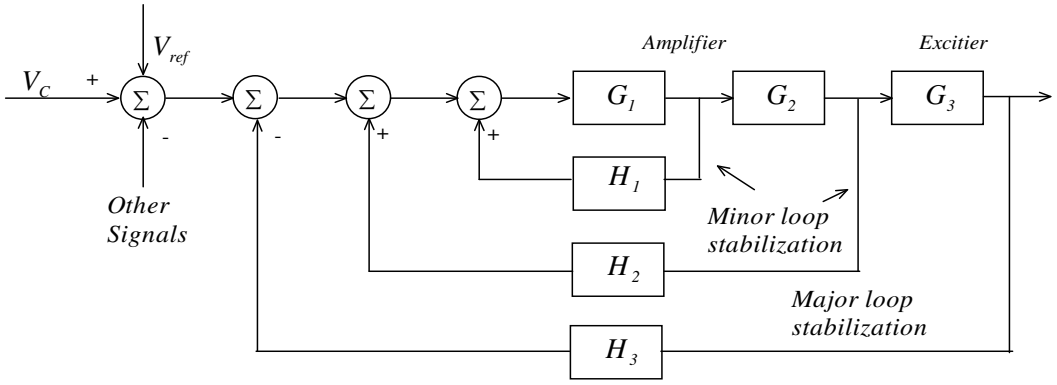

Fig. 4.12. Block diagram of detailed excitation model.

4.1.3 Performance of Diesel Generator Model

In this section, a diesel generator is implemented in a simple power system consisting of resistive and reactive loads. The diesel generator parameters and load profile are shown in Table 4.1.

Table 4.1. The parameters of diesel generator and load profile

Synchronous generator specification

Rated Power	325 kW
Rated Speed	1500 rpm
Rated Frequency	50 Hz
Rated Voltage	400 V
Stator Resistance	0.0183 ohm
Inertial Constant	0.1759
Pole pair	2

Load profile

Time	KW	KVAR
0	50	0
8 s	58	10
16 s	138	18
24 s	218	42
32 s	268	66

From Fig. 4.13 shows that the diesel generator can provide the necessary power while keeping the voltage and frequency constant. The voltage response of the diesel generator is shown during active and reactive power disturbance at a time of 16 seconds. From Fig. 4.14, it is seen that the diesel generator can provide a sinusoidal output voltage during the disturbance, at a time of 16 seconds.

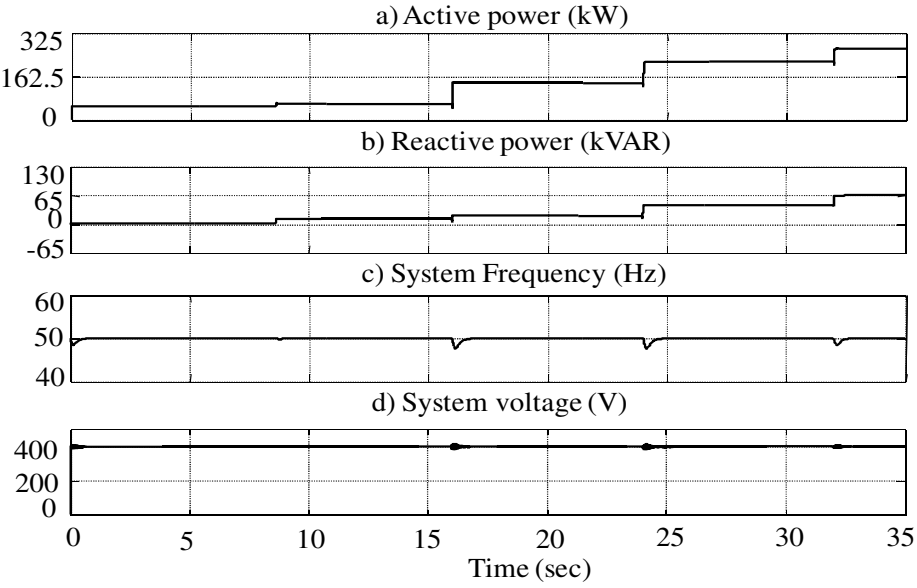

Fig. 4.13. Diesel generator response: a) active power, b) reactive power c) frequency d) voltage response.

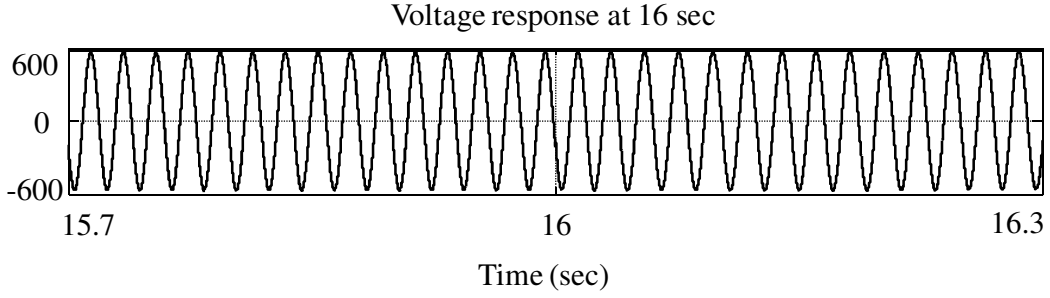

Fig. 4.14. Voltage response due to active and reactive power disturbance at a time of 16 seconds.

4.2 Modelling of Dual-Fuel Engine with Hydrogen

Diesel engine performance when operating on dual-fuel mode has been investigated in the hydrogen laboratory at the Centre for Renewable Energy and Power systems (CREPS) of the University of Tasmania. Preliminary research has been carried out by conducting an experiment on a diesel engine and electric generator assembly, working at a fixed speed of 1500 rpm.

4.2.1 Experimental Setup

The block diagram of the experimental setup used to examine the performance of a dual-fuel engine is shown in Fig. 4.15.

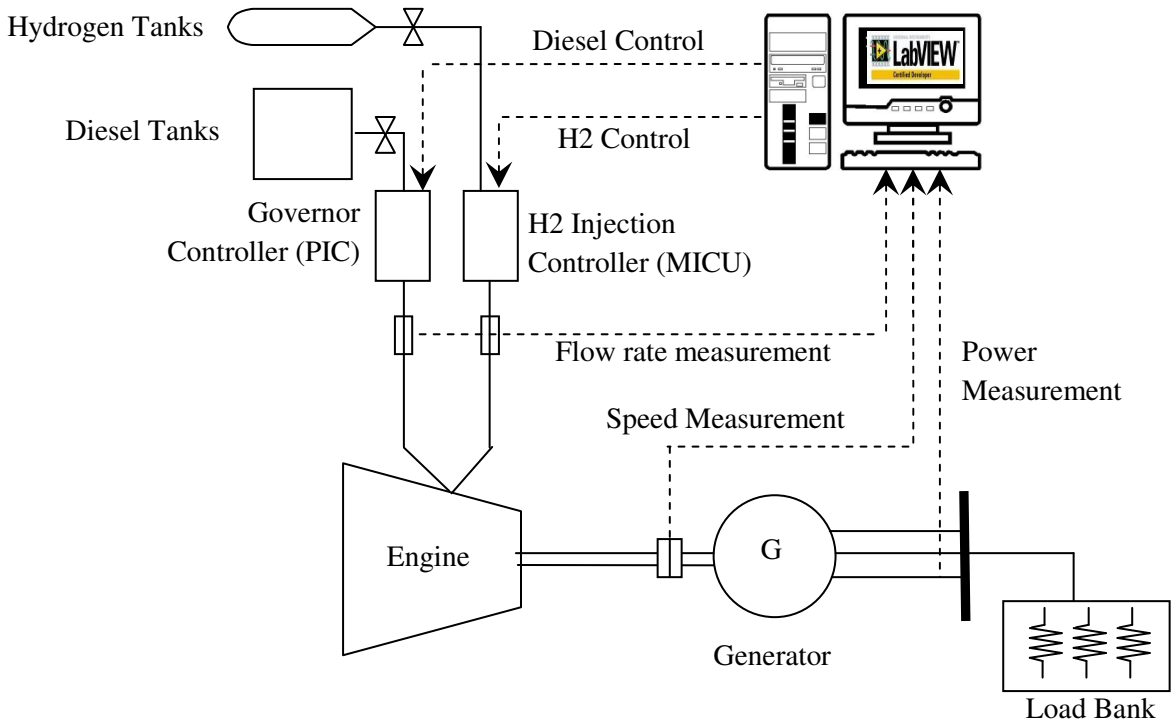

Fig. 4.15. Experimental setup for performance evaluation of the dual-fuel engine.

In this setup, the compression engine/generator dual-fuel supply system is investigated to evaluate the influence of a quantity of hydrogen injected into the consumed diesel fuel. Various electrical loads are applied to the alternator stimulating the engine governor response to the increase/decrease in fuel flow. Initially, the engine was started with diesel only with no load. The diesel flow rate was measured and recorded. Once the engine reached its steady state condition, a gradual load increase was applied to the engine. After reaching the steady state, a fixed ratio of hydrogen was injected and engine performance was recorded. Various measurement results are presented in Fig. 4.16. The engine speed and flow rates of the diesel and hydrogen are shown at different loading conditions. In this case, the hydrogen rate was fixed at 5 mg/s.

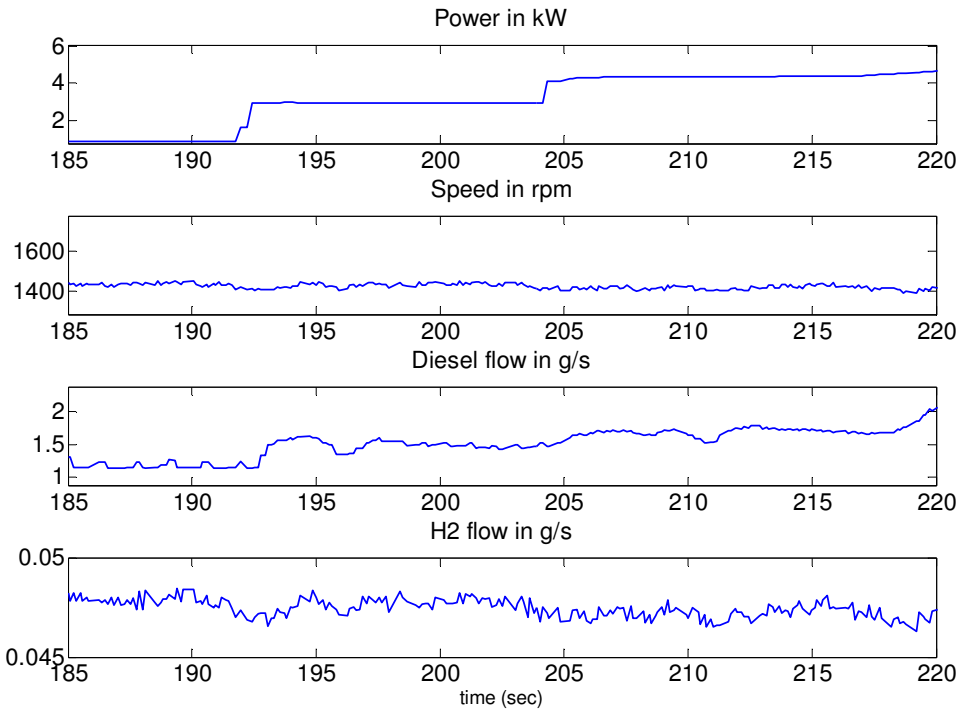

Fig. 4.16. Hydrogen performance at 5mg/s hydrogen injection

The compression engine is highly non-linear and its characteristics change with a change in speed, power developed, temperature, pressure and other conditions. An adaptive neuro-fuzzy inference system (ANFIS) has been used as a 'black-box' modelling tool for its ability to model non-linear dynamic systems [170]-[180].

4.2.2 Adaptive Neuro-Fuzzy Inference Systems

ANFIS works by constructing a fuzzy inference system from a given input-output data set. The parameters associated with the membership functions of the constructed fuzzy inference system are adjusted or tuned throughout the training process, using either a back-propagation algorithm or hybrid combination of both back-propagation and the least squares method. These methods allow the fuzzy inference system to learn from the input-output data set it is attempting to model. The architecture of a typical ANFIS is shown in Fig. 4.17 [180]. The interconnected network consists of the following layers [180], [181]:

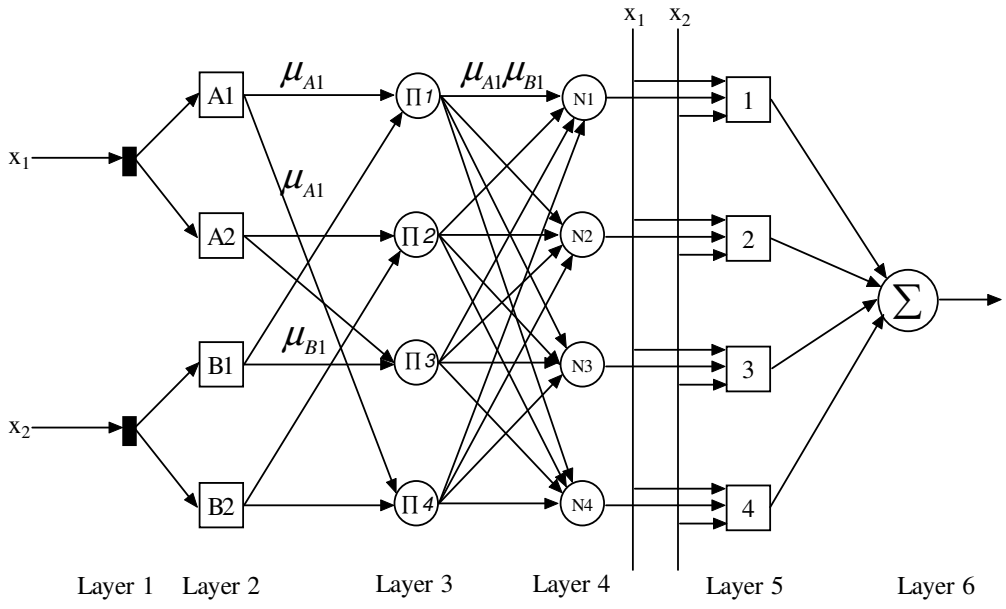

Fig. 4.17. Typical ANFIS architecture.

Layer 1. This is known as the input layer, where the inputs x1 and x2 are applied and passed without being processed to a number of neurons in Layer 2.

Layer 2. Known as fuzzification layer, neurons perform fuzzification in the incoming inputs x1 and x2. The output is as follows:

$$\begin{aligned} y_{Ai} &= \mu_{Ai} \\ y_{Bi} &= \mu_{Bi} \end{aligned} \tag{4.29}$$

Layer 3. This is known as the rule layer, at which each neuron evaluates a single Sugeno-type fuzzy rule. The rule neurons calculate the firing strength by determining the product of the incoming signals as shown below.

$$y_{\Pi i} = \prod_{j=1} x_{ji} \tag{4.30}$$

From Fig. 5.3, the output of the 1st neuron in Layer 3 is given below:

$$y_{\Pi 1} = \mu_{A1}\mu_{B1} \tag{4.31}$$

where μ_{A1} represents the firing strength of Rule 1.

Layer 4. This is called the normalization layer. Here, neurons receive inputs from all Layer 3 neurons. The normalized firing strength is calculated as the ratio of the firing strength of a given rule to the sum of firing strengths of all rules, as shown below:

$$y_{Nii} = \frac{\mu_i}{\sum_{j=1}^{n} \mu j} = \overline{\mu_i} \tag{4.32}$$

Here the output represents the contribution of a particular rule to the final result.

Layer 5. Known as the defuzzification layer, each neuron in this layer has the inputs of both the original input signals x1 and x2 and the output from Layer 4. Here, each neuron calculates the weighted consequent value of a particular rule as shown below:

$$y_i = \overline{\mu_i}\left(k_{i0} + k_{i1}x_1 + k_{i2}x_2\right) \tag{4.33}$$

where $\overline{\mu_i}$ is the input of defuzzification neuron i in Layer 5, y_i - is the output of defuzzification neuron i in Layer 5, k_{i0}, k_{i1} and k_{i2} is a set of consequent rule i parameters.

These consequent parameters are learnt by the ANFIS during the training process and used to tune the membership functions.

Layer 6. This is known as the summation neuron layer, consisting of one neuron which adds the outputs from Layer 5 together. The total sum of these inputs is the ANFIS output (y ANFIS) shown below:

$$y_{ANFIS} = \sum_{i=1}^{n} y_i \tag{4.34}$$

For each iteration of the training algorithm in ANFIS there is a forward and backward pass. In the forward pass, the inputs are applied to the ANFIS. Neuron outputs are calculated layer-by-layer and rule consequent parameters defined. Once the forward pass has been completed and the error determined, the second part of the iteration is implemented. Here, the back-propagation algorithm is applied, and the error propagated back through the network. The antecedent parameters are updated according to the chain rule. Using membership parameters and a training set of Z input-output data pairs, we are able to construct Z linear equations in terms of the consequent parameters as shown in Eq. (4.35).

$$\begin{aligned}
y_d(1) &= \overline{\mu_1}(1)f_1(1)+\overline{\mu_2}(1)f_2(1)+\ldots+\overline{\mu_n}(1)f_n(1)\\
y_d(2) &= \overline{\mu_1}(2)f_1(2)+\overline{\mu_2}(2)f_2(2)+\ldots+\overline{\mu_n}(2)f_n(2)\\
&\vdots \qquad\qquad \vdots \qquad\qquad \vdots\\
&\vdots \qquad\qquad \vdots \qquad\qquad \vdots\\
y_d(Z) &= \overline{\mu_1}(Z)f_1(Z)+\overline{\mu_2}(Z)f_2(Z)+\ldots+\overline{\mu_n}(Z)f_n(Z)
\end{aligned} \tag{4.35}$$

where y_d is a $Z\times 1$ desired output vector.

as $f_1(i)=k_{10}+k_{11}x_1(i)+k_{12}x_2(i)+k_{13}x_3(i)\cdots+k_{1m}x_m(i)$, substituting the value of $f_1(i)$ into (4.36),

$$\begin{aligned}
y_d(1) &= \overline{\mu_1}(1)(k_{10}+k_{11}x_1(1)+k_{12}x_2(1)+k_{13}x_3(1)\cdots+k_{1m}x_m(1))\\
&\quad+\overline{\mu_2}(1)(k_{20}+k_{21}x_1(1)+k_{22}x_2(1)+k_{23}x_3(1)\cdots+k_{2m}x_m(1))+\ldots\\
&\quad+\overline{\mu_n}(1)(k_{n0}+k_{n1}x_1(1)+k_{n2}x_2(1)+k_{n3}x_3(1)\cdots+k_{nm}x_m(1))\\
y_d(2) &= \overline{\mu_1}(2)(k_{10}+k_{11}x_1(2)+k_{12}x_2(2)+k_{13}x_3(2)\cdots+k_{1m}x_m(2))\\
&\quad+\overline{\mu_2}(2)(k_{20}+k_{21}x_1(2)+k_{22}x_2(2)+k_{23}x_3(2)\cdots+k_{2m}x_m(2))+\ldots\\
&\quad+\overline{\mu_n}(2)(k_{n0}+k_{n1}x_1(2)+k_{n2}x_2(2)+k_{n3}x_3(2)\cdots+k_{nm}x_m(2))\\
&\vdots \qquad\qquad\qquad \vdots \qquad\qquad\qquad \vdots\\
&\vdots \qquad\qquad\qquad \vdots \qquad\qquad\qquad \vdots\\
y_d(Z) &= \overline{\mu_1}(Z)(k_{10}+k_{11}x_1(Z)+k_{12}x_2(Z)+k_{13}x_3(Z)\cdots+k_{1m}x_m(Z))\\
&\quad+\overline{\mu_2}(Z)(k_{20}+k_{21}x_1(Z)+k_{22}x_2(Z)+k_{23}x_3(Z)\cdots+k_{2m}x_m(Z))+\ldots\\
&\quad+\overline{\mu_n}(Z)(k_{n0}+k_{n1}x_1(Z)+k_{n2}x_2(Z)+k_{n3}x_3(Z)\cdots+k_{n}x_m(Z))
\end{aligned} \tag{4.36}$$

where m is the number of input variables, n is the number of neurons in Layer 3.

In the matrix form, we can write:

$$y_d = AK \tag{4.37}$$

where $y_d = \begin{bmatrix} y_d(1) \\ y_d(2) \\ \vdots \\ y_d(Z) \end{bmatrix}$, and

$$A = \begin{bmatrix} \overline{\mu_1} & \overline{\mu_1}(1)x_1(1) & \cdots & \overline{\mu_1}(1)x_m(1) & \cdots & \overline{\mu_n}(1) & \overline{\mu_n}(1)x_1(1) & \cdots & \overline{\mu_n}(1)x_m(1) \\ \overline{\mu_1} & \overline{\mu_1}(2)x_1(2) & \cdots & \overline{\mu_1}(2)x_m(2) & \cdots & \overline{\mu_n}(2) & \overline{\mu_n}(2)x_1(2) & \cdots & \overline{\mu_n}(2)x_m(2) \\ \vdots & \vdots & \ddots & \vdots & \ddots & \vdots & \vdots & \ddots & \vdots \\ \overline{\mu_1} & \overline{\mu_1}(Z)x_1(Z) & \cdots & \overline{\mu_1}(Z)x_m(Z) & \cdots & \overline{\mu_n}(Z) & \overline{\mu_n}(Z)x_1(Z) & \cdots & \overline{\mu_n}(Z)x_m(Z) \end{bmatrix} \begin{matrix} n \geq 0 \\ m \geq 0 \end{matrix}$$

(4.38)

where k is $n(1+m)\times 1$ vector of unknown consequent parameters as shown (4.38):

$$k = [k_{nm}]^T = [k_{10} \quad k_{11} \quad k_{12} \quad \cdots \quad k_{1m} \quad k_{20} \quad k_{21} \quad k_{22} \quad \cdots \quad k_{2m} \quad \cdots \quad k_{n0} \quad k_{n1} \quad k_{n2} \quad \cdots \quad k_{nm}]^T$$

The actual network output, y_{ANFIS}, is determined once the rule consequent parameters have been established. The actual network output is then compared with the desired output (y) which defines the error vector between these two outputs as shown in (4.39).

$$e = y_d - y \tag{4.39}$$

Once the forward pass has been completed and the error determined, the second part of the epoch is implemented, which is the backward pass. Here, the back propagation algorithm is applied, and the error determined from the equation above is propagated back through the network. The antecedent parameters are updated according to the chain rule, and depending on how many epochs are specified for training, the process continues.

To determine how well the fuzzy inference system has learnt during the training process it is important to validate the model. Model validation is defined as the process

by which the input vectors form the input-output data sets (on which the fuzzy inference system was not trained) are presented to the trained fuzzy inference system model, with model outputs compared to expected output values..

4.2.3 Input/output of the ANFIS

In ANFIS, the input selection plays an important role in achieving the model's desired performance. Hence, it is very important to know which input most affects the system output parameters. It is often useful to neglect inputs having less effect on outputs, as too many inputs may compromise ANFIS performance.

In the diesel-hydrogen generator model, the ANFIS inputs are the power consumption by load, diesel and hydrogen flow into the generator, as well as the previous frequency. The system output is the current frequency, shown in Fig. 4.18:

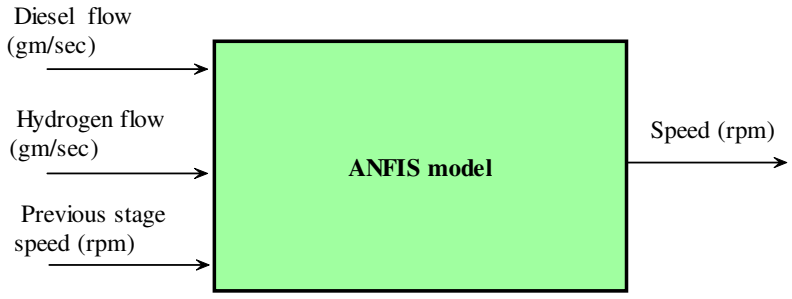

Fig. 4.18. The ANFIS model.

4.2.4 Structure of the ANFIS

The following parameters play an important role in training the ANFIS:

- Size and diversity of training set;
- Number of iterations;
- Type of fuzzy membership function; and
- Number of fuzzy membership functions associated with each set of input data.

The size and diversity of the training data plays an important role in training the ANFIS. The ANFIS model works well if the training data set is sufficient and diverse enough to represent the system's characteristics.

The number of training iterations is an important factor in ANFIS performance. As the number of iterations is responsible for proper tuning of the membership function, it is very important that this number be sufficient. It has been reported that the ANFIS performance improves with a higher number of training iterations. However, as the number increases, training time also increases. Therefore, it is important to obtain an optimum number of training iterations for each case. In this model, the optimum number is found to be 15, which means the performance remains the same if the iteration number increases.

There are many types of fuzzy membership functions and they perform differently for different cases. There is also no straight-forward rule for choosing a membership function, and thus a trial and error method is often employed. To estimate the speed of the diesel-hydrogen generator based on the injection ratio, a 'generalized bell' membership function is used, as shown in Fig. 4.19. This has been chosen for its smoothness and concise notation, and because the boundaries are wide enough to provide accurate results for variable data.

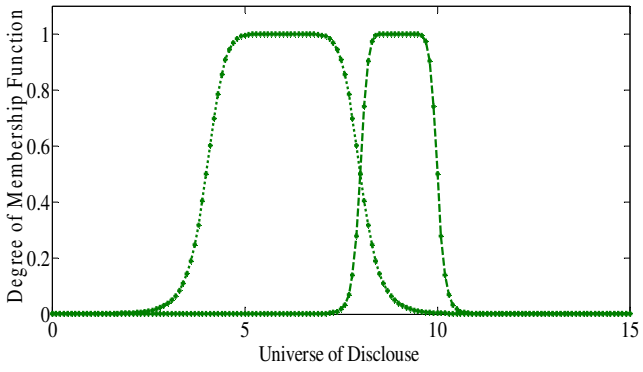

Fig. 4.19. 'Generalized bell' membership function.

The number of membership functions associated with each input depends both on system complexity and size of the training set. As a general rule, the ANFIS performs better if the number of membership functions increase. However, in some cases it provides unrealizable results if the membership functions number exceeds a certain value. The training time also drastically increases if the number of membership functions increases. Consequently it is very important to establish an optimum number of membership functions and in this model, the number of fuzzy membership functions for each input is three.

4.2.5 Case Studies and Model Verification

Several case studies are presented to verify the model's performance. In the first case study, the injection ratio of diesel and hydrogen is retained at 30. The generator's frequency response is shown in Fig. 4.20. In the second case study, the injection ratio of diesel and hydrogen is maintained at 18. The frequency response of the generator is shown in Fig. 4.21. In the third case study, the injection ratio of diesel and hydrogen is retained at 25. The generator's frequency response is shown in Fig. 4.22. Model error is calculated using the mean absolute percentage error (MAPE) as shown below [175]:

$$MAPE = \frac{\sum_{i=1}^{N} \left(\left| y_i^{actual} - y_i^{predicted} \right| \right)}{y_{mean}} \tag{4.40}$$

where y_i^{actual} and $y_i^{predicted}$ are the actual and predicted values of the generator speed at *i*th instant of time, y_{mean} is the average value of the generator speed over a time period of *N*.

The Model's estimated error is calculated as 1.7%, 0.9% and 2.3%. As this is very low, the model is clearly able to estimate the frequency of the diesel-hydrogen generator for different diesel hydrogen mixture ratios.

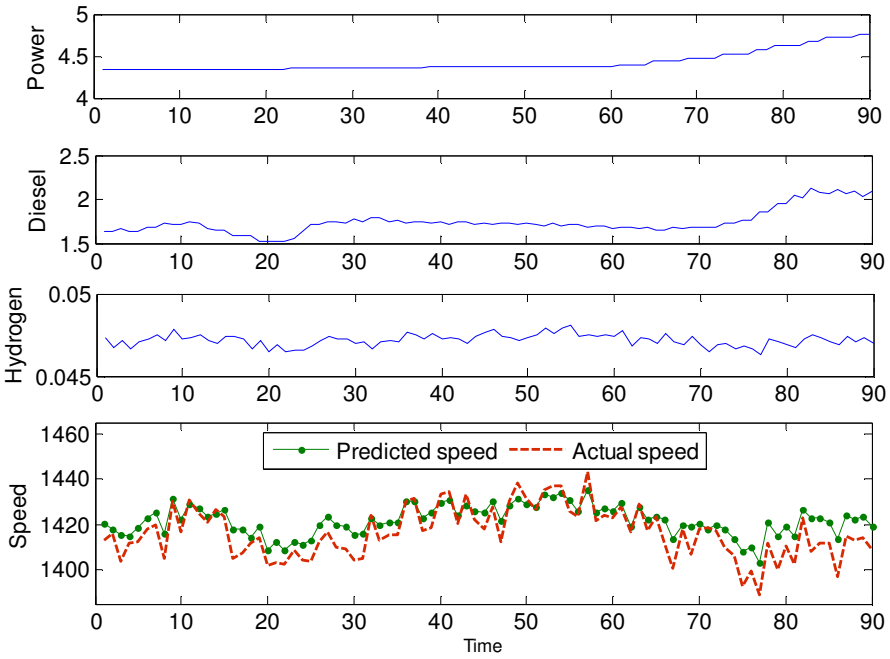

Fig. 4.20. Case Study 1: the injection ratio of diesel and hydrogen is 30.

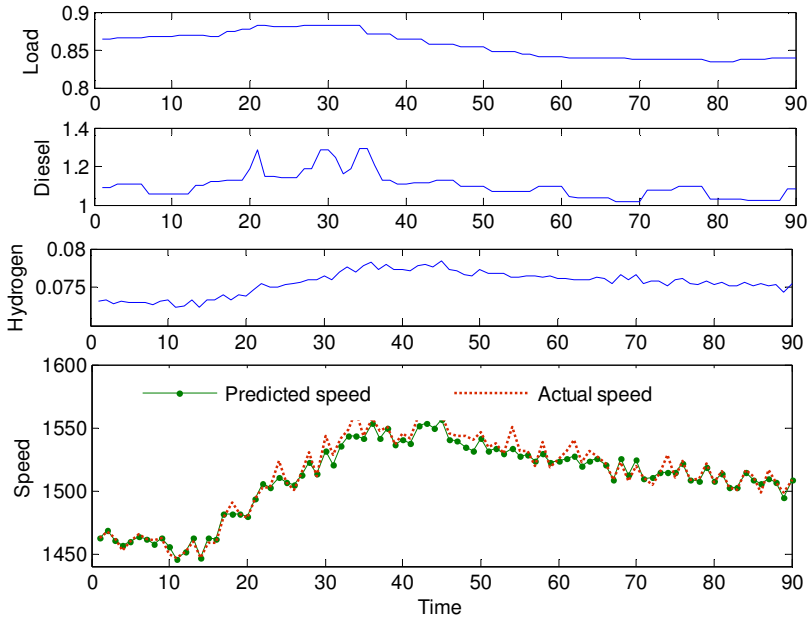

Fig. 4.21. Case Study 2: the injection ratio of diesel and hydrogen is 18.

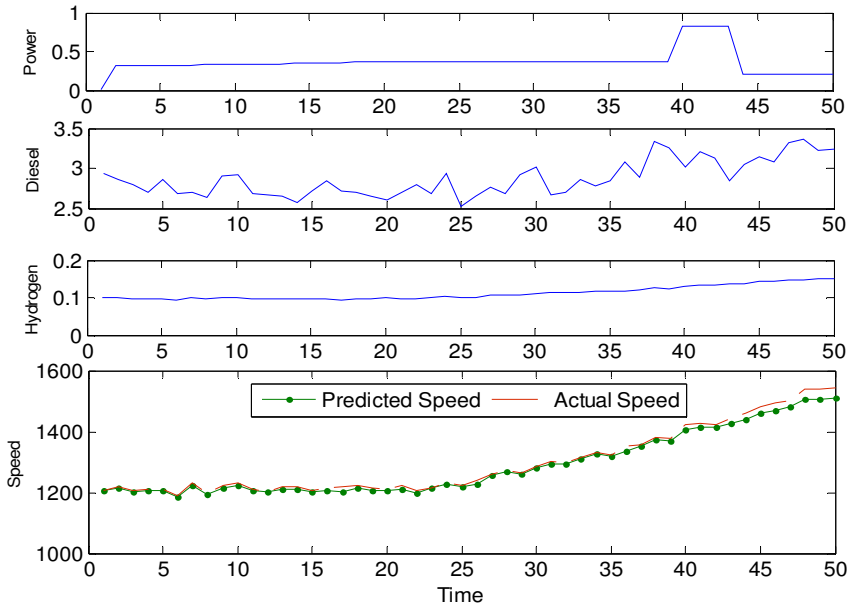

Fig. 4.22. Case Study 3: the injection ratio of diesel and hydrogen is 25.

4.3 Diesel Generator Synchronization and Power Sharing

In the hybrid power system, the diesel generator can be used in isochronous or power sharing modes. In the isochronous mode, the generator works alone and regulates system voltage and frequency. However, in the power sharing mode it shares power with the wind turbine and energy storage system as required.

In order to share power, the diesel generator has to be synchronized with the system. In the synchronization process, the voltage, frequency and phase angle are checked with the system voltage, frequency and phase angle. When the system voltage, frequency and phase angle match those of the diesel generator, it is connected to the system. Once connected, the power sharing equation is applied:

$$P_D(t) + P(t) = P_L(t) \tag{4.41}$$

where $P_D(t)$ is the required power from the diesel engine, $P_L(t)$ is the load demand and $P(t)$ is available power from other sources.

The proposed power sharing is based on the frequency droop control method, in which the generator's output voltage frequency is drooped to control its output power. A block diagram of the scheme is shown in Fig. 4.23. It can be seen that while a difference exists between measured mechanical power (P_m) and reference mechanical power (P_{mref}), the speed reference frequency will vary until the required output power is achieved [182].

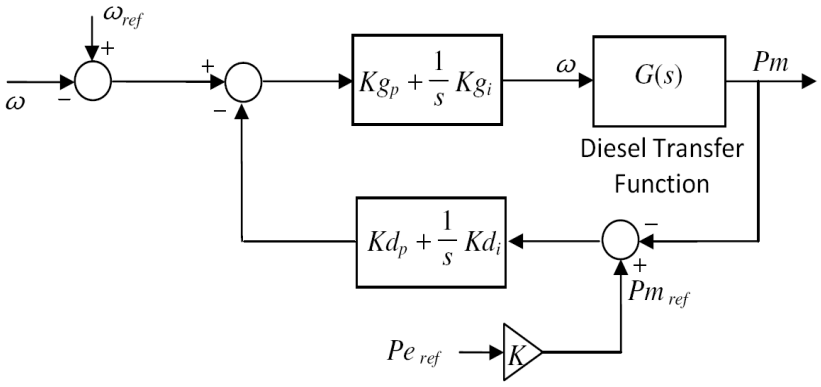

Fig. 4.23. Block diagram of the proposed power sharing scheme.

4.3.1 Simulation of Power Sharing of Diesel Generator

A simulation study is conducted to verify the performance of the power sharing algorithm of a diesel generator with other power generation sources. In this study, the diesel generator shares power with the wind turbine. The power from the wind turbine is regulated as discussed in Chapter 2. Load demand data and power generated from this turbine are presented in Table 4.2.

Table 4.2. Load demand and power from wind.

Time (seconds)	3	6	8	12
Load demand (kW)	210	185	235	220
Power from wind turbine (kW)	210	140	140	110

From Table 4.2, it is seen that at a time of 3 seconds, the load demand and power derived from the wind turbine are equal. However, at 6 seconds, while the load demand drops from 210 kW to 185 kW and the output power from the wind turbine decreases from 210 kW to 140 kW, the diesel generator must act to deliver the deficit power. The generator is synchronized with the system at a time of 5.37 seconds. The generator's voltage and frequency during the synchronization process is shown in Figs 4.25 and 4.26. It is seen that during synchronization, the output voltage, frequency and phase angle of the diesel generator match those of the wind turbine. From a time of 6 seconds, the diesel generator begins delivering the deficit power, as shown in Fig. 4.24 (c).

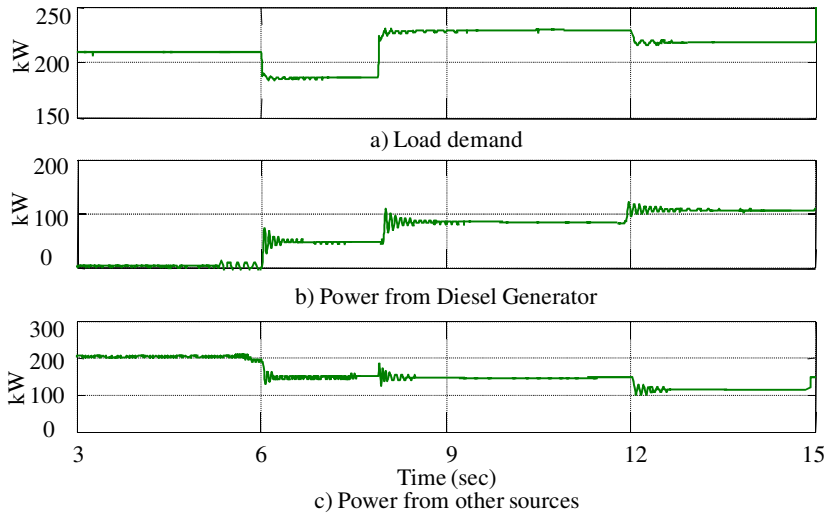

Fig. 4.24. Diesel generator response in power sharing mode: a) load demand, b) power from diesel generator and c) power from wind turbine.

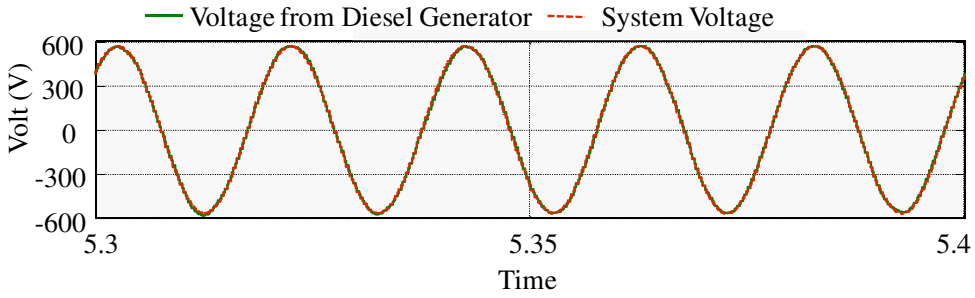

Fig. 4.25. Voltage during synchronization process (at 5.37 seconds).

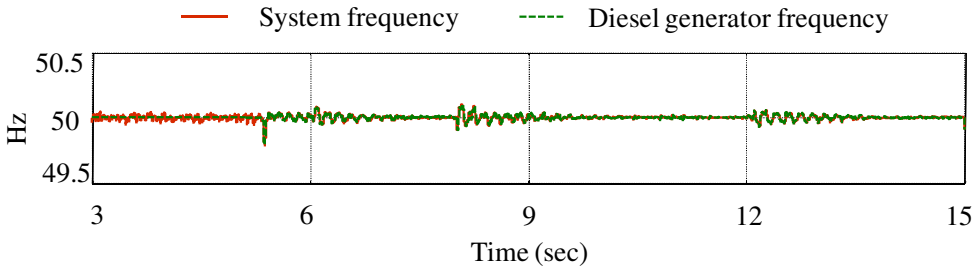

Fig. 4.26. System frequency.

Conclusion

In this chapter, mathematical modelling of the diesel generator system is presented. Black-box modelling of the dual-fuel diesel-hydrogen generator is also discussed. The performance of hydrogen as a fuel is evaluated using the dual-fuel engine. Several experiments have been carried out on the engine under different loading conditions, where the hydrogen amount was fixed at a constant value, and the governor controlled to regulate the speed at different loading conditions. Based on several on-line measurements, an ANFIS model has been developed to estimate the engine speed from the fuel (diesel/hydrogen) ratios. The performance of the 'black-box' model is evaluated using real-time data. The power sharing algorithm of the diesel generator is also developed and tested using simulation. From the results obtained, it is seen that the diesel generator can be used in either stand-alone operation or power sharing modes.

Chapter 5

System Control and Coordination

This chapter outlines the overall control strategy of the proposed renewable energy-based hybrid power system. This system consists of a wind turbine, fuel cell, electrolyzer, battery storage unit, diesel generator and a set of loads. The system's overall control strategy is based on a two-level structure. The top level is the energy management and power regulation (EMPRS) system. Depending on wind and load conditions, this system generates reference operating points to low level individual sub-systems. It also controls the load scheduling operation during unfavorable wind conditions with inadequate energy storage in order to avoid system black-out. Based on the reference operating points of the individual sub-systems, the local controllers control the wind turbine, fuel cell, electrolyzer, battery storage and diesel generator units. The proposed control system is implemented with MATLAB/Simpower software and tested for various wind and load conditions. Results are presented and discussed.

5.1 Configuration of Proposed Hybrid Power System

The proposed hybrid renewable energy-based stand-alone power system consists of wind turbine, energy storage system, fuel cell, electrolyzer and loads as shown in Fig. 5.1. Here, the wind turbine, battery storage system, fuel cell and electrolyzer are connected to the dc link by appropriate power electronic circuits. Finally, a set of ac loads is connected to the system via a controlled inverter. Fig. 5.1 also shows that the power electronic circuits are controlled for achieving optimum system performance.

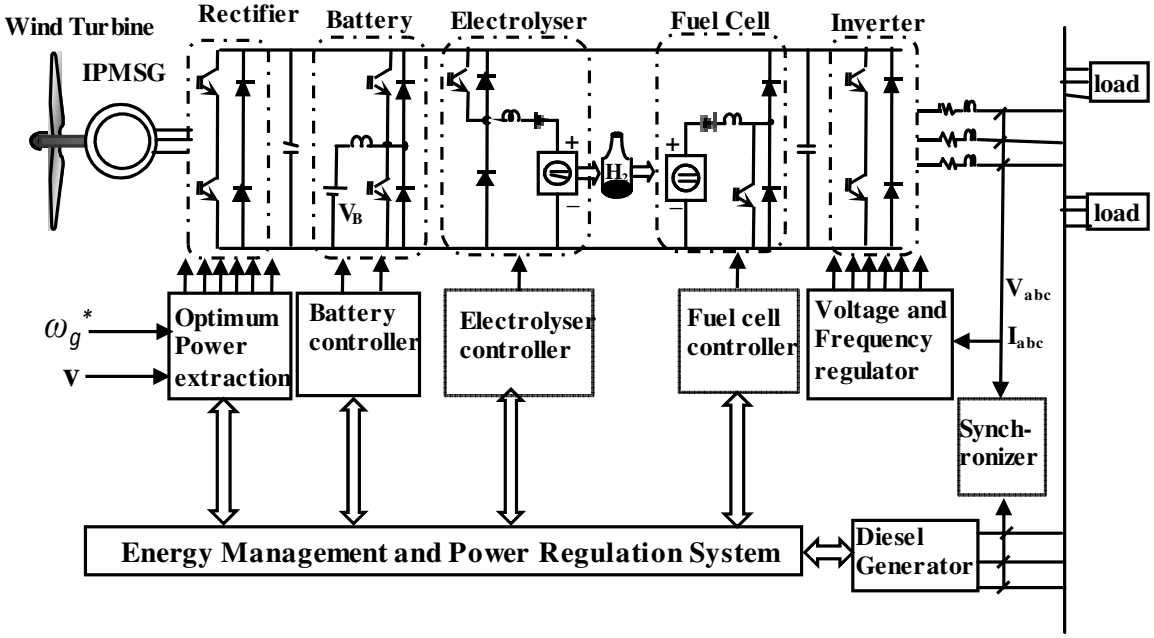

Fig. 5.1. Hybrid power system.

- **Wind turbine controller**

In this project, the wind energy conversion system consists of a variable speed wind turbine-based on as interior type permanent magnet (IPM) synchronous generator is used. The wind energy conversion system is connected to the dc link through a PWM controlled rectifier, which is designed to achieve a) optimum power from the wind by controlling the rotor speed and b) efficient operation of the IPM synchronous generator by controlling the *d*- and *q*- axes component of the stator current. The modelling and control technique is discussed in Chapter 2.

- **Battery storage controller**

A lead-acid battery is used in the project, connected to the system's dc link of the system through a bi-directional dc-dc converter. This converter is controlled so as to

control charging and discharging of the power/current of the battery storage system. The modelling and control techniques are discussed in Chapter 3.

- **Fuel cell controller**

A PEM fuel cell is used in the project, which is connected to the dc link of the system through a boost converter. This converter is controlled to regulate the fuel cell's power output. The modelling and control techniques are discussed in Chapter 3.

- **Electrolyzer Controller**

An alkaline electrolyzer is used in the project, connected to the dc link of the system through a buck converter. This converter is controlled to regulate the electrolyzer's power consumption. The details modelling and control techniques are discussed in Chapter 3.

- **Diesel Generator Model and Control**

A standby diesel generator is included in the project for use in emergency conditions. The modelling and control of the diesel and duel fuel diesel-hydrogen generator are discussed in Chapter 4, together with the power sharing algorithm of the diesel generator and other power generation sources.

5.2 Proposed System Parameter

The parameters used for the proposed hybrid stand-alone power system are shown in Table 5.1.

Table 5.1. System parameters

Permanent Magnet Synchronous Generator	
Number of pole pairs	4
Rated speed (rpm)	1260
Rated power (kw)	1
Stator resistance (ohm)	5.8
Direct inductance (mh)	0.0448
Quadrature inductance (mh)	0.1024
Inertia	0.011
Wind Turbine	
Rated power (kW)	1.1
Base wind speed (m/s)	12
RC Filter	
Series inductance (mh)	13
Shunt capacitance (micro F)	20
Emergency Storage System (Section A)	
Number of battery in series	12
Number of battery in parallel	1
Rated voltage (volt)	4.2
Rated current (amp)	5
Rated capacity (amp-hour)	0.1
Emergency Storage System (Section B)	
Number of battery in series	12
Number of battery in parallel	200
Rated voltage (volt)	4.2
Rated current (amp)	5
Rated capacity (amp-hour)	20
Fuel Cell	
Type of fuel cell	
Nominal voltage (volt)	24.23
Nominal current (amp)	52
Number of cell	42
Operating temperature (^{O}c)	55
Rated power (kW)	1.26
Electrolyzer	
Type of electrolyzer	Alkaline type
Number of cell	30
Nominal voltage (volt)	60
Nominal current (Amp)	60
Operating temperature (^{O}c)	80
Rated power (kW)	3.6

5.3 Overall Control, Coordination and Management Scheme

The supervisory controller is responsible for the overall coordination and management of the individual power plants of a hybrid power system. The supervisory controller's objectives are as follows:

- To ensure individual power plants operate at their optimal level.
- To ensure proper management of state of charge (SOC), for a longer life of battery storage system.
- To ensure efficient operation of the fuel cell and diesel generator.
- To ensure continuous operation of the system.

5.3.1 Energy Management and Power Regulation System

In this project, proposed EMPRS is developed, which acts as a supervisory controller for ensuring a proper coordination of energy generating units and loads. The EMPRS works in three stages. In the first stage, the EMPRS predicts the wind and load profile for a specified period of time. In the second stage, based on the wind and load profile and the status of energy reserve, the EMPRS schedules the maximum load able to be supplied by the system. In the third stage, the EMPRS determines the operating conditions of each sub-system.

- **Wind and load prediction**

Accurate wind and load prediction is key to ensuring a robust performance of the EMPRS. In several studies conducted earlier, it was demonstrated that an accurate forecasting system can be developed for the short-term (up to 15 minutes) predicting of wind and load conditions [183]-[186]. An integration of wind and load prediction in the EMPRS will allow implementation of load curtailment in advance, thus avoiding system black-outs, as will be demonstrated below.

- **Load management algorithm**

Based on the wind and load prediction, the power balance equation of the hybrid system can be expressed as follows:

$$P_{out} = P_L \pm P_B + P_{ELZ} - P_{FC} - P_{DG} \tag{5.1}$$

where P_{out}, P_L, P_B, P_{ELZ} , P_{FC} and P_{DG} are the output power from wind turbine, load demand, battery power, power consumed by electrolyzer, power from fuel cell, and power from diesel generator, respectively.

From (5.1), during high wind conditions excess power (P_{Ex}) is consumed by the electrolyzer and battery storage as follows:

$$P_{Ex} = P_L - P_{out} = -(P_{ELZ} + P_B) \tag{5.2}$$

During low wind conditions, the power deficit (P_{def}) from the wind can be supplied by the fuel cell and battery storage as follows:

$$P_{def} = P_L - P_{out} = P_{FC} + P_B + P_{DG} \tag{5.3}$$

The energy balance equation can be obtained by integrating (5.3):

$$\begin{cases} \int P_{out} = P_L \pm P_B + P_{ELZ} - P_{FC} - P_{DG} \\ E_{out} = E_L \pm E_B + E_{ELZ} - E_{FC} - E_{DG} \end{cases} \tag{5.4}$$

where E_{out} is the total energy produced by the wind energy conversion system, E_L is the total energy consumed by the load, E_B is the total energy supplied by the battery, E_{ELZ} is the total energy consumed by the electrolyzer, E_{FC} is the total energy supplied by the fuel cell and E_{DG} is the total energy supplied by the diesel generator.

However, under real hybrid system operating conditions, (5.4) is only valid for the following:

- If $E_{out} > E_L$, the excess energy is stored in the hybrid system.
- If $E_{out} < E_L$, the energy deficit from wind is balanced by the fuel cell, battery storage and diesel generator. In this case, the fuel cell and battery storage can produce required power provided the hydrogen storage and SOC of the battery are available. The system may experience black-out conditions if the energy reserves are not sufficient to meet the load demand.

The robustness of EMPRS depends on its prediction accuracy. Although it has been demonstrated that the short-term prediction error can be as low as 1% for normal conditions, this can increase with sudden wind guests or large industrial load changes. As a result, sufficient reserves must be allocated to offset the prediction error of up to 5%.

Moreover, the unlikely event of no wind conditions may occur and continue for a relatively long period. Here, the hybrid system will be completely dependent on the stored energy and diesel generator. Thus, energy reserves able to serve high priority loads for sufficient periods must be preserved.

Considering practical operational aspects during low wind conditions, the management of energy reserves of the hybrid system is vital. To ensure the system operation, the load curtailment is adopted, and the load management algorithm is shown in Fig. 5.2; described as follows:

- Calculate the total energy difference $(\mathrm{E_d})$ between the wind energy $(\mathrm{E_{out}})$ and the load demand $(\mathrm{E_L})$ as follows:

$$E_d = E_{out} - E_L \tag{5.5}$$

- If $\mathrm{E_{out}} > \mathrm{E_L}$, check SOC of the battery and the status of the hydrogen storage. If SOC>75%, no load curtailment is required. If SOC<75% and extra energy from wind and power from the fuel cell and diesel generator are insufficient to bring the SOC to 75%, the load curtailment is executed.

- If $E_{out} < E_L$, check SOC of the battery. If SOC>75% and the fuel cell, battery and diesel generator can supply the energy deficit, no load curtailment is needed. For other conditions, load curtailment is implemented.

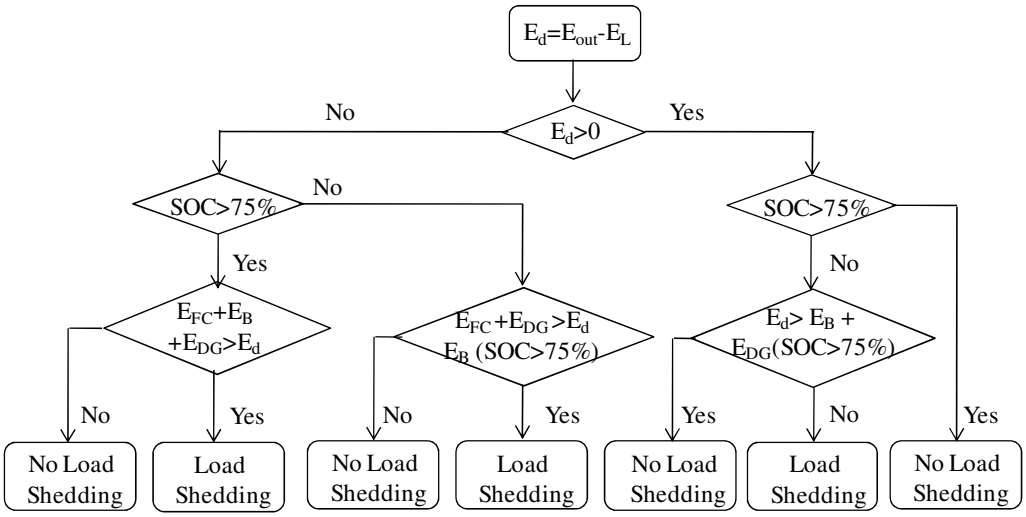

Fig. 5.2. The load management algorithm.

To implement the load curtailment, loads are divided based on priority. Loads for hospitals, police stations etc. can be designated as high priority or emergency loads. The hybrid system must fulfil these load power demand under any conditions. On the other hand, some lighting loads, washing machine loads etc. can be regardedd as low priority; able to be switched off when required.

- **Mode of Operation**

The EMPRS generates the operation points based on current wind and load conditions and actual limitations of each sub-system. Limitations includes the maximum and minimum power of the fuel cell ($P_{FC\_max,}$ P_{FC_min}) for operation in ohmic regions, the maximum charging or discharging power (P_{B_max}), and the maximum and minimum state of charge (SOC_{max}, SOC_{min}) of the battery storage system. In this paper, the allowable SOC range is assumed as 40 - 95%. For normal operating conditions, the battery storage system's allowable SOC is assumed to range from 75 - 95%. However, for emergency

operation the SOC is allowed to be as low as 40%. Limitations also include the maximum and minimum power consumption of the electrolyzer ($P_{ELZ\_max,}$ P_{ELZ_min}), and the maximum pressure of the hydrogen cylinder (p_{H2_max}). The operating points are summarized in Table 5.2.

Table 5.2: Modes of system operating conditions

Mode	Operating conditions
Mode 1	• The output power from wind is higher than the load demand ($P_{out} > P_L$). • High level of stored hydrogen ($p_{H2} \approx p_{H2max}$). • High level of battery storage ($SOC \approx SOC_{max}$).
Mode 2	• The output power from wind is higher than the load demand ($P_{out} > P_L$). • A fraction of excess power from wind can be retained in the storage device.
Mode 3	• The output power from wind is higher than the load demand ($P_{out} > P_L$). • Excess power from wind can be retailed in storage system.
Mode 4	• The output power from wind is less than the load demand ($P_{out} < P_L$). • Deficit power ($P_L - P_{out}$) is less than the capacity of fuel cell. • Enough storage in battery.
Mode 5	• The output power from wind is less than the load demand ($P_{out} < P_L$). • Deficit power ($P_L - P_{out}$) is higher than the maximum capacity of fuel cell but within the combined range of fuel cell and battery storage system.
Mode 6	• The output power from wind is less than the load demand ($P_{out} < P_L$). • Deficit power ($P_L - P_{out}$) is less than the minimum capacity of fuel cell. • Enough storage in battery.
Mode 7	• The output power from wind is less than the load demand ($P_{out} < P_L$). • Deficit power ($P_L - P_{out}$) is less than the minimum capacity of fuel cell. • Enough storage in battery.
Mode 8	• The output power from wind is less than the load demand ($P_{out} < P_L$).

	• Deficit power ($P_L - P_{out}$) is higher than the maximum capacity of fuel cell and battery storage system. • Diesel generator acts and supply power at least 30% of its capacity.
Mode 9	• Emergency condition – no wind power due to sever fault or wind gust or no wind conditions for long time. • Low level of stored hydrogen ($p_{H2} \approx p_{H2min}$). • Diesel generator and battery supplies the required power. • SOC of battery storage is allowed to go as low as 40%.

The operating points are described below:

Mode 1: High wind conditions ($P_{out} > P_L$), ($p_{H2} \approx p_{H2\_max}$) and ($SOC \approx SOC_{max}$).

In this mode, the wind turbine extracts optimum power equal to the load demand. The electrolyzer and battery cannot consume any power because the hydrogen tank pressure and the SOC of the battery have reached their maximum limits.

Mode 2: High wind conditions ($P_{out} > P_L$) and ($P_{Ex} > P_{ELZ\_max} + P_{B\_max}$).

In this mode, the wind turbine extracts optimum power equal to the load demand plus battery and the electrolyzer capacities.

Mode 3: High wind conditions ($P_{out} > P_L$) and ($P_{Ex} < P_{ELZ\_max} + P_{B\_max}$).

In this condition, the wind turbine extracts maximum power. The excessive wind power is consumed by the electrolyzer and battery.

Mode 4: Low wind condition ($P_{out} < P_L$), ($75\% \leq SOC < SOC_{max}$), and ($P_{FCmin} < P_{def} < P_{FC\_max}$).

In this condition, the wind turbine extracts the maximum available power. The deficit power is provided by the battery and fuel cell during transient conditions. Once

the system reaches a steady state condition, the deficit power is supplied by the fuel cell alone.

Mode 5: Low wind conditions ($P_{out} < P_L$), ($P_{FC\_max} < P_{def} < P_{FC\_max}+P_{Bmax}$), and ($75\% \leq SOC < SOC_{max}$).

In this condition, the wind turbine extracts the maximum power. The fuel cell provides its maximum power with the battery storage providing the remainder.

Mode 6: Low wind conditions ($P_{out} < P_L$), ($P_{def} < P_{FC\_min}$), and ($75\% \leq SOC < SOC_{max}$).

In this condition, the wind turbine extracts the maximum power while the battery storage provides the necessary power as the power deficit is lower than the minimum power limit of the fuel cell.

Mode 7: Low wind conditions ($P_{out} < P_L$), low SOC ($SOC \approx 75\%$) and ($Pdef < P_{FC\_min}$).

In this condition, the wind turbine extracts the maximum power. The battery cannot provide power as the SOC is close to 75%, which is the minimum limit for normal operating conditions. The fuel cell operates in its ohmic zone. Because the power produced by the fuel cell is higher than Pdef, the extra power is used to charge the battery. When the SOC of the battery storage system reaches about SOC_{max}, the system operation reverts to Mode 6.

Mode 8: Low wind conditions ($P_{out} < P_L$), (P_{DF} (30% of rated load)+ $P_{FC\_max}+P_{Bmax} > P_{def} > P_{FC\_max}+ P_{Bmax}$).

In this condition, the wind turbine cannot meet the load demand. The deficit power is higher than the maximum capacity of the fuel cell and battery storage systems. As a result, the diesel generator must provide power, running on atleast 30% of the rated load. This deficit power will be primarily be provided by the diesel generator (30% of rated power), and remainder by the fuel cell and battery storage system.

Mode 9: Emergency conditions – no wind power.

In this condition, the system needs to rely on the diesel generator and battery storage system. If deficit power exceeds the maximum limit of the battery storage and fuel cell, the diesel generator activates. Here, the diesel generator provides at least 30% of its rated load, with the remainder derived from the fuel cell and battery. In this condition, if the system runs out of hydrogen storage, the EMPRS allows the battery storage to drop as low as 40%.

5.4 Performance Evaluation of EMPRS

Simulation studies are conducted to evaluate the performance of the proposed system under varying wind and load conditions.

5.4.1 Performance of the Local Controllers under Different Wind and Load Conditions

In this section, the performance of the local controllers is evaluated under varying wind and load conditions. The parameters of the wind turbine, IPM synchronous generatorand energy storage system are shown in Table 5.1.

- Dynamic operating points of sub-systems under different wind and loading conditions

Figs 5.3(a) and 5.3(b) show hypothetical wind and load profiles, respectively. The EMPRS determines the operating mode according to current wind and load conditions and available energy reserves. Fig 5.4(a) shows the power generation from the wind energy conversion system, while Fig 5.4(b) shows the electrolyzer, fuel cell and battery power. Fig. 5.4 (c) shows the power from the diesel generator. Figs 5.4(d). 5.4(e) show the status of the hydrogen storage and the SOC of the battery, respectively. Fig 5.4(f) shows the hybrid power system's operation mode.

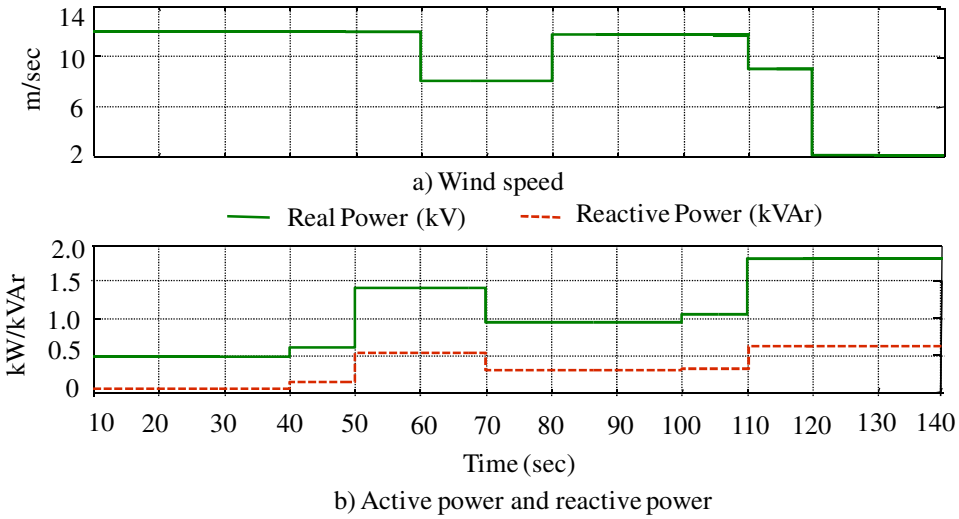

Fig. 5.3. Wind and load profiles.

From Figs 5.3(b) and 5.4(a), the initial load demand is 0.5 kVA (0.48 kW, 0.05 kVAR), and the maximum available power after considering conversion losses is about 0.9 kW. In this condition, the EMPRS operates in *Mode 3,* as the excess wind power can be stored in the battery and consumed by the electrolyzer to produce hydrogen. At the time of 20 seconds, the SOC of the battery reaches its maximum limit (about 95%); hence the battery cannot consume any additional power. In this condition, the EMPRS reverts to *Mode 2,* which allows the wind energy conversion system to extract optimum power (0.85kW) by controlling the rotor speed. Here, the excess wind power is consumed by the electrolyzer.

From Fig. 5.3(b), at the time of 40 seconds, the load increases from 0.5 kVA to 0.65 kVA (0.6 kW). At this time, the pressure of hydrogen storage system reaches its maximum value. As a result, the electrolyzer cannot consume additional power from the wind energy conversion system. In this condition, the EMPRS changes to *Mode 1,* which allows the wind energy conversion system to extract optimum power (0.65kW) by controlling the rotor speed.

From Fig. 5.3(b), at the time of 50 second, the load increases from 0.65 kVA to 1.5 kVA (1.4 kW). Since the maximum available energy from the wind turbine is less than the load demand and the power deficit is within the fuel cell power generation limit, the EMPRS now operates the system in *Mode 4*.

However, at the time of 60 seconds, the wind speed drops from 12 m/second to 8 m/second. As the deficit power is about 1.2 kW (which is within the combined limit of the fuel cell and the battery), the EMPRS operates the system in *Mode 5*.

At the time of 70 seconds, the load decreases from 1.5 kVA (1.4 kW) to 1.0 kVA (0.97 kW). In this condition, the EMPRS operates the system in *Mode 4* as the deficit power is within the fuel cell's limit.

At the time of 80 second, the wind speed increases from 8 m/second to 11.7 m/second. In this condition, as the deficit power (0.170 KW) is less than the minimum fuel cell power limit, the EMPRS operates the system in *Mode 6*.

At the time of 100 seconds, a 0.1 load is connected to the system. At this time, as the SOC of the battery approaches its minimum limit, the EMPRS runs the system in *Mode 7*. In this condition, the fuel cell can produce sufficient power, to balance the deficit power and increase the SOC of the battery.

At the time of 110 seconds, the wind speed drops from 11.7 m/second to 9 m/second and load demand increases from 1.1 kVAr to 2 kVAr (1.8 kW). In this condition, the wind turbine only supplies 0.5 kW power. As the deficit power (1.5 kW) exceeds the battery storage and fuel cell unit maximum limits, the diesel generator is connected to the system to supply power. In this scenario, the diesel generator, fuel cell and battery storage system supply the deficit power. In this case, the fuel cell, diesel generator and battery supply 1.1 kW, 0.3 kW and 0.1 kW, respectively.

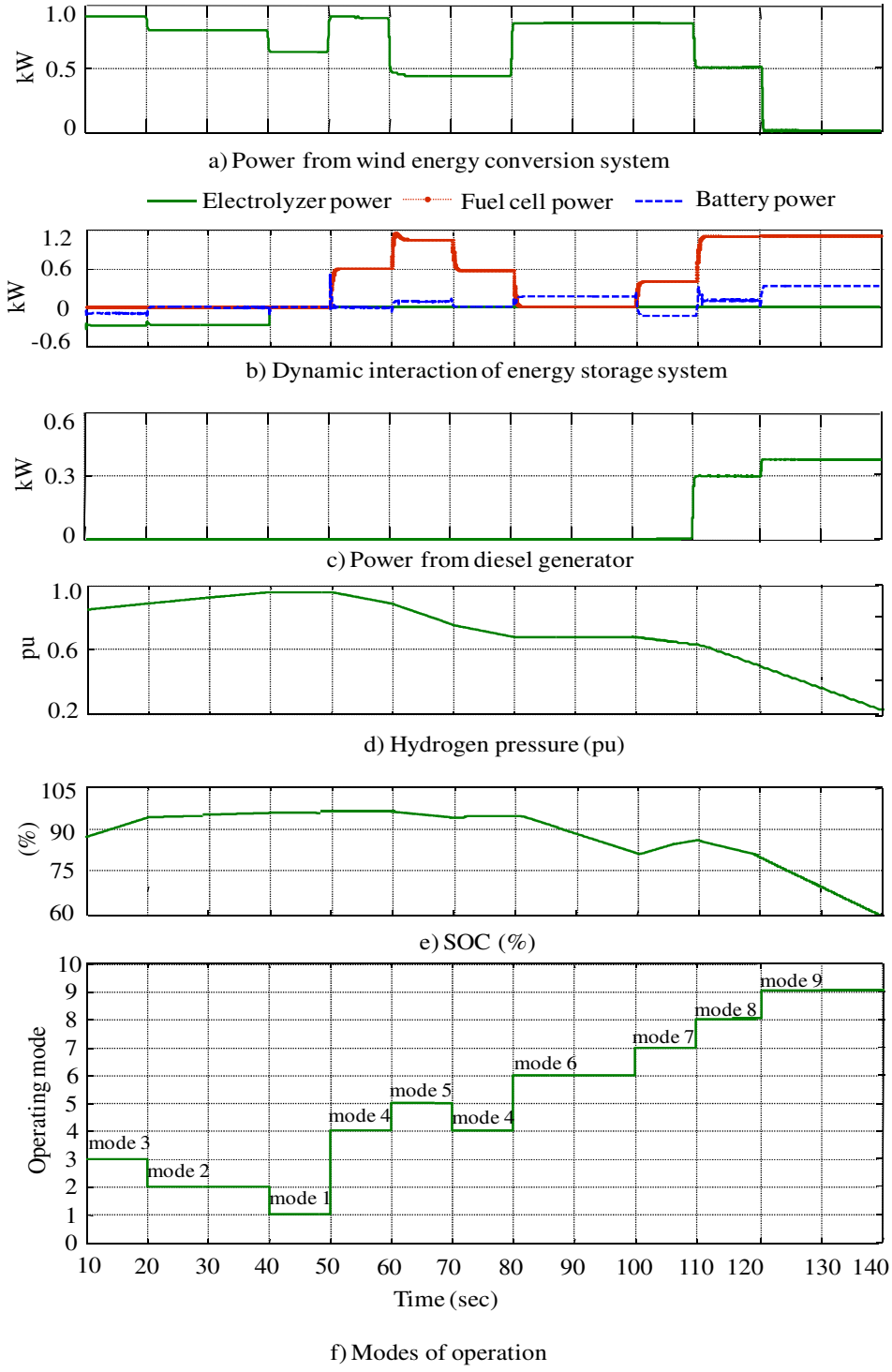

Fig. 5.4. Power balance and operation mode sequence of hybrid system.

At the time of 120 seconds, the wind speed drops to 2 m/second and the wind turbine cannot produce any power. In this condition, the fuel cell, diesel generator and battery storage system supply the total power. As this condition is considered an emergency condition, the EMPRS allows the SOC of battery storage system to be as low as 40%.

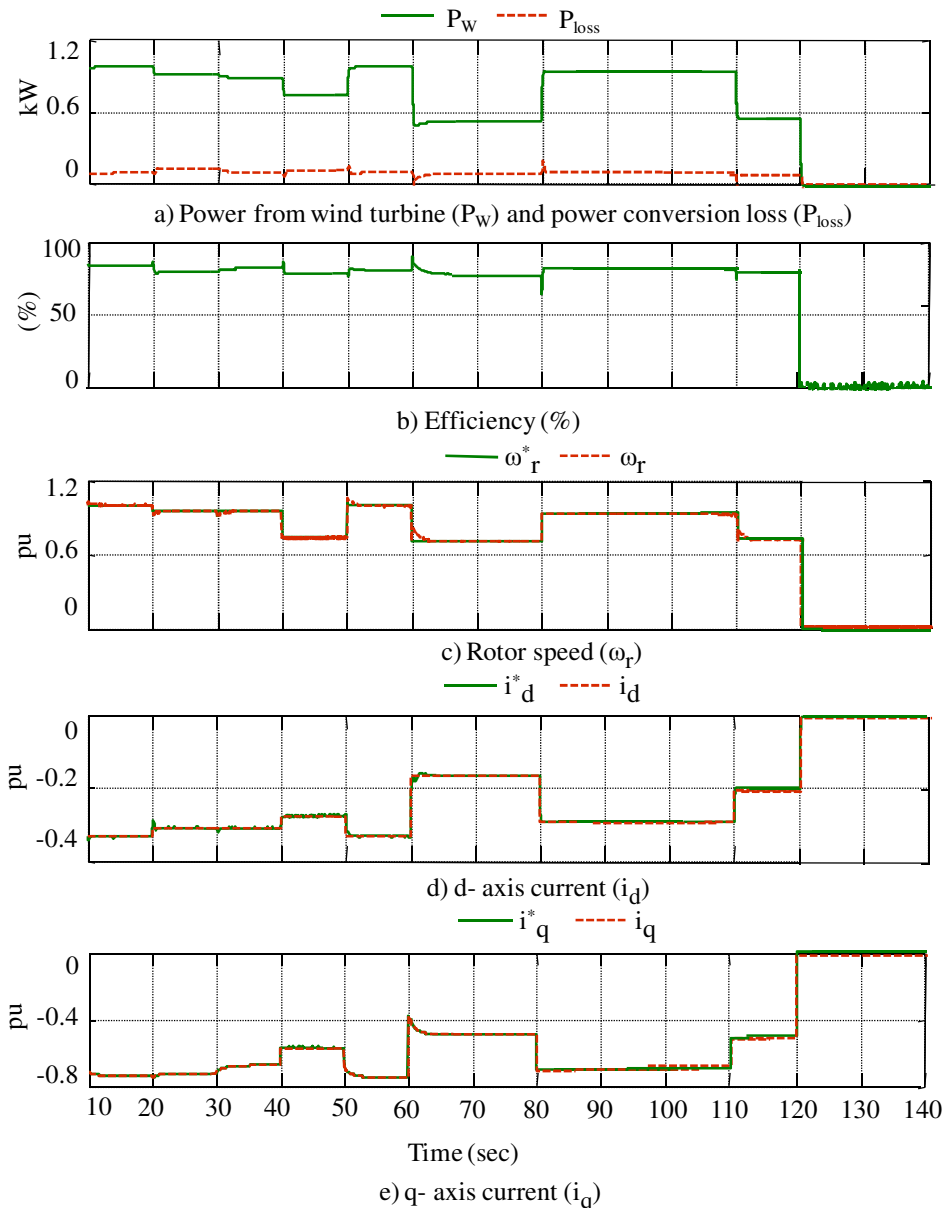

Fig. 5.5. Performance of the wind energy conversion system controller.

- **Performance of the wind energy control system**

Fig. 5.5 demonstrates the performance wind turbine controller. Fig. 5.5(a) shows both power extracted from the wind turbine and power losses. The wind energy conversion system is shown in Fig. 5.5(b). From Fig. 5.5(c), it can be seen that the wind energy control system extracts the optimum power by regulating the rotor speed of the IPM synchronous generator. From Figs 5.5(d) and 5.5(e), the wind energy control system is seen to maintain an efficient operation of the IPM synchronous generator by controlling the *d*- and *q*- axes stator current components.

- **Performance of the electrolyzer controller**

The buck converter is used to control the electrolyzer power flow. The electrolyzer power and current are shown in Fig 5.4(b).

- **Performance of the fuel cell controller**

The boost converter is used to control the dc-link voltage and power flow of the fuel cell, which is shown in Fig. 5.3(b).

- **Performance of the bi-directional battery controller**

As shown in Fig. 5.4(b), the bi-directional dc-dc converter controls the battery charging/discharging power to ensure the power balance and transient stability of the system.

- **Dynamic interaction of the energy storage system**

The dynamic interaction of each energy storage device is shown in Fig. 5.4(b). It can be seen that, under any change of wind speed or load demand, the battery storage system provides or consumes the transient power due to the faster dynamics of its fuel cell counterpart.

- **Performance of diesel generator**

From Fig. 5.4(c), it is seen that the diesel generator can successfully share power with the wind turbine, fuel cell and battery storage system.

- **Performance of the inverter controller**

Fig. 5.6 shows the output voltage and frequency being regulated by the load side inverter controller under varying wind and load conditions. Fig. 5.7 shows the dynamic performance of the inverter at 70 second, when the load decreases from 1.5 kVA to 1.0 kVA. Fig. 5.8 demonstrates the active and reactive power demand response of the inverter.

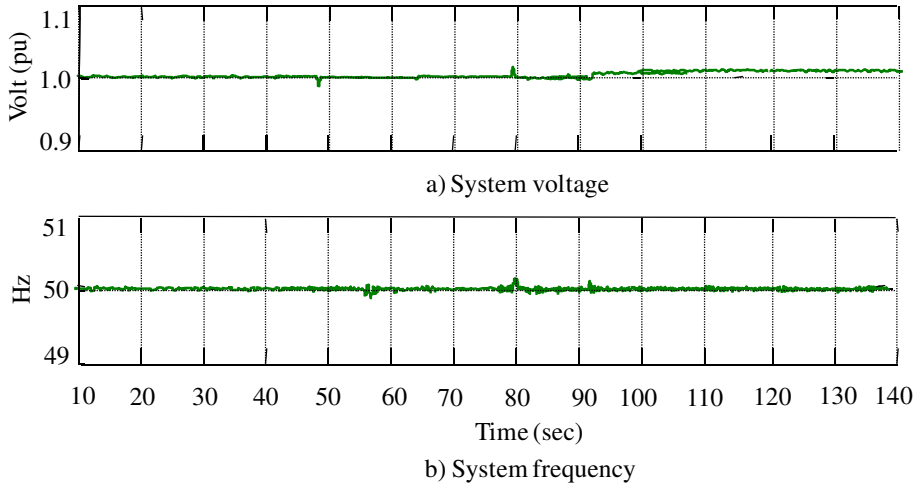

Fig. 5.6. System voltage and frequency.

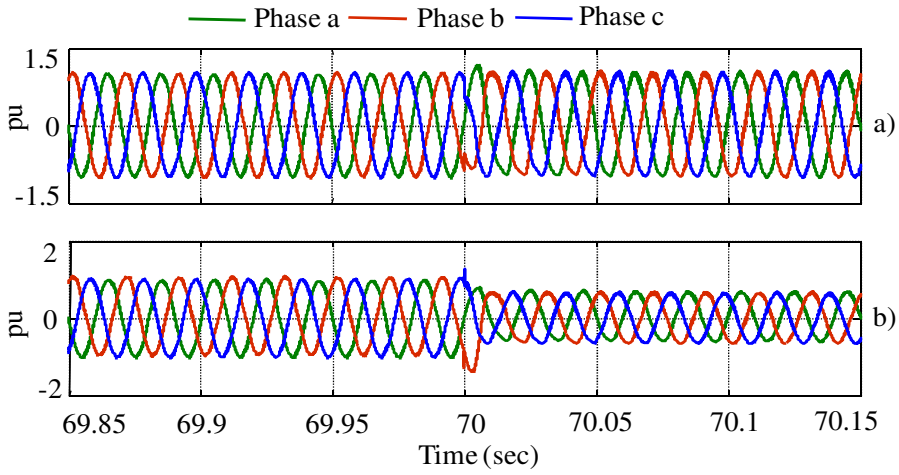

Fig. 5.7. Inverter response during load change at 70 seconds where the load decreased from 1.5 kVA to 1.0 kVA: a) voltage and b) current responses.

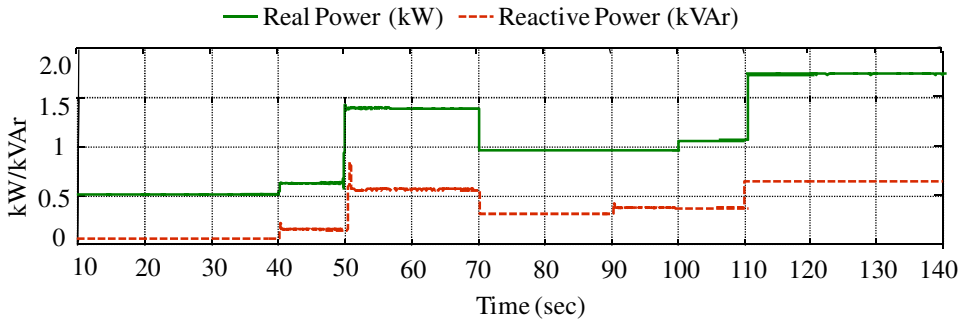

Fig. 5.8. Real and reactive power responses.

5.4.2 Load Management of the System under Low Wind Conditions

The EMPRS performance is evaluated under various realistic wind and load scenarios. Let us assume the proposed hybrid shown in Fig. 5.1 operates in an isolated area. The average load demand is assumed to be about 0.6 kW with a peak load demand of 1 kW. This case study is performed under low wind conditions when the load peak occurs. Let us assume the energy reserve is low and cannot support the system without load curtailment. The parameters for the wind turbine, fuel cell and electrolyzer are derived from Table 5.1.

The wind speed profile is shown in Fig. 5.9(a). A hypothetical wind prediction is assumed with an error of ±5%, while, the corresponding power extracted from the wind turbine is shown in Fig. 5.9(b).

The load profile is shown in Fig. 5.10(a), with loads divided into four categories. Type *LC4* is the load with the highest priority, constituting about 25-30% of the total load. Type *LC3* is a high priority load that constitutes about 25-30% of the total load. Type *LC2* has a medium priority, constituting about 25-30% of the total load. Finally, type *LC1* has the lowest priority. The load curtailment operation is shown in Fig. 5.10(b).

Figs 5.11 (a) and 5.11 (b) show the electrolyzer/fuel cell operations and associated hydrogen storage, respectively. Figs 5.12 (a) and 5.12 (b) show the battery storage

operation and associated SOC, respectively. Fig. 5.13 shows the power from diesel generator. From Figs 5.9-5.13, it can be seen that the EMPRS can operate the system without any load curtailment up to 2:00 hours. However, from 2:00 - 3:24 hours, the EMPRS curtails the load with the lowest priority (*LC1*) as the stored energy is not sufficient to provide the required deficit. At 2:48 hours, the hydrogen storage runs out. Since the energy stored in the battery is not sufficient to run the system, the diesel generator acts to supply power. At 3:24 hours, the SOC of the battery storage is approaching about 75% and a no wind condition is is approaching. In this condition, the diesel generator mainly supplies the load demand. From 3:24 - 3.48 hours, the EMPRS curtails *LC1, LC2, LC3* loads in order to prevent system black-out. During this period, the EMPRS uses the emergency reserves of the battery and diesel generator to supply power only to the highest priority loads. The wind returns at 3:48 hours, but is not sufficient to provide load demand. In this condition, the EMPRS curtails *LC1, LC2* because the SOC of the battery is too low. At 4:42 hours, the diesel generator shuts down as power from the wind turbine and battery storage system can satisfy the load demand. During this period, if the wind power exceeds the load demand, the excess power is used to charge the battery.

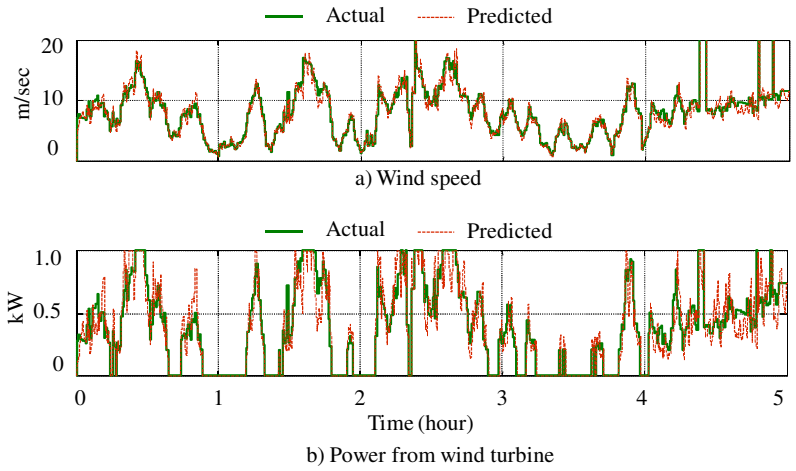

Fig. 5.9. Wind speed profile and generated wind power.

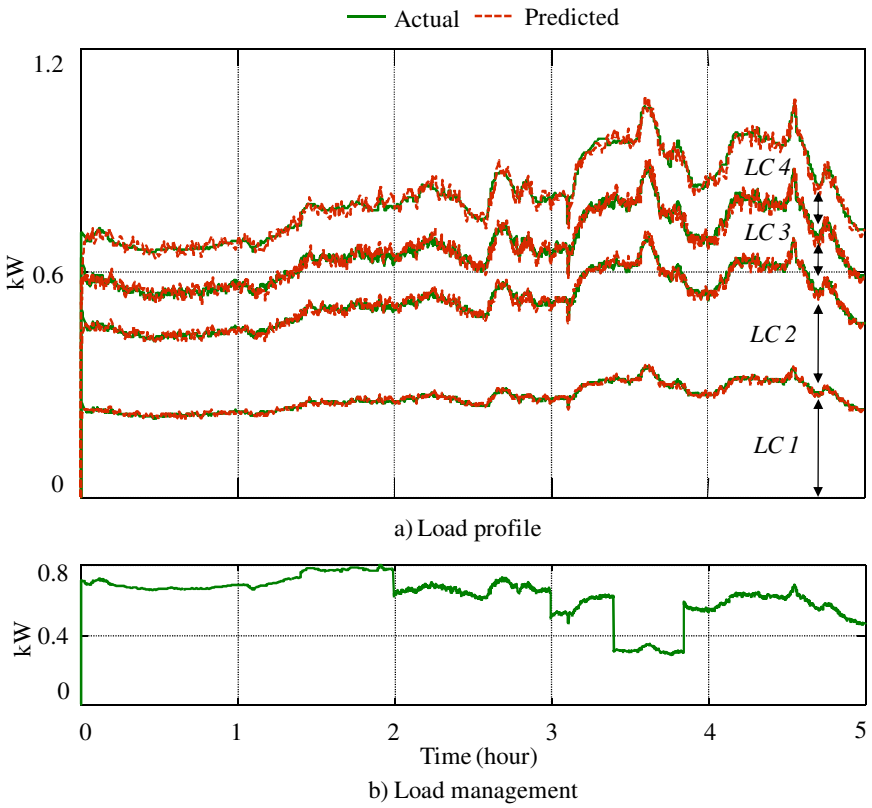

Fig. 5.10. Load conditions.

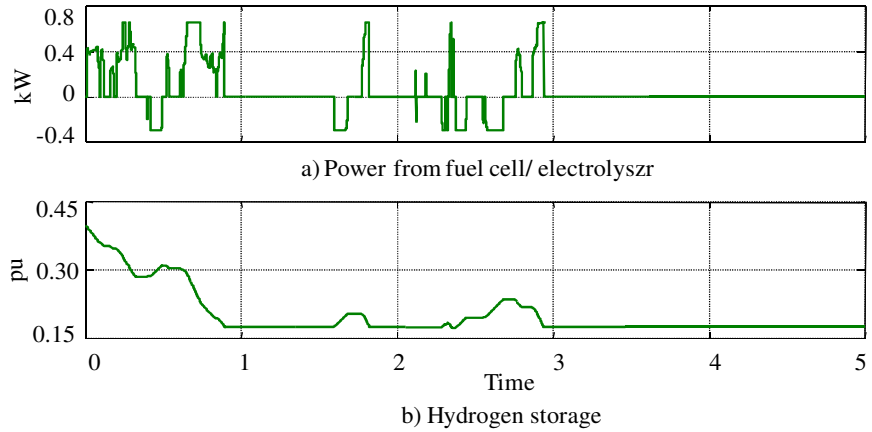

Fig. 5.11. Fuel cell, electrolyzer power and hydrogen status.

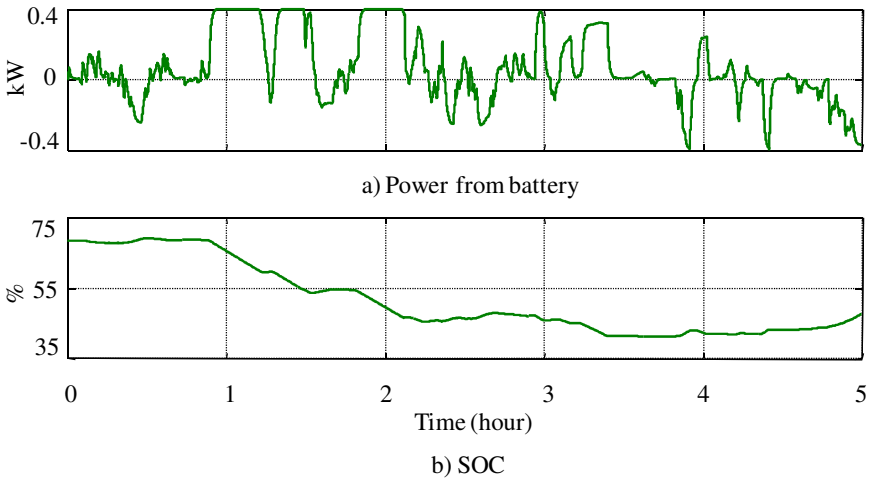

Fig. 5.12. Battery power and SOC.

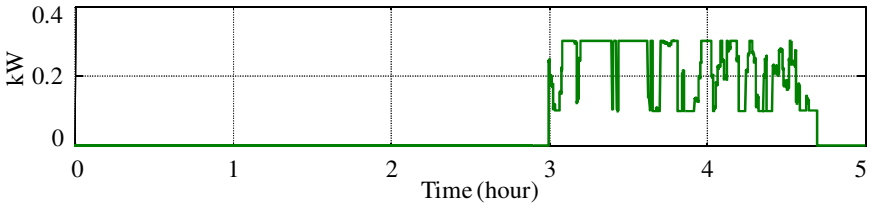

Fig. 5.13. Power from diesel generator.

Conclusion

A novel operation and control strategy for a hybrid power system with energy storage for a stand-alone operation is proposed. The performance of the proposed control strategy is evaluated under different wind and load conditions. From the simulation studies, it is revealed that the machine side converter is able to extract the optimum power. It is also able to operate the IPM synchronous generator with the maximum efficiency. The battery storage system is controlled successfully by a bi-directional converter. The fuel cell and electrolyzer are controlled using a boost-converter and buck converter, respectively. The diesel generator can supply the required power. The overall

co-ordination of the wind turbine, fuel cell, battery storage system, electrolyzer, diesel generator and loads is done by the developed EMPRS. The obvious advantage of the EMPRS is that it can prevent the system from black-outs in the event of low wind conditions or inadequate energy reserves.

\

Chapter 6

Application of the Proposed Stand-Alone Power Supply System: Case Studies

This chapter presents several case studies designed to investigate the application of the proposed hybrid stand-alone power system for a variable wind, load and energy reserve conditions.

6.1 Variables considered for Case Studies

Case studies are performed under actual wind and load data derived from a remote island located in the South Tasmania, with variables listed below:

6.1.1 Wind profile

Fig. 6.1 shows the week-long wind speed over from 1-7 January 2012. Fig. 6.1 indicates that the wind does not follow any trend. From one year data documents, the average wind speed in 2011 in that particular island is 7.87 m/sec with a standard deviation is 3.44. The island's maximum wind speed was 22.83 m/sec.

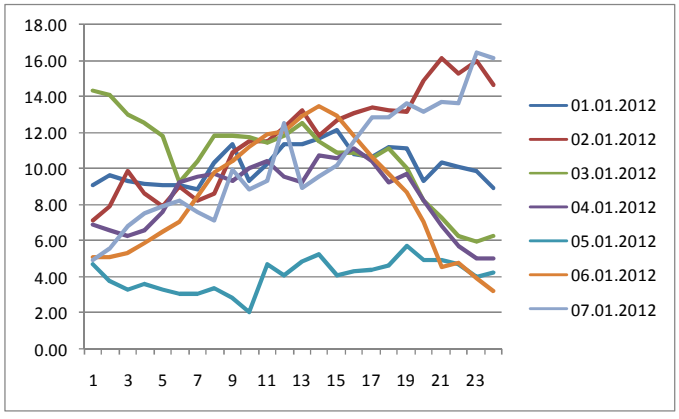

Fig. 6.1. Wind profile from 1-7 January, 2012.

From the data, it is observed that low or no wind conditions can occur for relatively long period several times annualiy. Figs 6.2 and 6.3 show two cases where low wind conditions occurred for longer period during the day. It is noted that low or no wind conditions can occurs during the peak demand period.

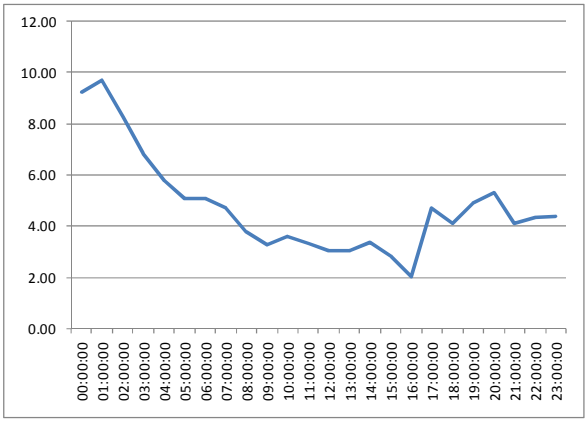

Fig. 6.2. Wind profile from 00:00 hour to 24:00 hour on April 14, 2011.

From Fig. 6.2, it is seen that from 02:00 hours, wind speed declines. At 7:00 hours, a low wind condition occurs when the wind turbine cannot extract any power. However, at 17:00 hours the wind returns, enabling the turbine to extract power.

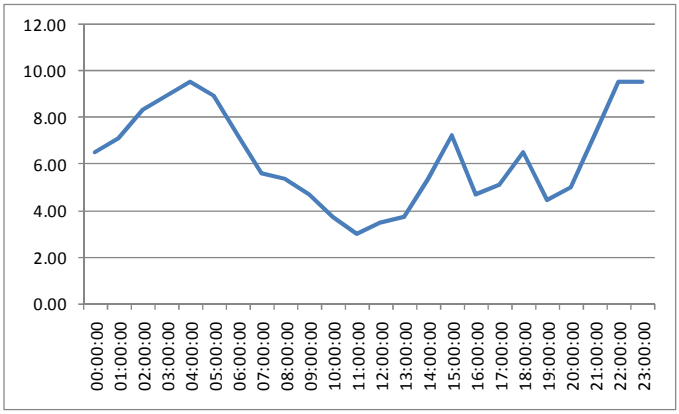

Fig. 6.3. Wind profile from 00:00 hour to 24:00 hour on December 23, 2011.

From Fig. 6.3, it is evident that the wind turbine can extract power from 00:00 hours to 9:00 hours. From 09:00 hours to 13:00 hours, a low wind condition prevents the wind turbine from extracting any power. Finally, at approximately 17:00 hours the wind returns.

6.1.2 Load profile

The load has a unique characteristic, with a peak generally occuring during mornings and evenings. However, the load demand varies on seasonal basis. The average load demand in the summer period (December to February) is lower than during the winter period (June to August). Being an attractive tourist destination, the island experiences a higher load demand during the Easter period. The average hourly load demand in summer, winter, and the Easter period are shown in Figs 6.4 –6.6.

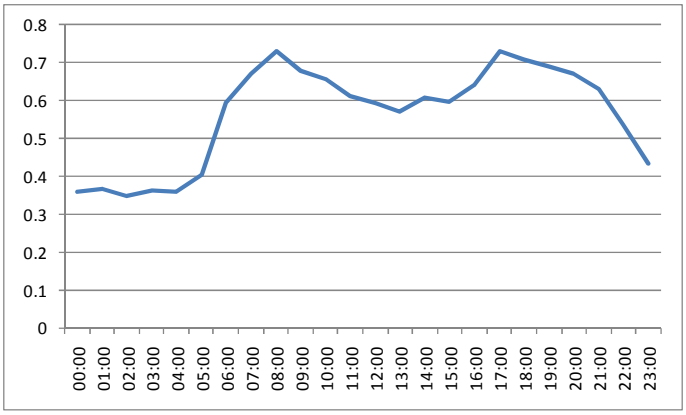

Fig. 6.4. Average hourly load demand during summer period.

Fig. 6.4, shows that peak demand in summer occurs between 7:00 am and 9:00 am and between 16:00 pm and 21:00 pm . The morning and evening average peak is about 0.8 MW.

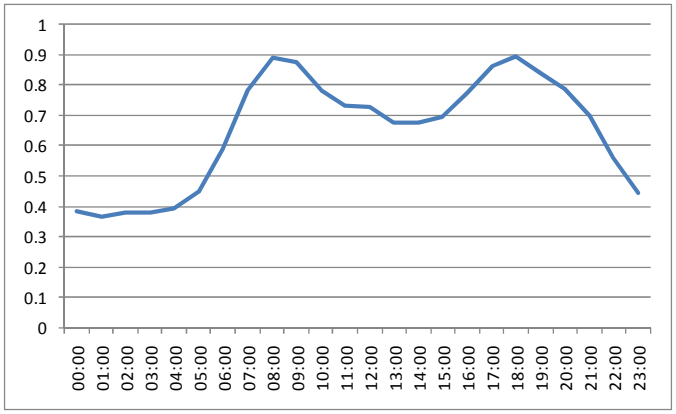

Fig. 6.5. Average hourly load demand during winter period.

Fig. 6.5 indicates it is seen that peak demand in winter occurs between 7:00 am and 10:00 am and between 16:00 pm and 20:00 pm. The morning and evening average peak is approximately 0.9 MW.

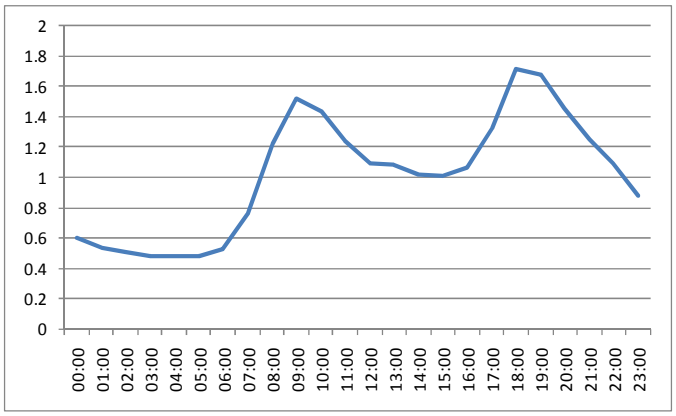

Fig. 6.6. Average hourly load demand during Easter week.

Fig. 6.6 shows that peak demand during the Easter period occurs from 8:00 am to 11:00 am and from 17:00 pm to 20:00 pm. The morning and evening average peak is about 1.5 MW and 1.7 MW, respectively.

6.1.3 Battery management

As discussed in Chapter 5, the SOC of the battery has to be monitored and maintained within a specific range to ensure a longer life operation. The proposed SOC management of the battery under normal conditions is between 75% - 95% and between 40% - 75% under emergency conditions, as discussed in Chapter 5.

6.1.4 Hydrogen storage management

The maximum pressure of hydrogen storage is considered as 1 pu, with minimum pressure 0.1 pu, as discussed in Chaprter 5.

6.1.5 Diesel generator power management

For efficient operation, the minimum power from a diesel generator is 30% of its rated power. As a result, the output power from the diesel generator can vary from 30% of its full load power to its full load power, as discussed in Chapter 5.

6.2 System Sizing

The proposed system components include the wind turbine, battery storage, fuel cell, electrolyzer and diesel generator. The sizing of each system is assumed as follows:

- Wind turbine rating is assumed to cover the peak power (1.8 MW) in base wind speed.
- Fuel cell is 1.0 MW
- Electrolyzer is 1.0 MW
- Battery storage is 0.8 MW (10 MW-hour)
- Diesel generator is 0.6 MW.

6.3 Case Study - low wind conditions during busy Easter period

For this case study, a wind profile is chosen where a low wind condition occurs during peak demand time in the busy Easter season. Proposed system performance is evaluated in terms of a) SOC status and b) hydrogen storage status. The wind and load profiles are shown in Fig. 6.7.

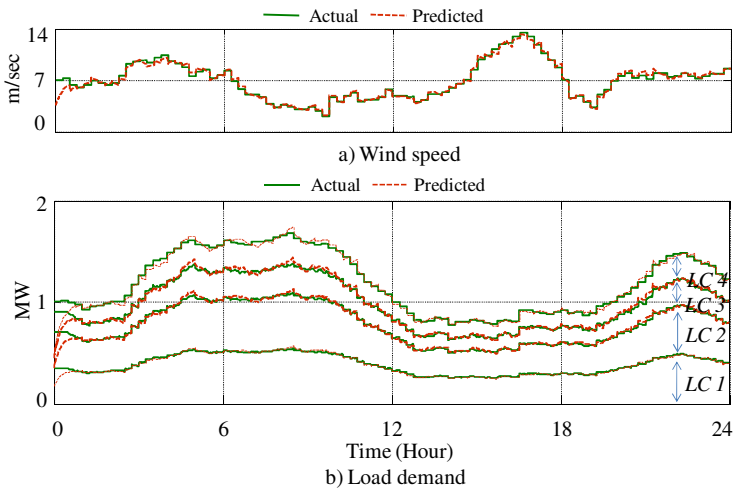

Fig. 6.7. Wind and load profiles: a) wind and b) load demand.

The SOC of the battery for this case study is divided into four categories. A high level is considered if the SOC of the battery storage is between 90% and 95%. A medium level is considered if the SOC of the battery is between 80% and 90%. A low level is considered if the storage of the battery is between 75% and 80%. A very low level is considered if the storage of the battery is between 40% and 75%.

The hydrogen storage is divided into three categories. A high level of hydrogen storage is considered if the hydrogen pressure of the tank is between 0.7% and 0.9%. A medium level is considered if the hydrogen pressure of the tank is between 0.3% and 0.7%. A low level is considered if the hydrogen pressure of the tank is between 0.1% and 0.3%.

All loads shown in Fig. 6.7 (b) are divided into four categories. Type *LC4* is the load with the highest priority that constitutes about 25-30% of the total load. Type *LC3* is a high priority load that constitute about 25-30% of the total load. Type *LC2* is the load with a medium priority that constitutes about 25-30% of the total load. Type *LC1* has the lowest priority.

6.3.1 Case A – System performance under high hydrogen and high battery storage conditions

In this case study, the hydrogen pressure is assumed at 0.9 pu and the SOC of the battery storage is assumed 94%. The response of the system is shown in Fig. 6.8.

Fig 6.8(a) shows the power from the wind turbine. Figs 6.8(b) and 6.8(c) show the power from the electrolyzer/fuel cell and hydrogen storage status, respectively. Figs 6.8(d) and 6.8(e) depict the power from battery storage and status of SOC, respectively. Fig. 6.8(f) shows the power generation of the diesel generator, and Fig. 6.8(g) shows the connected load.

From Fig. 6.8(a), it is seen that the wind turbine cannot extract any power from 7:00 hours to 15:00 hours due to low wind conditions. During this period, the system relies solely on the energy storage and diesel generator. From Figs 6.8(b) and 6.8(c), it is evident that the hydrogen storage runs out at 10:54 hours. During this condition, the load demand is provided by the battery storage and diesel generator. Wind returns at 15:00 hours and the diesel generator is disconnected from the system, as power from the wind and energy storage is sufficient to meet load demand. Under these conditions, the load curtailment operation is not required.

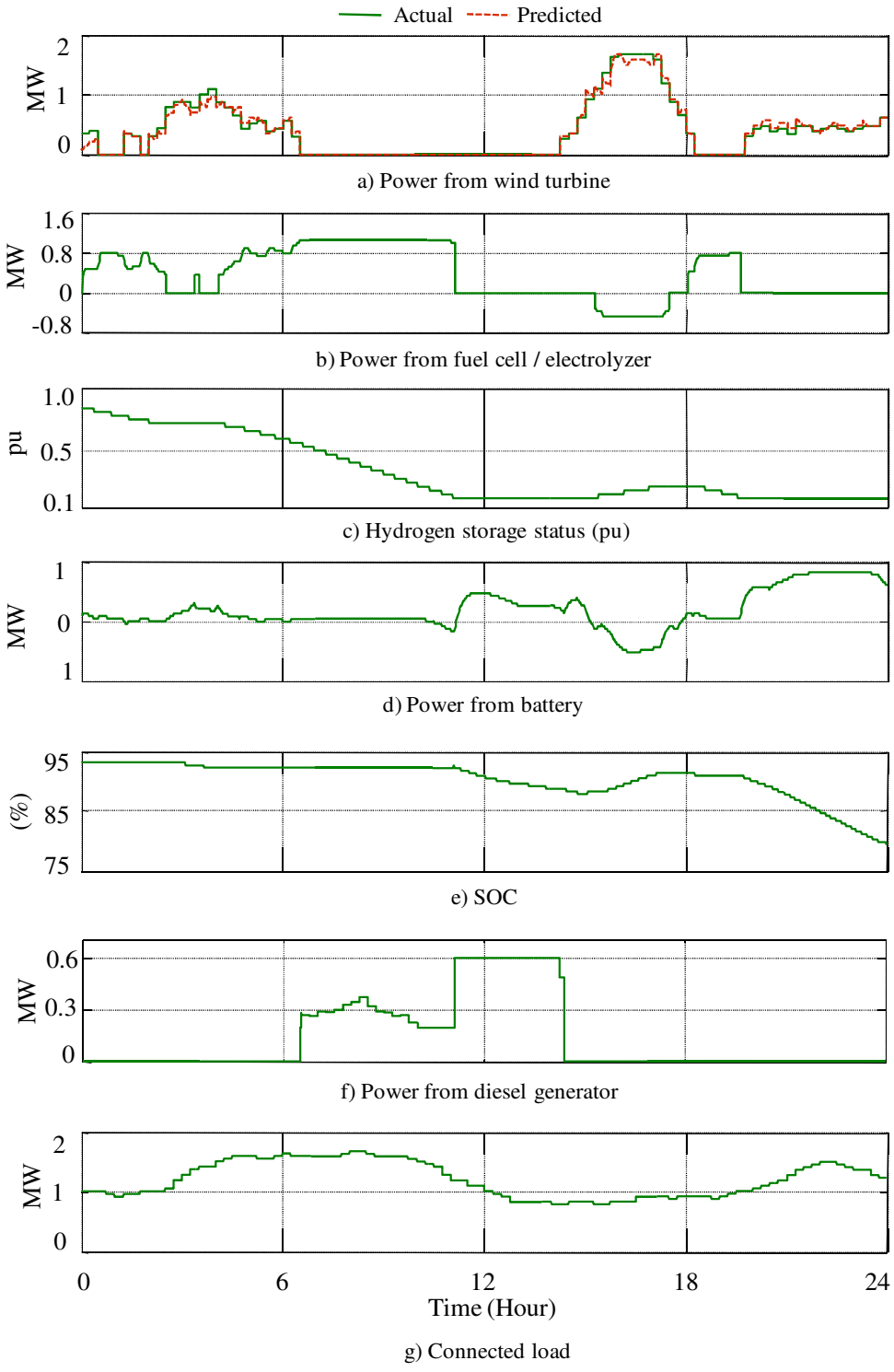

Fig. 6.8. Hybrid system operation under high hydrogen and high battery storage.

6.3.2 Case B – System performance under high hydrogen and low battery storage conditions

In this case study, the initial hydrogen pressure is assumed at 0.9 pu and the initial SOC of the battery storage is assumed 77%. The response of the system is shown in Fig. 6.9.

Fig 6.9(a) shows the power from the wind turbine. Figs 6.9(b) and 6.9(c) depict the power from the electrolyzer/fuel cell and the hydrogen storage status, respectfully. Figs 6.9(d) and 6.9(e) show the power from battery storage and the status of SOC, respectfully. Fig. 6.9(f) shows the power generation of the diesel generator, and Fig. 6.9(g) shows the connected load.

Here, the battery cannot provide any power as the SOC of the battery storage is considered low (77%). As a result, the system relies on the fuel cell and diesel generator when wind power falls below load demand. From Fig. 6.9(a), it is evident that the wind turbine cannot extract any power between 7:00 hours and 15:00 hours due to low wind conditions. As a result, the hybrid system must connect the diesel generator at 7:00 hours to meet the load demand.

Figs 6.9(b) and 6.9(c), reveal that the hydrogen storage runs out at 10:54 hours. As a result, the diesel generator only supplies the load demand from 10:54 hour to 15:00 hours. During this condition, the EMPRS curtails only load type *LC 4* as shown in Fig. 6.8(f) to avoid any system black-out. However, when wind returns at 15:00 hours, the hybrid system can provide power to all loads. In this particular case, the diesel generator is disconnected from the system at 16:50 hours when the wind turbine, battery and fuel cell can meet the load demand.

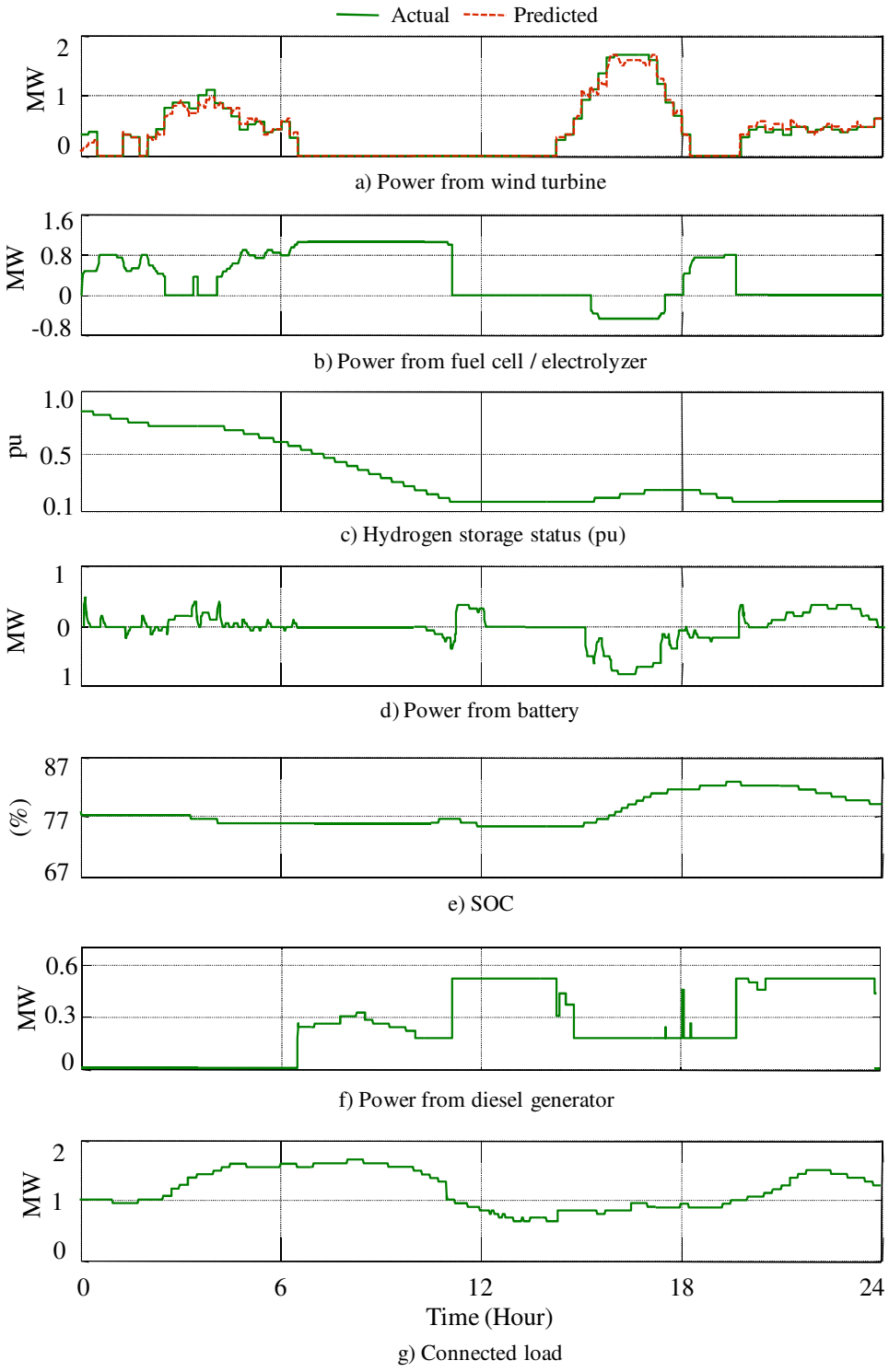

Fig. 6.9. Hybrid system operation under high hydrogen and low battery storage.

6.3.3 Case C – System performance under low hydrogen and high battery storage conditions

In this case study, the hydrogen pressure is assumed at 0.2 pu and the SOC of the battery storage is assumed 90%. The response of the system is shown in Fig. 6.10.

Fig 6.10(a) shows the power from wind turbine. Figs 6.10(b) and 6.10(c) show the power from the electrolyzer/fuel cell and hydrogen storage status, respectively. Figs 6.10(d) and 6.10(e) show the power from battery storage and the status of SOC, respectively. Fig. 6.10(f) shows power generation from the diesel generator. Fig. 6.10(g) shows the connected load.

From Figs 6.10(b) and 6.10 (c), it is seen that the hybrid system runs out of hydrogen at 1.5 hours. Fig. 6.10(a) indicates that the wind turbine system cannot extract any power from 7:00 hours to 15:00 hours owing to low wind conditions. During this time, the system is solely reliant on the battery storage and diesel generator. From Fig. 6.10(f), the diesel generator is connected to the system at 7:00 hours when power from the wind is not available. From Fig. 6.10(c), it is also seen that the SOC of the battery storage is too low to provide any power to the hybrid system at 08:15 hours. As a result, the hybrid system must rely soley on diesel generation. As power from the wind turbine and fuel cell and battery storage system is not available, the hybrid system must shut down certain loads between 8:15 hours and 15:00 hours. From Fig. 6.10(g), it is seen that the system curtails load types *LC 4* and *LC 3* from 08:15 hours to 15:00 hours. When wind returns at 15:00 hours, the load types *LC 4* and *LC 3* are reconnected to the system. However, at 18:30 hours the wind disappears. In this situation, the fuel cell, battery storage and diesel generator provides power without any load curtailment as shown in Figs 6.10(a) – 6.10(g).

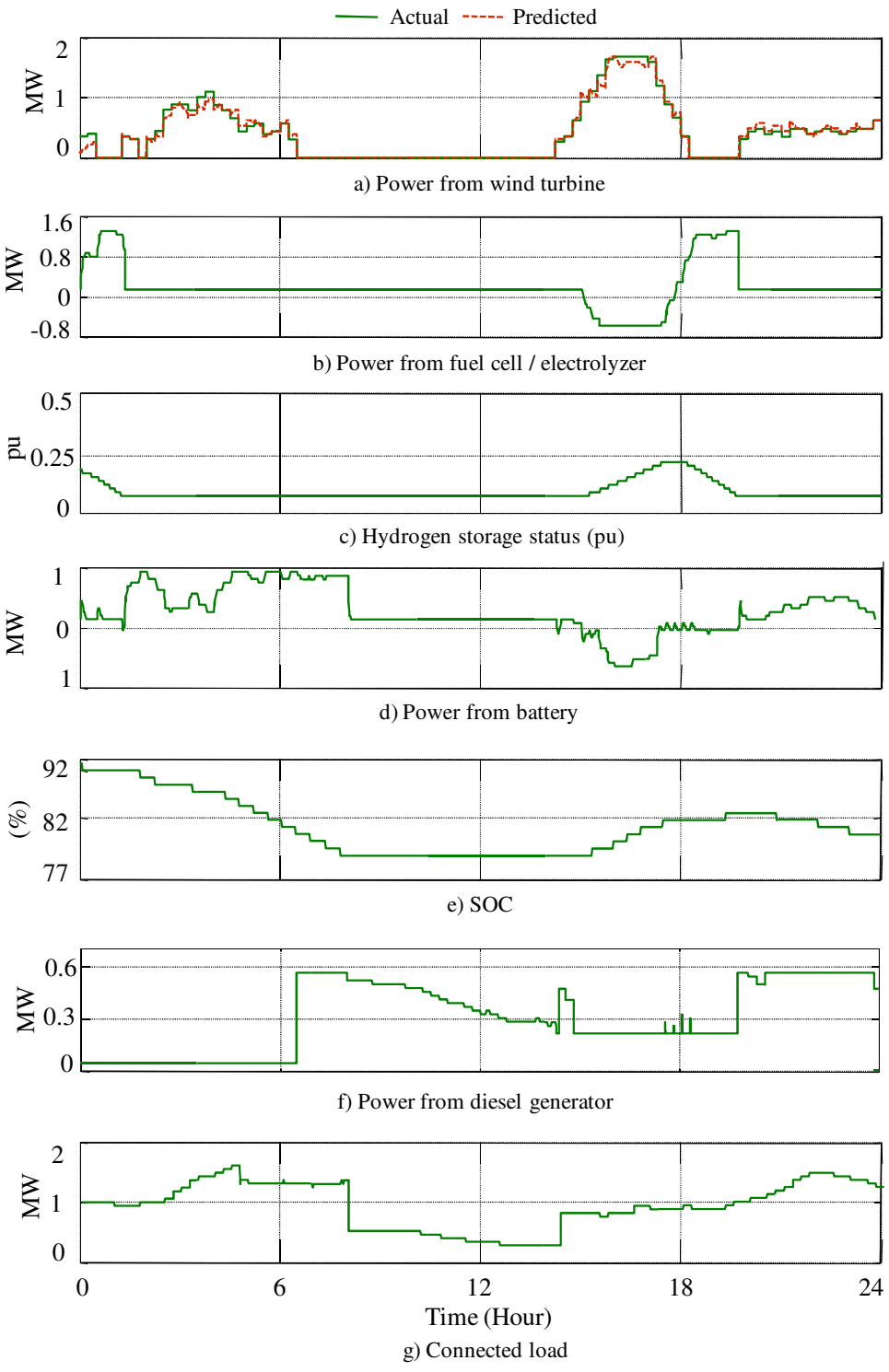

Fig. 6.10. Hybrid system operation under low hydrogen and high battery storage.

6.3.4. Case D – System performance under medium hydrogen and medium battery storage conditions

In this case study, the hydrogen pressure is assumed at 0.5 pu and the SOC of the battery storage is assumed 85%. The response of the system is shown in Fig. 6.11.

Fig 6.11(a) shows the power from the wind turbine. Figs 6.11(b) and 6.11(c) show the power from the electrolyzer/fuel cell and hydrogen storage status, respectively. Figs 6.11(d) and 6.11(e) show the power from battery storage and the status of SOC, respectfully. Fig. 6.11(f) shows the power generation from the diesel generator. Fig. 6.11(g) shows the connected load.

From Fig. 6.11(a), it is seen that the wind turbine system cannot extract any power from 7:00 hours to 15:00 hours due to low wind conditions. During this period, the system only relies solely on the battery storage, fuel cell and diesel generator. From Fig. 6.10(f), it is seen that the diesel generator is connected to the system at 7:00 hours when wind power is not available.

It is also seen from Figs 6.11(b) and 6.11 (c) that the fuel cell cannot provide any power as the hybrid system runs out of hydrogen at 7.5 hours. From Fig. 6.10(c), it is also seen that the SOC of the battery storage is too low to provide any power to the hybrid system at 09:00 hours. As a result, the hybrid system is solely reliant on diesel generation.

Fig. 6.11(g) shows that the hybrid system has shut down a) load type *LC4* at 07:30 hours, b) load type LC4 and LC 3 at 09:15 hours. When wind returns to the system at 15:00 hours, the load type *LC 4* and *LC 3* are reconnected to the system. However, at 18:30 hours, the wind disappears again. In this condition, the fuel cell, battery storage and diesel generator provide power without any load curtailment as shown in Figs 6.11(a) – 6.11(g).

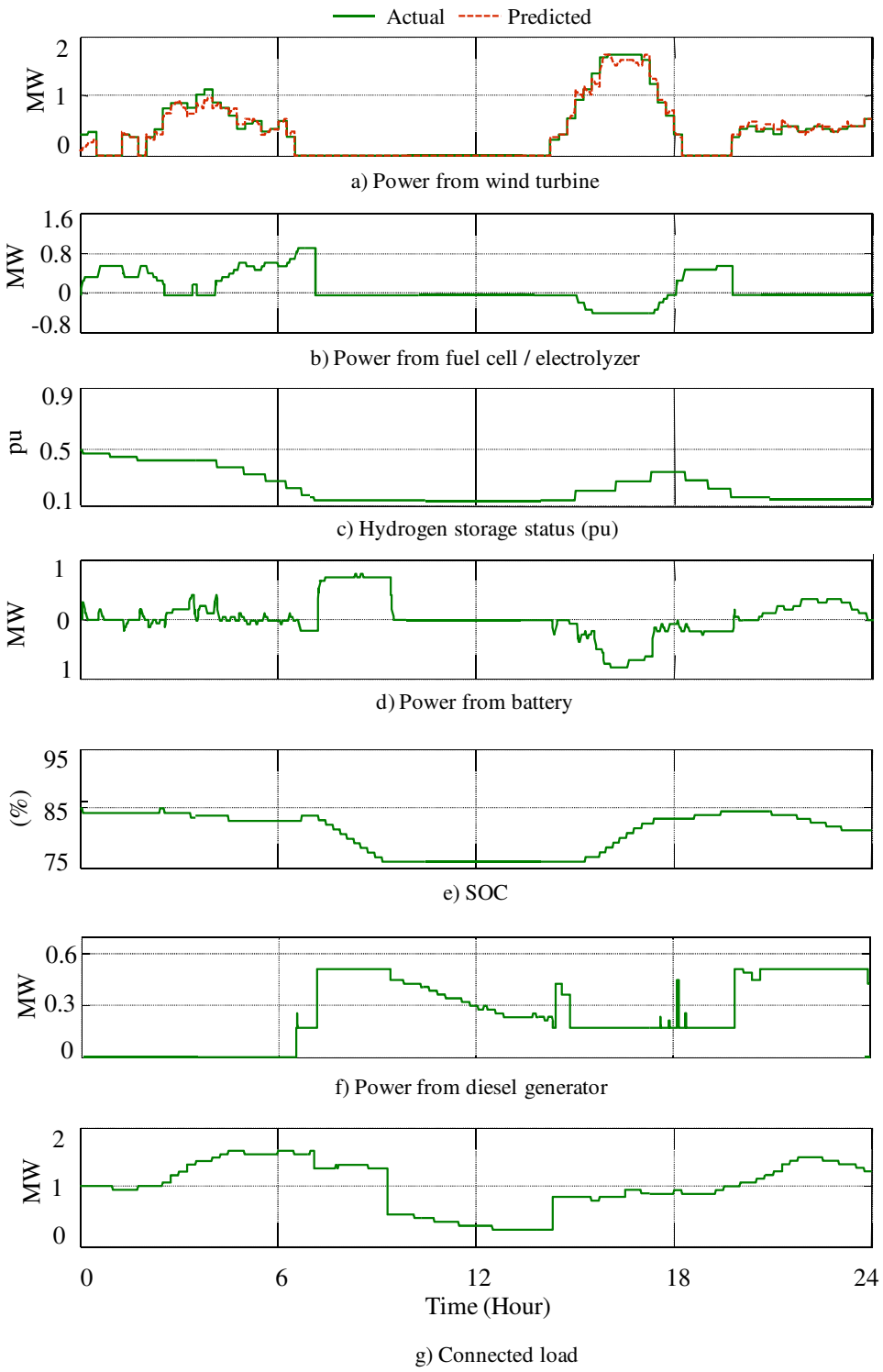

Fig. 6.11. Hybrid system operation under medium hydrogen and medium battery storage.

6.3.5 Case E – System performance under low hydrogen and very low battery storage conditions (emergency operation)

In this case study, the hydrogen pressure is assumed at 0.1 pu and the SOC of the battery storage is assumed 45%. The response of the system is shown in Fig. 6.12.

Fig 6.12(a) shows the power from wind turbine. Figs 6.12(b) and 6.12(c) show the power from electrolyzer/fuel cell and hydrogen storage status, respectfully. Figs 6.12(d) and 6.12(d) show the power from battery storage and the status of SOC, respectfully. Fig. 6.12(f) shows the power generation from the diesel generator. Fig. 6.12(g) shows the connected load.

As the system runs on a very low battery storage and low hydrogen storage, the system has to run on emergency mode. As a result, the hybrid system has to connect diesel generator at 00:00 hour as seen in Fig. 6.12(f), As the system runs on emergency mode the only emergency load type *LC 1* is connected. During this time, the diesel generator is used to provide power. However, the diesel generator has to run at its 30% of its rated power. As a result, the battery storage system consumes extra power when the emergency load demand is lower than the minimum power of diesel generator.

From Fig. 6.12(a), it is seen that the wind comes back at 15:00 hours. During this period, diesel generator is disconnected as wind turbine can provide the load demand. However, at 19:00 hours when the wind disappears, the diesel generator is again connected.

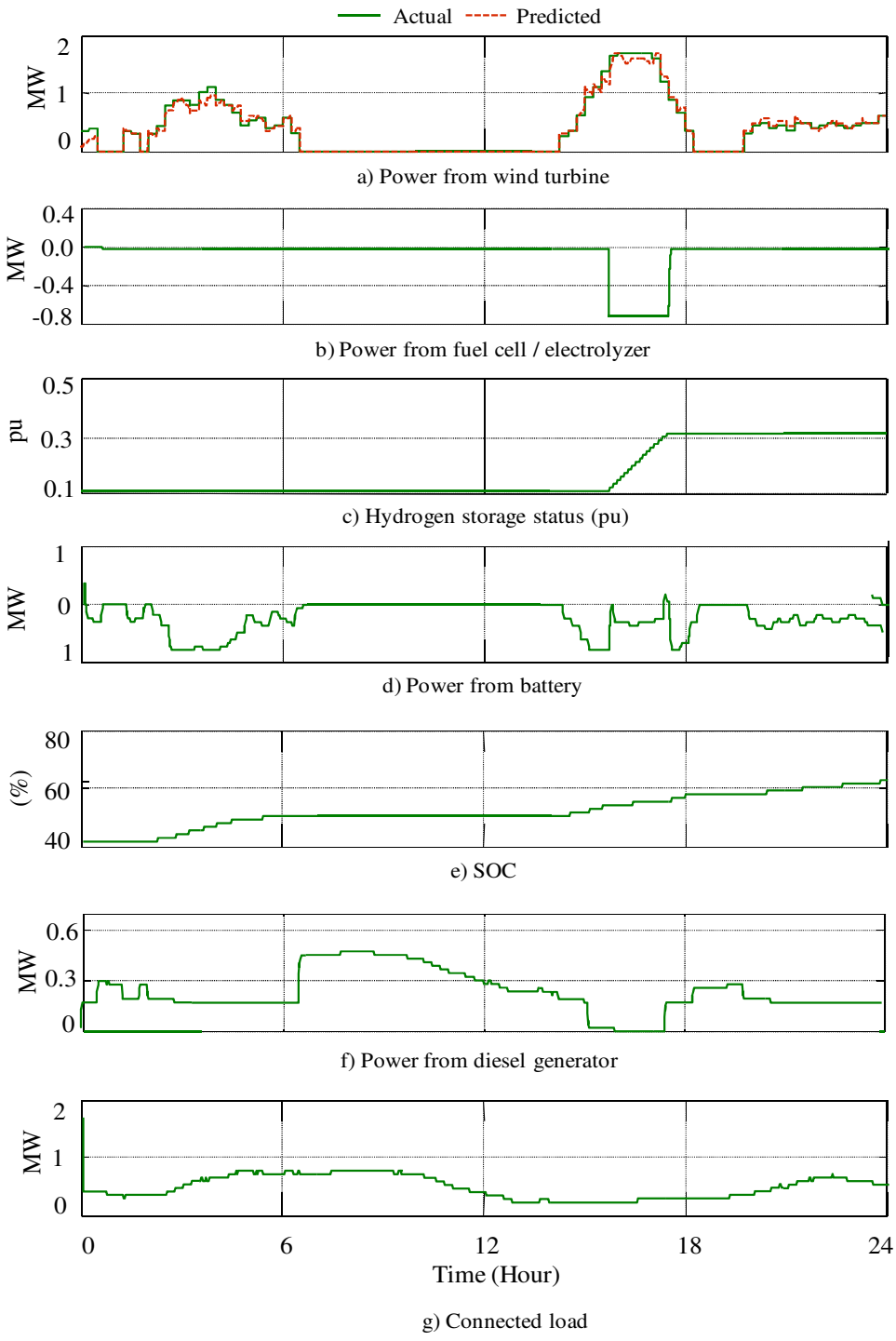

Fig. 6.12. Hybrid system operation under low hydrogen and very low battery storage (emergency operation condition).

Conclusion

In this chapter, several case studies are presented to evaluate the performance of the proposed system during the busy Easter period for different conditions of the battery and hydrogen storage under varying wind and load conditions. In these case studies, the wind profile is chosen such that a no wind condition occurs during the peak load. Several different cases of SOC of battery storage and hydrogen storage are considered. From these case studies, it is found that the proposed system can meet the load demand if the status of the SOC of battery storage and the hydrogen storage is high. However, for other conditions, the hybrid system has to curtail loads in order to avoid system black-out. An emergency operation condition is also shown in the case study when the SOC of the battery storage is very low (below 75%) and hydrogen storage is low. From Fig. 6.12, the proposed system is able to support only emergency loads for 24 hours. From the case studies, it is also revealed that the hybrid system can avoid system black-outs and is able to supply the emergency loads.

The proposed system is design to operate even in the worst case scenario. Of course, power supply cannot be maintained for all the customers all the time, but all essential customers will receive the required power under any worst case scenario. This is the main advantage of the proposed system

Conclusions

This thesis proposes a control and overall coordination of a hybrid stand-alone power system. The system comprises of a wind turbine, fuel cell, electrolyzer, battery storage, diesel generator and a set of loads. The overall control strategy of the hybrid system is based on a two-level structure. The top level is the energy management and power regulation system. Depending on wind and load conditions, this system generates reference dynamic operating points to low level individual sub-systems. The energy management and power regulation system also controls the load scheduling operation during unfavorable wind conditions with inadequate energy storage in order to avoid a system black-out. Based on the reference dynamic operating points of the individual sub-systems, the local controllers control the wind turbine, fuel cell, electrolyzer and battery storage units. The proposed control system is implemented in MATLAB Simpower software and tested for various wind and load conditions. Results are presented and discussed.

The major achievements of the thesis are summarized as follows:

- Optimum power extraction from varying wind – The optimum power extraction algorithm is proposed by controlling the rotor speed of the wind turbine. The novelty of the optimum power extraction algorithm is that it can ensure highly efficient operation of the PMSG at various wind and rotor speeds. Efficient operation is ensured by regulating the *d*- and *q*-axes current components of the PMSG.

- Hydrogen storage system modelling and control –The hydrogen storage system consists of fuel cell, electrolyzer and hydrogen tank. It is used in the project to support a load leveling application. In this project, power flow of the fuel cell and electrolyzer are regulated by a boost control and buck controller, respectively.

- Battery storage system modelling and control – The battery storage system is mainly used in the project to improve transient stability of the system in the event of wind and load changes. The power flow of the battery storage system is controlled by using a bi-directional dc-dc converter.

- Inverter control – Due to constant changes of wind and load speed, the inverter has to control the output voltage and frequency of the system. A three phase PWM controlled inverter is used to control the output voltage and frequency of the inverter.

- Dual-fuel diesel-hydrogen generator modelling and control – The modelling of the governor and excitation systems of the diesel generator is developed using a mathematical model. The adaptive neuro fuzzy inference system (ANFIS) is used to develop dual-fuel diesel-hydrogen generator model, due to its non-linear and time-varying nature. The frequency responses of the proposed model for different diesel hydrogen mixtures are developed and verified using real time data.

- Energy management and power regulation system –The overall coordination of the wind turbine, fuel cell, battery storage system, electrolyzer, diesel generator and loads is enacted by an energy management and power regulation system. Based on the actual wind and load profile and the status of energy storage, the energy management and power regulation system generates the appropriate dynamic reference signal to each individual controller. Moreover, it also controls the load curtailment operation. The obvious advantage of the EMPRS is its ability to prevent system black-outs in the event of low wind conditions or inadequate energy reserves.

Finally, application of the proposed system is investigated via several case studies for real wind and load conditions under different status of a) SOC of the battery storage system and b) hydrogen storage system. The wind profile is chosen such that a no wind

condition occurs for a relatively long period during peak load conditions. The load profile is considered during a busy season when the load demand is higher than the average seasons. From the case studies, it was demonstrated that this energy management and power regulation system can ensure continuous system operation free of black-outs.

The followings can be undertaken as future work of the projects:

(a) Verification of performance of the proposed system: Experimental set-up of a small wind generator and PEM fuel cell should be implemented to verify the performance of the proposed controllers.

(b) Power quality issues: Power quality issues should also be investigated in wind and hydrogen storage based hybrid power system.

(c) Low frequency emitted from wind generator and its impact on rural population should be investigated.

(d) Various types of wind turbine with different generation units should be compared.

List of References

[1] B. Singh, and J. Solanki, "Load Compensation for Diesel Generator-Based Isolated Generation System Employing DSTATCOM " *IEEE Transaction on Industry Application,* vol. 47, no. 1, pp. 238-244, January/February, 2011.

[2] R. J. Best, D. J. Morrow, D. J. McGowan, and P. A. Crossley, "Synchronous Islanded Operation of a Diesel Generator" *IEEE Transaction on Power Systems,* vol. 22, no. 4, pp. 2170-2176, November, 2007.

[3] Australian Institute of Petroleum bi-annual report, "Downstream Petroleum 2011" published in 2011. Web address: http://www.aip.com.au/pdf/Downstream_Petroleum_2011_Report.pdf

[4] http://www.cumminspower.com/www/literature/technicalpapers/PT-7004-Maintenance-en.pdf

[5] C. V. Nayar, High Renewable Energy Penetration Diesel Generator Systems, http://www.intechopen.com/articles/show/title/high-renewable-energy-penetration-diesel-generator-systems-.

[6] F. Katiraei, and C Abbey, "Diesel Plant Sizing and Performance Analysis of a Remote Wind-Diesel Microgrid" *IEEE Power Engineering Society General Meeting, Tampa, Florida, June 24- 28, 2007,* pp. 1-8.

[7] P. Saiyasitpanich, M. Lu, T. C. Keener, F. Liang, and S-J. Khang "The effect of diesel fuel sulfur content on particulate matter emissions for a nonroad diesel generator. *Journal of the Air & Waste Management Association, Volume 55, Issue 7, Pages 993-998, Jul 2005.*

[8] J. P. Barton and D. G. Infield, "Energy storage and its use with intermittent renewable energy", *IEEE Transactions on Energy Conversion, vol. 19 , no. 2, June 2004, pp: 441 – 448.*

[9] D. Anderson and M Leach, "Harvesting and redistributing renewable energy: on the role of gas and electricity grids to overcome intermittency through the generation and storage of hydrogen" *Journal on Energy Policy, Vol. 32 pp: 1603–1614, 2004.*

[10] P. Moriarty and D. Honnery, "Intermittent renewable energy: The only future source of hydrogen?", *International Journal of Hydrogen Energy Vol 32, pp. 1616 – 1624, 2007.*

[11] M.B. Blarke and H. Lund, "The effectiveness of storage and relocation options in renewable energy systems", *Journal of Renewable Energy, Vol. 33 pp. 1499–1507, 2008.*

[12] M. Datta, T. Senjyu, A. Yona, T. Funabashi, and C-H. Kim, "A Coordinated Control Method for Leveling PV Output Power Fluctuations of PV–Diesel Hybrid Systems Connected to Isolated Power Utility" *IEEE Transaction on Energy Conversion,* vol. 20, no. 1, March, 2009, pp. 153-162.

[13] J. Frunt, W. L. Kling, "Mitigation of wind power fluctuations in smart grids", *IEEE PES Innovative Smart Grid Technologies Conference Europe (ISGT Europe), Gothenburg, Germary, October 11-13,* pp. 1-8.

[14] Y. Ozaki, M. Miyatake, D. Iwaki, "Power control of a stand-alone photovoltaic/ wind/ energy storage hybrid generation system with Maximum Power Point Tracker", *International conference on Electrical Machines and Systems (ICEMS), Incheon, South Korea, October 10 – 13, pp 607 -611.*

[15] L. Jin, S. Yuan-Zhang, P. Sørensen, L. Guo-Jie, and G. Weng-Zhong, "Method for Assessing Grid Frequency Deviation Due to Wind Power Fluctuation Based on "Time-Frequency Transformation"", *IEEE Transaction on Sustainable Energy,* vol. 3, no. 1, pp. 65-73, January, 2012.

[16] M. L. Rahman, S. Oka, and Y. Shirai, "Hybrid Power Generation System Using Offshore-Wind Turbine and Tidal Turbine for Power Fluctuation Compensation (HOT-PC)", *IEEE Transaction on Sustainable Energy,* vol. 1, no. 2, pp. 92-98, July, 2010.

[17] G. Liu, W. Yu and Z. Tu, "Power Management for Alleviation of the Impact on PEM Fuel Cell due to Load Fluctuation", *Sixth International Conference on Intelligent Systems Design and Applications, Jinan, China, 16-18 Oct. 2006, Vol. 1,* pp: 1104 – 1110.

[18] H. Asano, and S. Bando, "Load Fluctuation Analysis of Commercial and Residential Customers for Operation Planning of a Hybrid Photovoltaic and Cogeneration System", *IEEE Power Engineering Society General Meeting, Montreal, Quebec, Canada, October 16-20, 2006, pp. 1-6.*

[19] E. Muljadi, and H. E. McKenna, "Power Quality Issues in a Hybrid Power System", " *IEEE Transaction on Industry Application,* vol. 38, no. 3, pp. 803-809, May/June, 2002.

[20] R. I. Bojoi, L. R. Limongi, D. Roiu, and A. Tenconi, "Enhanced Power Quality Control Strategy for Single-Phase Inverters in Distributed Generation Systems", *IEEE Transaction on power electronics,* vol. 26, no. 3, March, 2011, pp. 798-806.

[21] C. Han, A. Q. Huang, M. E. Baran, S. Bhattacharya, W. Litzenberger, L. Anderson, A. L. Johnson, and A-A. Edris, "STATCOM Impact Study on the Integration of a Large Wind Farm into a Weak Loop Power System", *IEEE Transaction on energy conversion,* vol. 26, no. 1, March 2008, pp. 226- 233.

[22] I. Wasiak, M. C. Thoma, C. E. T. Foote, R. Mienski, R. Pawelek, P. Gburczyk, and G. M. Burt, "A Power-Quality Management Algorithm for Low-Voltage Grids With Distributed Resources" *IEEE Transaction on power delivery,* vol. 23, no. 2, April, 2008, pp. 1055-1062,.

[23] M. Singh, V. Khadkikar, , A. Chandra, and R. K. Varma, "Grid Interconnection of Renewable Energy Sources at the Distribution Level With Power-Quality Improvement Features", *IEEE Transaction on power delivery,* vol. 26, no. 1, January, 2011, pp. 307- 315.

[24] H. Nian, R. Zeng "Improved control strategy for stand-alone distributed generation system under unbalanced and non-linear loads", *IET Renewable Power Generation,* vol. 5, no. 5, pp 323-331, 2011.

[25] N. Gyawali, and Y Ohsawa, "Integrating Fuel Cell/Electrolyzer/ Ultracapacitor System Into a Stand-Alone Microhydro Plant", *IEEE Transaction on Energy Conversion,* vol. 25, no. 4, December 2010, pp. 1092-1104.

[26] C. Wang, and M. H. Nehrir, "Power Management of a Stand-Alone Wind/Photovoltaic/Fuel Cell Energy System", *IEEE Transaction on Energy Conversion,* vol. 23, no. 3, September 2008, pp. 957-967.

[27] A. Hajizadeh, M. A. Golkar, and A. Feliachi, "Voltage Control and active Power Management of Hybrid Fuel-Cell/Energy-Storage Power Conversion System Under Unbalanced Voltage Sag Conditions", *IEEE Transaction on Energy Conversion*, vol 25, no. 4, December 2010, pp. 1195-1208.

[28] S. D. G. Jayasinghe, D. M. Vilathgamuwa, and U. K. Madawala, "Direct Integration of Battery Energy Storage Systems in Distributed Power Generation" *IEEE Transaction on Energy Conversion*, vol 26, no. 2, June 2011, pp. 977-685.

[29] C. Wang, M. Nehrir, and S. R. Shaw, "Dynamic Models and Model Validation for PEM Fuel Cells Using Electrical Circuits" *IEEE Transaction on Energy Conversion,* vol 20, No. 2, June 2005, pp. 442-451.

[30] P. Garcia, L. M. Fernandez, C. A. Garcia, and F. Jurado, "Energy Management System of Fuel-Cell-Battery Hybrid Tramway" *IEEE Transaction on Industrial Electronics*, vol. 57, no. 12, December 2010, pp. 4013-4023.

[31] T. Zhou, B. Francois, M. el H. Lebbal, and S. Lecoeuche, "Real-Time Emulation of a Hydrogen-Production Process for Assessment of an Active Wind-Energy Conversion System" *IEEE Transaction on Industrial Electronics,* vol. 56, no. 3, April 2009, pp. 737-746.

[32] K. L. Wang and P. Kundur, "Power system security assessment", *IEEE Power and Energy Magazine*, vol. 2 , No. 5, September/ October, 2004, pp. 30 – 39.

[33] J. A. Greatbanks, D. H. Popovic, M. Begovic, A. Pregelj, T. C. Green, "On optimization for security and reliability of power systems with distributed generation", *IEEE Power Tech Conference Proceedings,* Bologna, Italy, 23-26 June, 2003.

[34] C. W. Gellings, W. M. Smith, "Integrating demand-side management into utility planning", *IEEE proceedings,* vol. 77, No. 6, June 1989, pp. 908-918.

[35] G. Strbac, "Demand side management: Benefits and challenges ", *Journal on Energy Policy* ,vol. 36, no. 12, December 2008, pp: 4419–4426.

[36] H. L. Wills, H. N. Tram and G. B. Rackliffe "Short-range load forecasting for distribution system planning-an improved method for extrapolating feeder load growth ", *IEEE Transaction on Power Systems*, vol. 7, no. 3, August 1992, pp. 1306-1312.

[37] I. Ziari, G. Ledwich, A. Ghosh, and G. Platt, "Integrated Distribution Systems Planning to Improve Reliability Under Load Growth", *IEEE Transaction on Power Delivery*, vol. 27, no. 2, April 2012, pp. 757-765.

[38] Z. A. Yamayee, H. Hakimmashhadi, "A Flexible Generation Planning Approach Recognizing Long Term Load Growth Uncertainty", *IEEE Power Engineering Review*, vol. 4, no. 8, August 1984.

[39] A. H. Shahirinia, S. M. M. Tafreshi, A. H. Gastaj, A. R. Moghaddomjoo, "Optimal sizing of hybrid power system using genetic algorithm", *2005 International Conference on Future Power Systems*, Amsterdam, Netherland,vol. 6, Novermber, 2005, pp: 1-6.

[40] B. S. Borowy, Z. M. Salameh, "Methodology for optimally sizing the combination of a battery bank and PV array in a wind/PV hybrid system", *IEEE Transaction on Energy Conversion*, vol. 11, no. 2, June, 1996, pp. 367-375.

[41] W.D. Kellogg, M.H. Nehrir, G. Venkataramanan, and V. Gerez, "Generation Unit Sizing and Cost Analysis for Stand-Alone Wind, Photovoltaic, and Hybrid Wind PV Systems", *IEEE Transaction on Energy Conversion*, pp. 70-75, vol. 13, no. 1, March 1998.

[42] A. A. Setiawan, Y. Zhao, and C. V. Nayar, "Design, economic analysis and environmental considerations of mini-grid hybrid power system with reverse osmosis desalination plant for remote areas", *Journal on Renewable Energy,* vol. 34, 2009, Pages 374–383.

[43] S. Diaf, M. Belhamel, M. Haddadi, A. Louche, "Technical and economic assessment of hybrid photovoltaic/wind system with battery storage in Corsica island", *Journal on Energy Policy*, vol. 36, 2008, pp: 743–754.

[44] D. B. Das, C. Patvardhan, "Solution of Economic Load Dispatch using real coded Hybrid Stochastic Search", *International Journal of Electrical Power & Energy Systems*, pp 165−170, vol. 21, no. 3, March 1999,

[45] J. Samaniego, F. Alija, S. Sanz, C. Valmaseda and F. Frechoso, "Economic and technical analysis of a hybrid wind fuel cell energy system", *Journal on Renewable Energy Review*, vol. 33, pp: 839 - 845, 2008.

[46] M. El Mnassri, M.; A. S. Leger; "Stand alone photovoltaic solar power generation system: A case study for a remote location in Tunisia" *IEEE Power and Energy Society General Meeting*, Minneapolis, 25-29 July 2010, pages 1-4.

[47] P. Hearps, D. McConnell, "Renewable Energy Technology Cost Review", Melbourne Energy Institure, March 2011.

[48] B. Singh, and J. Solanki, "Load Compensation for Diesel Generator-Based Isolated Generation System Employing DSTATCOM " *IEEE Transaction on Industry Application*, vol. 47, no. 1, pp. 238-244, January/February, 2011.

[49] R. J. Best, D. J. Morrow, D. J. McGowan, and P. A. Crossley, "Synchronous Islanded Operation of a Diesel Generator" *IEEE Transaction on Power Systems*, vol. 22, no. 4, pp. 2170-2176, November, 2007.

[50] A. Roy, S. B. Kedare, and S. Bandyopadhyay, "Optimum sizing of wind-battery systems incorporating resource uncertainty," *Applied Energy*, vol. 87, no. 8, pp. 2712–2727, 2010.

[51] C. Wang and M. H. Nehrir, "Load transient mitigation for stand-alone fuel cell power generation systems," *IEEE Transaction Energy Conversion.*, vol. 22, no. 4, pp. 864–872, December 2007.

[52] P. Thounthong, S. Rael, and B. Davat, "Analysis of supercapacitor as second source based on fuel cell power generation," *IEEE Transaction Energy Conversion.*, vol. 24, no. 1, pp. 247–255, March 2009.

[53] P. K. Goel, B. Singh, S. S. Murthy, and N. Kishore "Isolated Wind–Hydro Hybrid System Using Cage Generators and Battery Storage" *IEEE Transaction on Industrial Electronics*, vol. 58, no. 4, April 2011, pp. 1141-1153.

[54] T. Zhou and B. François "Energy Management and Power Control of a Hybrid Active Wind Generator for Distributed Power Generation and Grid Integration" *IEEE Transaction on Industrial Electronics,* vol. 58, no. 1, January 2011, pp. 95-104.

[55] N. Gyawali, and Y Ohsawa, "Integrating Fuel Cell/Electrolyzer/ Ultracapacitor System Into a Stand-Alone Microhydro Plant", *IEEE Transaction on Energy Conversion*, vol. 25, no. 4, pp. 1092-1104, December 2010.

[56] C. Wang, and M. H. Nehrir, "Power Management of a Stand-Alone Wind/Photovoltaic/Fuel Cell Energy System", *IEEE Transaction on Energy Conversion,* vol. 23, no. 3, pp. 957-967, September 2008.

[57] A. Hajizadeh, M. A. Golkar, and A. Feliachi, "Voltage Control and active Power Management of Hybrid Fuel-Cell/Energy-Storage Power Conversion System Under Unbalanced Voltage Sag

Conditions", *IEEE Transaction on Energy Conversion,* vol. 25, No. 4, pp. 1195-1208, December 2010.

[58] S. D. G. Jayasinghe, D. M. Vilathgamuwa, and U. K. Madawala, "Direct Integration of Battery Energy Storage Systems in Distributed Power Generation" *IEEE Transaction on Energy Conversion,* vol 26, No. 2, pp. 977-685, June 2011.

[59] C. Wang, M. Nehrir, and S. R. Shaw, "Dynamic Models and Model Validation for PEM Fuel Cells Using Electrical Circuits" *IEEE Transaction on Energy Conversion*, vol. 20, No. 2, pp. 442-451, June 2005.

[60] P. Garcia, L. M. Fernandez, C. A. Garcia, and F. Jurado, "Energy Management System of Fuel-Cell-Battery Hybrid Tramway" *IEEE Transaction on Industrial Electronics*, vol. 57, no. 12, pp. 4013-4023, December 2010.

[61] T. Zhou, B. Francois, M. el H. Lebbal, and S. Lecoeuche, "Real-Time Emulation of a Hydrogen-Production Process for Assessment of an Active Wind-Energy Conversion System" *IEEE Transaction on Industrial Electronics*, vol. 56, no. 3, April 2009, pp. 737-746.

[62] W. D. Kellogg, M. H. Nehrir, G. Venkataramanan, and V. Gerez, "Generation unit sizing and cost analysis for stand-alone wind, photovoltaic, and hybrid wind/PV systems," *IEEE Transaction on Energy Conversion*, vol. 13, no. 1, pp. 70–75, Mar. 1998.

[63] R. Chedid, H. Akiki, and S. Rahman, "A decision support technique for the design of hybrid solar-wind power systems," *IEEE Transaction on Energy Conversion*, vol. 13, no. 1, pp. 76–83, Mar. 1998.

[64] B. Borowy and Z. Salameh, "Methodology for the optimally sizing the combination of a battery bank and PV array in a wind/PV hybrid system," *IEEE Transaction on Energy Conversion.*, vol. 11, no. 2, pp. 367–375, Jun. 1996.

[65] F. Giraud and Z. M. Salameh, "Steady-state performance of a gridconnected rooftop hybrid wind-photovoltaic power system with battery storage," *IEEE Transaction on Energy Conversion*, vol. 16, no. 1, pp. 1–7, Mar. 2001.

[66] C. Marnay, G. Venkataramanan, M. Stadler, A. S. Siddiqui, R. Firestone, and B. Chandran, "Optimal technology selection and operation of commercial-building microgrids," *IEEE Transaction on Power Systems*, vol. 23, no. 3, pp. 975–982, Aug. 2008.

[67] R. Lasseter, A. Abbas, C.Marnay, J. Stevens, J. Dagle, R. Guttromson, A. S. Meliopoulos, R. Yinger, and J. Eto, Integration of Distributed Energy Resources: The CERTS Microgrid Concept California Energy Commission, P500-03-089F, Oct. 2003.

[68] R. H. Lasseter and P. Piagi, Control and Design of Microgrid Components: Final Project Report PSERC Publication 06–03, Jan. 2006.

[69] H. Louie and K. Strunz, "Superconducting magnetic energy storage (SMES) for energy cache control in modular distributed hydrogen-electric energy systems," *IEEE Transaction on Applied Superconductor*, vol. 17, no. 2, pp. 2361–2364, Jun. 2007.

[70] K. Agbossou, M. Kolhe, J. Hamelin, and T. K. Bose, "Performance of a stand-alone renewable energy system based on energy storage as hydrogen," *IEEE Transaction on Energy Conversion*, vol. 19, no. 3, pp. 633–640, Sep. 2004.

[71] K. Agbossou, R. Chahine, J. Hamelin, F. Laurencelle, A. Anourar, J.-M. St-Arnaud, and T. K. Bose, "Renewable energy systems based on hydrogen for remote applications," *Journal on Power Sources*, vol. 96, pp. 168–172, 2001.

[72] S.-H. Ko, S. R. Lee, H. Dehbonei, and C. V. Nayar, "Application of voltage- and current-controlled voltage source inverters for distributed generation systems," *IEEE Transaction on Energy Conversion*, vol. 21, no. 3, pp. 782–792, Sep. 2006.

[73] F.A. Farret and M.G. Simões, Integration of Alternative Sources of Energy. Hoboken, NJ: Wiley, 2006.

[74] M. H. Nehrir and C. Wang, Modeling and Control of Fuel Cells: Distributed Generation Applications. Piscataway, NJ: IEEE Press-Wiley, 2009, ch. 9.

[75] C. K. Sao and P. W. Lehn, "A transformer less energy storage system based on a cascade multilevel PWM converter with star configuration," *IEEE Transaction on Industry Application*, vol. 44, no. 5, pp. 1621–1630, Sep./Oct. 2008,

[76] L. H. Hansen, L. Helle, F. Blaabjerg, E. Ritchie, S. Munk-Nielsen, H. Bindner, P. Srensen, and B. Bak-Jensen, "Conceptual survey of generators and power electronics for wind turbines," Risø Nat. Lab., Roskilde, Denmark, Tech. Rep. Riso-R1205 (EN), Dec. 2001.

[77] G. Abad, M. A. Rodriguez, G. Iwanski, and J. Poza, "Direct power control of doubly-fed-induction-generator-based wind turbines under unbalanced grid voltage," *IEEE Transaction on Power Electronic*, vol. 25, no. 2, pp. 442–452, Feb. 2010.

[78] R. Peña, J. Clare, and G. Asher, "Doubly-fed induction generators using back-to-back PWM converters and its applications to variable-speed wind-energy generation," IEEE Proceedings on Electric Power Application, vol. 143, no. 3, pp. 231–241, May 1996.

[79] W. Leonhard, Control of Electrical Drives. Berlin, Germany: SpringerVerlag, 1997.

[80] S. Muller, M. Deicke, and R. W. De Doncker, "Doubly fed induction generator systems for wind turbines," *IEEE Industry Application Magazine*, vol. 8, no. 3, pp. 26–33, May 2002.

[81] K. Rothenhagen and F. W. Fuchs, "Doubly fed induction generator model-based sensor fault detection and control loop reconfiguration," *IEEE Transaction on Industry Electronics*, vol. 56, no. 10, pp. 4229–4238, Oct. 2009.

[82] M. Kayikci and J. V. Milanovic, "Reactive power control strategies for DFIG-based plants," *IEEE Transaction on Energy Conversion*, vol. 22, no. 2, pp. 389–396, Jun. 2007.

[83] B. Rabelo and W. Hofman, "Control of an optimized power flow in wind power plants with doubly-fed induction generators," *IEEE Power Electronics Specialist Conference, Acapulco, México, Jun. 2003,* pp. 1563–1568.

[84] B. Rabelo and W. Hofmann, "Power flow optimization and grid integration of wind turbines with the doubly-fed induction generator," *IEEE Power Electronics Specialist Conference, Recife, Brazil, 2005,* pp. 2930–2936.

[85] F. Iov, R. Teodorescu, F. Blaabjerg, B. Andersen, J. Birk, and J. Miranda, "Grid code compliance of grid-side converter in wind turbine systems," *IEEE Power Electronics Specialist Conference, Jun. 18–22, 2006*, pp. 1–7.

[86] Grid Code. High and Extra High Voltage, E.ON Netz, Bayreuth, Germany. [Online]. Available: www.eon-netz.com

[87] A. Yazdani, and R. Iravani, "A Neutral-Point Clamped Converter System for Direct-Drive Variable-Speed Wind Power Unit," *IEEE Transaction on Energy Conversion*, vol. 21, no. 2, pp. 596–607, Jun. 2006.

[88] H. Polinder, F. F. A. van der Pijl, G.-J. de Vilder, and P. Tavner, "Comparison of direct-drive and geared generator concepts for wind turbines," *IEEE International Conference. Electric Machine and Drives, May 15, 2005,* pp. 543–550.

[89] A. Ragheb and M. Ragheb, "Wind turbine gearbox technologies," *1st INREC, Mar. 21–24, 2010,* pp. 1–10.

[90] Wind Turbines and Wind Farms Database. accessed on Oct. 2010. [Online]. Available: http://www.thewindpower.net/turbines_list.php

[91] H. Li, Z. Chen, and H. Polinder, "Optimization of Multibrid permanentmagnet wind generator systems," *IEEE Transaction on Energy Conversion*, vol. 24, no. 1, pp. 82–92, Mar. 2009.

[92] R. A. Huggins, "Energy Storage" Springer-Verlag GmbH, July 2010

[93] California energy commission, "2020 Strategic Analysis of Energy Storage in California", November 2011.

[94] Nexight Group and Sandia National Laboratories, "Advanced Materials and Devices for Stationary Electrical Energy Storage Application" U. S. Department of Energy, December 2010.

[95] Electric Power Research Institute, "Electric Energy Storage Technology Option: A White Paper Primer on Applications, Cost and Benefits", Palo Alto, CA 1020676.

[96] Electricity Society Association (ESA), April 2011.
http://www.electricitystorage.org/ESA/technologies/pumped_hydro/

[97] J. N. Gordes, A. L. Weisbrich, D. L. Rainey, P. W. Olson, "Offshore WARP Wind Power and Integral H2-Gas Turbine or Fuel Cells" *The European Seminar on Offshore Wind Energy in Mediterranean and Other European Seas (OWEMES) conference, Syracusa, Sicily, Italy, April 2000.*

[98] H. Ibrahim, A. Ilinca, and J. Perron, "Energy Storage Systems - characteristics and comparisons," *Journal of Renewable and Sustainable Energy Reviews,* vol. 12, no. 5, pp. 1221-1250, June 2008.

[99] G. Weiss, Ed., Multiagent Systems: A Modern Approach to Distributed Artificial Intelligence. Cambridge, MA: MIT Press, 1999.

[100] H. M. Kelash, H. M. Faheem, and M. Amoon, "It takes a multiagent system to manage distributed systems," *IEEE Potentials*, vol. 26, no. 2, pp. 39–45, Mar./Apr. 2007.

[101] A. L. Dimeas and N. D. Hatziargyriou, "Operation of a multiagent system for microgrid control," IEEE Trans. Power Syst., vol. 20, no. 3, pp. 1447–1455, Aug. 2005.

[102] Z. Yang, C. Ma, J. Q. Feng, Q. H. Wu, S. Mann, and J. Fitch, "A multi-agent framework for power system automation," *International Journal on Innovation Energy System and Power*, vol. 1, no. 1, pp. 39–45, Nov. 2006.

[103] Z. Toroczckai and S. Eubank, "Agent-based modeling as a decisionmaking tool," The Bridge, Publication of the National Engineering Academy, vol. 35, no. 4, pp. 22–27, 2005, Winter.

[104] K. Huang, D. A. Cartes, and S. K. Srivastava, "A multiagent-based algorithm for ring-structured shipboard power system reconfiguration," *IEEE Transaction on System, Man, Cybernetics*, vol. 37, no. 5, pp. 1016–1021, Sep. 2007.

[105] T. Nagata and H. Sasaki, "A multi-agent approach to power system restoration," *IEEE Transaction on Power System*, vol. 17, no. 2, pp. 457–462, May 2002.

[106] M. E. Torres-Hernandez, "Hierarchical Control of Hybrid Power Systems," Ph.D. Dissertation, Univ. of Puerto Rico, Mayaguez, 2007.

[107] Z. Jiang and R. Dougal, "Hierarchical microgrid paradigm for integration of distributed energy resources," *IEEE Power Engineering Society General Meeting*, Pittsburgh, PA, Jul. 20–24, 2008.

[108] S. M. Schoenung, Long- vs. Short-Term Energy Storage Technologies Analysis: A Life-Cycle Cost Study: A Study for the DOE Energy Storage Sandia National Laboratories, Sandia Rep. SAND2003-2783, Aug. 2003.

[109] M. Coleman, W. G. Hurley, and C. K. Lee, "An improved battery characterization method using a two-pulse load test," *IEEE Transaction on Energy Conversion*, vol. 23, no. 2, pp. 708–713, Jun. 2008.

[110] G. Plett, "Extended Kalman filtering for battery management systems of LiPB-based HEV battery packs. Part 3. State and parameter estimation," *Journal on Power Sources*, vol. 134, no. 2, pp. 277–292, 2004.

[111] S. Rodrigues, N. Munichandraiah, and A. Shukla, "A review of state-of-charge indication of batteries by means of ac impedance measurements," *Journal on Power Sources*, vol. 87, no. 1/2, pp. 12–20, 2000, 12.20.

[112] I. L.-S. Kim, "A technique for estimating the state of health of lithium batteries through a dual-sliding-mode observer," *IEEE Transaction on Power Electronics*, vol. 25, no. 4, pp. 1013–1022, Apr. 2010.

[113] C. R. Gould, C. M. Bingham, D. A. Stone, and P. Bentley, "New battery model and state-of-health determination through subspace parameter estimation and state-observer techniques," *IEEE Transaction on Vehicle Technology*, vol. 58, no. 8, pp. 3905–3916, Oct. 2009.

[114] J. P. Christophersen, "Battery State of Health Assessment Using Near Real-Time Impedance Measurement," Ph.D. Dissertation, Montana State Univ.-Bozeman, Bozeman, MT, 2011

[115] M. Yin, G. Li, M. Zhou and C. Zhao, "Modeling of the Wind Turbine with a Permanent Magnet Synchronous Generator for Integration" *IEEE Power Engineering Society General Meeting,* Tampa, Florida, *2007, 24-28 June 2007,* pp. 1-6.

[116] A. G. Abo-Khalil, D-C. Lee "Dynamic Modeling and Control of Wind Turbines for Grid-Connected Wind Generation System" *IEEE Power Electronics Specialists Conference 2006 (PESC '06), 18-22 June 2006,* pp. 1-6.

[117] L. Shi, C. Wang, L. Yao, Y. Ni, and M Bazargan "Optimal Power Flow Solution Incorporating Wind Power", *IEEE Systems Journal,* vol. 6, no. 2, pp. 233-241, June, 2012.

[118] K. Ohyama, T. Nakashima, "Wind turbine emulator using wind turbine model based on blade element momentum theory", *International Symposium on Power Electronics Electrical Drive Austromation and Motions (SPEEDAM),* 14-16 June 2010, pp. 762-765.

[119] Y. Lei, A. Mullane, G. Lightbody, and R. Yacamini, "Modeling of the Wind Turbine With a Doubly Fed Induction Generator for Grid Integration Studies", *IEEE transaction on Energy Convsion,* vol. 21, no. 1, pp. 257-264, Mar, 2006.

[120] C. Eisenhut, F. Krug, C. Schram, and B Klockl " Wind-Turbine Model for System Simulations Near Cut-In Wind Speed" *IEEE transaction on Energy Convsion,* vol. 22, no. 2, pp. 414-420, Jun, 2007.

[121] K. E. Johnson, L. Y. Pao, M. J. Balas, and L. J. Fingersh "Control of variable-speed wind turbines: standard and adaptive techniques for maximizing energy capture", *IEEE Control System Magazine,* vol. 26, no. 3, pp. 70-81, June 2006.

[122] P. C. Klause, O. Wesynczuk, and S. D. Sudhoff, "Analysis of Electric Machinary and Drive System" 2nd Edition, John Willey and Sons, Inc. Publication, ISBN: 0-471-14326-X.

[123] S. Li, T. A. Haskew, R. P. Swatloski and W. Gathings, "Optimal and Direct-Current Vector Control of Direct-Driven PMSG Wind Turbines", *IEEE transaction on Power Electronics*, vol. 27, no. 5, pp. 2325-2337, May, 2012.

[124] S. Zhang, K-J. Tseng, D. M. Vilathgamuwa, T. D. Nguyen, and X.-Y. Wang, " Design of a Robust Grid Interface System for PMSG-Based Wind Turbine Generators", *IEEE transaction on Industrial Electronics*, vol. 58, no. 1, pp. 316-328, January, 2011.

[125] H. Geng, G. Yang, D. Xu, and B. Wu, "Unified Power Control for PMSG-Based WECS Operating Under Different Grid Conditions", *IEEE transaction on Energy Conversion,* vol. 26, no. 3, pp. 822-830, September, 2011.

[126] J. Dai, D. Xu, and B. Wu, "A Novel Control Scheme for Current-Source Converter-Based PMSG Wind Energy Conversion Systems", *IEEE Transaction on Power Electronics,* vol. 24, no. 4, 2009, pp. 1-10.

[127] S. Morimoto, H. Nakayama, M. Sanada, and Y. Takeda, "Sensorless Output Maximization Control for Variable- Speed Wind Generation System Using IPMSG", *IEEE Transaction on Industrial Application,* vol. 41, no. 1, pp. 60-67, January. 2005.

[128] W. Qiao; L. Qu; and R. G. Harley; " Control of IMP Synchronous generator for Maximum Wind Power Generation" *IEEE Transaction on Industrial Application,* vol. 45, no. 3, pp. 1095-1105, May/June 2009.

[129] M. E. Haque, K. M. Muttaqi and M. Negnevitsky, "A Novel Control Strategy for a Variable Speed Wind Turbine with a Permanent Magnet Synchronous Generator" *IEEE Transaction on Industry Applications,* vol. 46, no. 1, pp. 331-339, Jan./Feb., 2010.

[130] M. Chinchilla, S. Arnaltes, and J. C. Burgos, "Control of PermanentMagnet Generators Applied to Variable- Speed Wind-Energy Systems Connected to the Grid" *IEEE Transaction on Energy Conversion,* vol. 21, No. 1, pp. 130-135, March 2006.

[131] T. F. Chan, and L. L. Lai, "Permanenet-magnet machines for distributed generation: a review," *IEEE Power Engineering Society General Meeting, Tampa, Florida, June 24- 28, 2007,* pp. 1-6.

[132] M. De Broe, S. Drouilhet, and V. Gevorgian, "A peak power tracker for small wind turbines in battery charging applications," *IEEE Transaction on Energy Conversion*, vol. 14, no. 4, pp. 1630–1635, December 1999.

[133] M. G. Simoes and B. K. Bose, "Design and performance evaluation of a fuzzy-logic-based variable-speed wind generation system," *IEEE Transaction on Industry Applications,* vol. 33, no. 4, pp. 956–965, Jul./Aug. 1997.

[134] K. Tan and S. Islam, "Optimal control strategies in energy conversion off PMSG wind turbine system without mechanical sensors," *IEEE Transaction on Energy Conversion,* vol. 19, no. 2, pp. 392–399, June, 2004.

[135] S. M. Muyeen, R. Takahashi, and J. Tamura, "Operation and Control of HVDC-Connected Offshore Wind Farm ", *IEEE Transaction on Sustainable Energy Conversion,* vol. 1, no. 1, pp. 30–37, April 2010.

[136] A. M. O. Haruni, A. Gargoom, M. E. Haque, and M. Negnevitsky, "Dynamic Operation and Control of a Hybrid Wind-Diesel Stand Alone Power Systems" *Twenty-Fifth Annual IEEE Applied Power Electronics Conference and Exposition(APEC)*, Palm Springs, California, *21-25 Feb. 2010,* pp. 162-169.

[137] N. Gyawali, and Y Ohsawa, "Integrating Fuel Cell/Electrolyzer/Ultracapacitor System Into a Stand-Alone Microhydro Plant", *IEEE Transaction on Energy Conversion*, vol. 25, no. 4, pp. 1092-1104, December 2010.

[138] C. Wang, and M. H. Nehrir, "Power Management of a Stand-Alone Wind/Photovoltaic/Fuel Cell Energy System", *IEEE Transaction on Energy Conversion,* vol. 23, no. 3, pp. 957-967, September 2008.

[139] Sim Power Systems, Reference, Hydro-Québec, MathWorks, Inc., Natick, MA, 2011.

[140] O. Tremblay, L. Dessaint, "Experimental Validation of a Battery Dynamic Model for EV Application" *World Electric Vehicle Journal,* Vol. 3, pp. 1-10, 2009.

[141] M. Chen, and G. A. Rincon-Mora, "Accurate Electrical Battery Model Capable of Predicting Runtime and I–V Performance", *IEEE Transaction on Energy Conversion*, vol. 21, no. 2, pp. 504-511, December 2006.

[142] A. Khaligh, A. M. Rahimi, Y. J. Lee, J. Cao, A. Emadi, S. D. Andrews, C. Robinson, and C. Finnerty, "Digital control of an isolated active hybrid fuel cell/Li-ion battery power supply," *IEEE Transaction on Vehicular Technology,* vol. 56, pp. 3709 - 3721, Nov. 2007.

[143] Z. Jiang, L. Gao, and R. A. Dougal, "Flexible multiobjective control of power converter in active hybrid fuel cell/battery power sources," *IEEE Transaction on Power Electronics*, vol. 20, no. 1, pp. 244–253, Jan. 2005

[144] A. Hajizadeh, M. A. Golkar, and A. Feliachi, "Voltage Control and active Power Management of Hybrid Fuel-Cell/Energy-Storage Power Conversion System Under Unbalanced Voltage Sag Conditions", *IEEE Transaction on Energy Conversion,* vol 25, No. 4, pp. 1195-1208, December 2010.

[145] K. Jin, M. Yang, and X. Ruan, "Three-Level Bi-Directional Converter — A Novel DC-DC Converter Suitable for Fuel Cell Power System" *IEEE Power Electronics Specialists Conference 2006 (PESC '06), 18-22 June 2006*, pp. 1-6.

[146] O. Garcia, L. A. Flores, J. A. Olivier, J. A. Cobos and J. de la Pena, "Bi-directional DC/DC Converter for Hybrid Vehicles" *IEEE Power Electronics Specialists Conference 2005 (PESC '05)*, pp. 1881-1886.

[147] C.-H. Lin, H-W Liu, and C Jin, M. Yang, and X. Ruan, "Design and implementation of a bi-directional power converter for electric bike with charging feature" *IEEE Conference on Industrial Electronics and Applications (ICIEA), 15-17 June 2010,* pp. 538- 543.

[148] S Liu, X. Zhang, H. Guo and J. Xie , "Multiport DC/DC Converter for Stand-alone Photovoltaic Lighting System with Battery Storage" *International Conference on Electrical and Control Engineering (ICECE), 25-27 June 2010,* pp. 3894 - 3897.

[149] T Begalke "A direct isolated bi-directional converter as a power electronic building block (PEBB)" *IEEE Power Electronics Specialists Conference 2008 (PESC '08), 15-19 June 2008,* pp. 3894-3900.

[150] A. A. Fardoun, E. H. Ismail, A. J. Sabzali and M. A. Al-Saffar "Bi-directional converter with low input/output current ripple for renewable energy applications" *2011 IEEE Energy Conversion Congress and Exposition (ECCE), 17-22 Sept. 2011,* pp. 3322 - 3329.

[151] Z. Liao and X. Ruan "Control strategy of bi-directional DC/DC converter for a novel stand-alone photovoltaic power system" *IEEE Vehicle Power and Propulsion Conference, 2008. (VPPC '08), 3-5 Sept. 2008,* pp. 1 - 6.

[152] S. Pasricha, and S. R. Shaw, "A Dynamic PEM Fuel Cell Model" *IEEE Transaction on Energy Conversion,* vol. 21, no. 2, pp. 484-460, June 2006.

[153] C. Wang, M. H. Nehrir, and S. R. Shaw "Dynamic Models and Model Validation for PEM Fuel Cells Using Electrical Circuits" *IEEE Transaction on Energy Conversion,* vol. 20, no. 2, pp. 442-451, June 2005.

[154] M. Youssef, K. E. AL-NAdi and M. H. Khalil "Lumped Model for Proton Exchange Membrane Fuel Cell (PEMFC)" *International Journal Electrochemical Science*, vol. 5 pp. 267 – 277, 2010.

[155] Y. Shan, S.-Y. Choe "Modeling and simulation of a PEM fuel cell stack considering temperature effects" *Journal of Power Sources*, vol. 158 pp. 274–286, 2006.

[156] C.-Y. Wang, "Fundamental Models for Fuel Cell Engineering" *Chem. Rev.* vol. 104, pp. 4727–4766, 2004.

[157] J. T. Pukrushpan, A. G. Stefanopoulou and H. Peng "Modeling and Control for PEM Fuel Cell Stack System", *Proceedings of the American Conference, Anchorage, May 8-12, 2002,* pp. 3117–3122.

[158] H. Ju and C.-Y. Wang "Experimental Validation of a PEM Fuel Cell Model by Current Distribution Data", *Journal of The Electrochemical Society,* vol. 151 no.11, pp. 1954-1960, 2004.

[159] S. Caux, W. Hankache, M. Fadel and D. Hisselc, "PEMfuelcellmodel suitable for energy optimization purposes", *Journal of Energy Conversion and Management*, vol. 51, no. 2, pp. 320-328, Feb. 2010.

[160] Y. Hou, Z. Yang, G. Wan "An improved dynamic voltage model of PEM fuel cell stack", *International Journal of Hydrogen Energy,* vol. 35, pp. 11154- 11160, 2010.

[161] C. Kunusch, P. F. Puleston, M. A. Mayosky, J. J. More "Characterization and experimental results in PEM fuel cell electrical behaviour", *International Journal of Hydrogen Energy*, vol. 35, pp. 5876- 5884, 2010.

[162] P. Artuso, R. Gammon, F. Orecchini, S. J. Watson "Alkaline electrolysers: Model and real data analysis" *International journal of hydrogen energy*, vol. 36, pp. 7956 – 7962, 2011.

[163] T. Zhou, B. Francois, M. el H. Lebbal, and S. Lecoeuche, "Real-Time Emulation of a Hydrogen-Production Process for Assessment of an Active Wind-Energy Conversion System" *IEEE Transaction on Industrial Electronics,* vol. 56, no. 3, pp. 737-746, April 2009.

[164] O. Ulleberg "Modeling of advanced alkaline electrolyzers: a system simulation approach", *International Journal of Hydrogen Energy*, vol. 28, no. 1, pp. 21 – 33, 2003.

[165] N. Mendis, S. Sayeef, K. M. Muttaqi and S. Perera, "Hydrogen energy storage for a permanent magnet wind turbine generator based autonomous hybrid power system" , *IEEE Power Engineering Society General Meeting*, Detroit, Michigan, *23-28 July 2011,* pp. 1-7.

[166] S. Roy, O. P. Malik, and G. S. Hope, "An adaptive control scheme for speed control of diesel driven power plants", *IEEE Transaction on Energy Conversion,* vol. 6, No. 4, December, 1995

[167] G. S. Stavrakakis, G.N. Kariniotakis, "A general simulation algorithm for the accurate assessment of isolated diesel-wind turbines systems interaction. I. A general multi machine power system model" *IEEE Transaction on Energy Conversion,* vol. 10, no. 3, Sep 1995 pp:577 – 583.

[168] G. S. Stavrakakis, G.N. Kariniotakis, "A general simulation algorithm for the accurate assessment of isolated diesel-wind turbines systems interaction. Part II: Implementation of the algorithm and case-studies with induction generators" *IEEE Transaction on Energy Conversion*, vol. 10, no. 3, Sep 1995, pp: 584 – 590.

[169] P. Kundur, "Power System Stability and Control", ISBN 0-07-035958-X, New York, McGraw-Hill, 1994, Chapter 7.

[170] IEEE Std 421.5™-2005, "IEEE Recommended Practice for Excitation System Models for Power System Stability Studies", *IEEE Power Engineering Society,* 21 April 2006.

[171] A. M. M. Gargoom, A. M. O. Haruni, M. E. Haque, and M. Negnevitsky, 'Hybrid stand-alone power systems with hydrogen energy storage for isolated communities', *Transmission and Distribution Conference and Exposition, 2010 IEEE PES, April 19-22 2010, New Orleans, Louisiana, USA.*

[172] A. M. M. Gargoom, A. M. O. Haruni, M. E. Haque, and M. Negnevitsky, 'Voltage and frequency stabilization using PI-like fuzzy controller for the load side converters of the stand alone wind energy systems', *IEEE Power Electronic Society, Palm Springs, California USA, February 21-25 2010,* pp. 2132-2137.

[173] A. M. M. Gargoom, A. M. O. Haruni, M. E. Haque, and M. Negnevitsky, 'Dynamic Operation and Control of a Hybrid Wind-Diesel Stand Alone Power Systems', *IEEE Applied Power Electronics Conference and Exposition (APEC), Palm Springs, USA, February 21-25 2010,* pp. 162-169.

[174] A. M. M. Gargoom, A. M. O. Haruni, M. E. Haque, and M. Negnevitsky, 'Voltage and Frequency Stabilisation of Wind-Diesel Hybrid Remote Area Power Systems ', *Proceedings of Australasian Universities Power Engineering Conference (AUPEC 2009), , Adelaide, September, 27-30, 2009,* pp 1-6.

[175] A. M. O. Haruni and M. Negnevitsky, 'An Artificial Intelligence Approach to Develop a Time-Series Prediction Model of The Arc Furnace Resistance', *Journal of Advanced Computational Intelligence,* vol. 14, no. 6, pp. 722-728, September 2010.

[176] A. R. Sadeghian and J. D. Lavers, "Application of radial basis function networks to model electric arc furnaces," *International Joint Conference on Neural Network (IJCNN '99), Vol.6, July 10-16, 1999,* pp. 3996-4001.

[177] X.-H. Liu, R. Kuai, P. Guan, X.-M. Ye, and Z.-L. Wu, "Fuzzy-PID control for arc furnace electrode regulator system based on Genetic Algorithm," *International Conference on Machine Learning and Cybernetics, Vol.2, July 12-15, 2009,* pp. 683-689.

[178] G. Ping, L. Ji-chao, and L. Xiao-he, "Direct adaptive fuzzy sliding mode control of arc furnace electrode regulator system," *Chinese Control and Decision Conference, June, 17-19 2009, pp. 2776-2781.*

[179] Z. Hui and X. Wang, "Prediction Model of Arc Furnace Based on Improved BP Neural Network," *International Conference on Environmental Science and information Application Technology, (ESIAT 2009), Vol.3, July 4-5, 2009,* pp. 664-669.

[180] M. Negnevitsky, "Artificial Intelligence: a guide to intelligent systems," 2nd Edition, Addison-Wesley, Harlow, England, 2005.

[181] J.-S. R. Jang, C.-T. Sun, and E. Mizutani, "Neuro-Fuzzy and Soft Computing," A Computational Approach to Learning and Machine Intelligent, Prentice Hall, Englewood Cliffs, NJ, 1993

[182] A. M. M. Gargoom, A. M. O. Haruni, M. E. Haque, and M. Negnevitsky, 'Smooth synchronisation and power sharing schemes for high penetration wind diesel hybrid remote area power systems', *Australian Journal of Electrical & Electronics Engineering,* vol. 8 no.1 pp. 75-84, 2011.

[183] A. Kusiak, and Z. Zhang, "Short-Horizon Prediction of Wind Power: A Data-Driven Approach", *IEEE Transaction on Energy Conversion,* vol. 25, no. 4, pp. 1112-1122, December 2010.

[184] C. W. Potter, and M. Negnevitsky, "Very Short-Term Wind Forecasting for Tasmanian Power Generation" *IEEE Transaction on Power Systems*, vol. 21, No. 2, pp. 965-972, May 2006.

[185] N. Amjady, F Keynia, and H. Zareipour, "Short-Term Load Forecast of Microgrids by a New Bilevel Prediction Strategy", *IEEE Transaction on smart grid*, vol. 1, No. 3, pp. 286-294, December 2010.

[186] A. M. O. Haruni, and M. Negnevitsky, "An Artificial Intelligence Approach to Develop a Time-Series Prediction Model of the Arc Furnace Resistance" *Journal of Advance*

Computational Intelligence and Intelligent Informatics, vol 14, No. 6, pp. 722-729, September. 2010.